

**ROBUST MEMORY AND PRECISE BALANCE:
COMPUTATION WITH BIOLOGICAL NETWORK MOTIFS**

A Thesis
Submitted to the
Tata Institute for Fundamental Research, Mumbai
for the degree of Doctor of Philosophy
in Biology

by

SAHIL MOZA



National Centre for Biological Sciences
Tata Institute of Fundamental Research

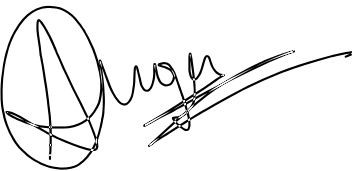
National Centre for Biological Sciences
Tata Institute of Fundamental Research
Bengaluru, India

July 2020

DECLARATION

This thesis is a presentation of my original research work. Wherever contributions of others are involved, every effort is made to indicate this clearly, with due reference to the literature, and acknowledgement of collaborative research and discussions.

The work was done under the guidance of Professor Upinder S. Bhalla, at the National Centre for Biological Sciences, Bengaluru, Tata Institute of Fundamental Research.



Sahil Moza

In my capacity as supervisor of the candidate's thesis, I certify that the above statements are true to the best of my knowledge.



Prof. Upinder S. Bhalla

Date: 15th July 2020

CERTIFICATE

I certify that this thesis entitled "**Robust memory and precise balance: Computation with biological network motifs**" comprises research work carried out by **Sahil Moza** at National Centre for Biological Sciences under the supervision of **Prof. Upinder S. Bhalla** during the period August 2012 - January 2020 for the degree of Doctor of Philosophy of the Tata Institute of Fundamental Research (TIFR). The results presented in this thesis have not been submitted previously to this or any other University for a PhD or any other degree.



Head Academics
National Centre for Biological Sciences
Tata Institute of Fundamental Research
Bangalore

अथ हैनं सौर्यायणि गार्यः पप्रच्छ । भगवन्नेतस्मिन्परुषे कानि स्वपन्ति कान्यस्मिआग्रति कतर
एष देवः स्वजान्यश्यति कस्यैतत्सुखं भवति कस्मिन्नु सैर्वं संप्रतिष्ठिता भवन्तीति ॥ १ ॥

Then Gargya approached the sage and asked him:
“Sir, when a man is sleeping, who is it that sleeps in him?
Who sees the dreams he sees?
When he wakes up, who in him is awake?
When he enjoys, who is enjoying?
In whom do all these faculties rest?”

- Question 4, Prashna Upanishad¹

¹The Upanishads, Introduced and translated by Eknath Easwaran

Accept and build

- To the joy, philosophy & art of improvisational theater.

ACKNOWLEDGEMENTS

The joy of discovery is a unique and surprisingly fulfilling state of mind that perhaps only very fortunate individuals have an opportunity to experience. For me, this experience has been possible due to many extraordinary people in my life, who I want to express my gratitude towards.

I begin by thanking my family for their patience and silent support during this time, and for several lessons that I have learned and continue to learn from them. My mother for her abstract thinking and the sense of awe, my father for his pragmatism and reasoning, my late grandfather for his cool and free mind, my grandmother for her grit and my brother for his constant love and unwavering support.

During my PhD, in addition to the craft of science, I have also learned several ways of exploring and expressing myself. I want to thank Upi for catalyzing many of these transformations. Upi has been a source of many opportunities, learning experiences, and patience with the several non-linear paths I sometimes took during my PhD. Much of this work has been possible due to the freedom of thought and expression that I enjoyed during my tenure at NCBS. Upi set up appropriate feedback loops to pull me back whenever my trajectory was wandering off to infinity, and gentle nudges when I was caught in limit cycles. There is much to learn from Upi in terms of his ethics and way of managing the lab. I have never had to wait an extra day whenever I've asked him for a recommendation or time for discussion. I know that I have gained more from here than I will realize immediately. In addition, I want to thank him for the basic neuroscience course, especially the segment on neurophilosophy, which has undoubtedly been the seed for my journey into both neuroscience and philosophy. Both of these have become important parts of my personality and dominate my intellectual thought.

I also have to thank Upi for the opportunity to organize the CAMP course. I have gained in many ways over the years while designing various parts of curriculum and teaching at the Com-

putational Approaches to Memory and Plasticity (CAMP) summer school at NCBS. I made many close friends and learned a lot from the diversity of people that I got the opportunity to interact with. Here I would also like to thank Subha, Aditya Gilra, and Bhanu for various discussions on CAMP organization, designing curriculum and tutorials.

My TCM members Rishi and Sandeep, for discussions, advice and always being prompt in setting up meetings. Arvind Kumar, who I have had many helpful and fascinating discussions with and has recommended me several times for various opportunities.

Thanks to Mukund, for some of the best lectures that I have had the privilege of attending: in Dynamical Systems, Information Theory and Stochastic Processes. He has a gift of reducing and simplifying concepts to the bare-bones, which were accessible and inspiring for student like me, new to many of these ideas. All these courses ended up being relevant for the work that I did during my PhD.

Sanjay for many interesting and enriching lunch table discussions, on a wide variety of topics, from old bollywood movies to interesting books.

I was also very lucky to have amazing company to live and hang out with throughout my PhD. I had an amazing time with my various house-mates and close friends Aanchal, Amit, Ananth, Anjali, Aparna, Calvin, Chaitra, Dinesh, Gulrez, Lena, Parul, Sriram, Vaibhav and Vishaka.

Upi Lab has always been a fertile ground for both learning and having fun. Thanks to Mehrab, Aditya Gilra, Subhasis, Neeraj from whom I learned a lot from as an early grad student. Thanks to all the members of Upi lab who I overlapped with. Special thanks to Harsha for always being helpful. Special thanks also to Aditya Asopa and Aanchal Bhatia for many discussions on eastern philosophical ideas which have become a close part of my life.

Of course, none of this would be possible without the plethora of support NCBS provides to graduate students. So thank you NCBS! Thank you for the comfortable accommodation (House-

keeping, security, elechelp), keeping me well fed (canteen, shout out to Roy), gainfully employed (accounts and admin), well prepared to give presentations and performances (instrumentation). Thanks to Chakrapani, Rifat, and many others at the IT section who were prompt to help me with installations and repairs on the cluster for my simulations. Thank you Vishalakshi and the admin office, for always being ready to help and making our lives easier by taking the bulk of the admin load.

A part of the work in this thesis has been possible due to animal model based research. I would like to extend my gratitude to the research animals (C57BL/6) for their sacrifice, and NCBS animal house, who strive to maintain policies for treatment of research animals in a humane, respectful, and ethical way.

Thank you to all the various other departments that have continuously and silently worked as regulatory elements in the background to keep the PhD life stable.

My life at NCBS was joyful and fun also due to an active culture of music, theatre and improv at NCBS

First, I want to begin by thanking Ananth, Aparna, Divya, Terence, and Vinca. No words fit the description for the beautiful bond that I shared with this group practicing and performing improvisational theatre. I wish everyone an experience of this nature, where a group can develop trust for each other with an intensity that I experienced with them. It is very satisfying to see a seed that you sow, grow up to become independent and larger than yourself. I would like to thank all past and present members of StageFright (Prabahan, Gaurav, Vardhanam, Shweta, Manal, Vrinda, Shyam, and many others) who I have had the pleasure to practice, teach and perform improv theatre with on campus. A special thanks to Ananth, Terence and others who inspired me to pick up music more regularly. I have learned to open up in expressing myself through music in large parts due to many improvised jam sessions. Thanks to Prabahan and all cast and crew members of StageCraft at NCBS and Rangmarch at IISc for the opportunity to perform and develop my craft in theatre.

Thanks to Dr. Aanchal Bhatia for being a wonderful collaborator, a friend and an all-weather companion :).

My thesis reviewers Prof. Avrama Kim Blackwell (George Mason University, Virginia) and Dr. Collins Assisi (IISER, Pune) for their suggestions and encouraging words about my PhD work.

CSIR, DBT, NCBS and TIFR for funding me during various periods during my PhD.

To end, I would like to express gratitude to people from all professions who are continuously fighting against the COVID pandemic, putting their own lives at risk, trying to make our lives safer.

LIST OF PUBLICATIONS

Research articles

1. Bhatia, A.*, **Moza, S.***, Bhalla, U.S., "Precise excitation-inhibition balance controls gain and timing in hippocampus.", *eLife, April 2019* (*Equal contribution)
2. **Moza S.**, Bhalla, U.S., "Different dimensions of robustness- noise, topology and rates - are nearly independent in chemical switches.", *bioRxiv Aug 2020*
3. HarshaRani, G.V., **Moza, S.**, Ramakrishnan, N., Bhalla, U.S., "SWITCHES: Searchable Web Interface for Topologies of CHEmical Switches.", *bioRxiv Aug 2020*

Book chapter

Bhatia, A., **Moza, S.**, Bhalla, U.S., "Patterned Optogenetic Stimulation using a DMD-projector", *Channelrhodopsin, Chapter 11, Springer Protocols, 2020 (In press)*

Table of Contents

Chapter 1: Introduction	1
1.1 Dynamical systems	10
1.2 Robustness and emergence of network motifs	15
1.3 Excitation and Inhibition in the brain	17
1.4 Neural Coding	19
1.5 Excitation Inhibition Balance	22
1.6 Hippocampus	26
1.7 Precise EI balance and Subthreshold Divisive Normalization	28
Chapter 2: Robustness properties of chemical switches	43
2.1 Introduction	45
2.2 Results	49
2.3 Discussion	62
2.4 Methods	66
2.5 Supplementary Figures	80

Chapter 3: Precise excitation-inhibition balance controls gain and timing in the hippocampus	83
3.1 Main article	84
3.2 Supplementary figures	114
3.3 Supplementary tables	138
Chapter 4: Conclusion	142
4.1 Families of feedback loop networks inherit robustness attributes from their root networks	145
4.2 Feedforward inh circuit with precise EI balance leads to gain control	148

Chapter 1

Introduction

Living systems continuously extract and compute relevant information about their external environment. This computation involves propagation, manipulation, and maintenance of this information across large intricate networks. Decades of research in complex systems theory, including network theory, dynamical systems theory and developments in computational modeling have guided research in the *systems* sciences, which aims to understand these computations. Owing to the mathematical backbone of this field, and inherent symmetry in nature, similar general rules have been found to predict properties of social networks, neuronal networks, and protein-protein interaction networks (Barabasi and Albert, 1999; Milo et al., 2002). These examples suggest that similar computations may be organized on different substrates, across different lengthscales and timescales, due to conserved relations between them. In this thesis, I uncover fundamental aspects of dynamics in commonly occurring motifs across two different systems: chemical reaction networks, and neuronal networks using tools from complex systems theory.

The keystone of systems sciences or the constructionist idea has been very well summarised in an essay by P.W. Anderson (Anderson, 1972):

The ability to reduce everything to simple fundamental laws does not imply
the ability to start from those laws and reconstruct the universe.

He discusses the usefulness, but the inherent incompleteness of the reductionist idea of science, which posits that understanding can be achieved by reducing a system to its parts, and studying these parts in isolation. However, this approach suffers from the inability to explain observed emergent properties of *complex* natural systems. This is because entirely new dynamical properties emerge when these reduced units are put together with their interactions.

This thesis is structured by two key ideas. First, complex networks are composed of small structural repeating elements called *motifs*, which are thought to have been learned over evolution to transform information across networks. Formally defined as a set of (two or more) conserved relations between (two or more) entities, motifs are patterns that occur above chance levels in a network. Just like words for a language, or logic gates for a computer, motifs can form the structural vocabulary for a complicated network, containing reusable or repeatable computational units. Second, network structure constrains the dynamical system that sits in it. This suggests that by knowing the structure of motifs, one can suggest properties and potential computations of its dynamics (Shoval and Alon, 2010).

Below, I summarise findings from two different kinds of computations: gain control and memory from the perspective of two different kinds of network motifs: the feedforward inhibitory loop motif and the positive feedback loop motif respectively.

Networks and network motifs

A *network* is a pattern of relations between entities. They are often written in the form of mathematical objects called *graphs* with vertices as *nodes*, and connecting lines called *edges*. These relations (edges) can be *directed*, i.e. pointing from one node to another, or *undirected*. The number of edges that a node makes with other nodes in the network is called its *degree*. Networks and network (graph) theory have been used extensively to understand complex interactions between a large number of entities, such as the internet, gene regulatory networks, protein-protein inter-

action networks, neural networks, opinion networks, epidemic propagation (Barabasi and Albert, 1999). Organizing observations about the world in this form has revealed the underlying structure in connections in several real-world networks. Three striking properties are found in real networks. First, many real networks are *scale-free* (Barabasi and Albert, 1999), i.e. the distribution of degrees of the graph follows a power-law: $P(k) \approx k^{-\gamma}$, where k is the degree and γ is the exponent, ($2 < \gamma < 3$ for many real-world networks). This implies that there are very few nodes with a large number of connections and many nodes with a few connections. Second, many real-world networks are also *small-world*, i.e. it is possible to visit any node in the graph from any other node in very few steps. Specifically, for a graph with n nodes, $\leq \log(n)$ nodes need to be traversed to travel between two random nodes (Watts and Strogatz, 2011). Third, real networks have patterns of interconnections that exist at a frequency higher than that expected by chance (Milo et al., 2002). These are called network *motifs*.

Network motifs can be thought of as reusable sub-units that can perform a set of computations (Alon, 2007). Figure 1.1 shows all possible graphs of size 2 and 3 nodes. Some of these graphs are also motifs: feedforward loops and cycles are found in larger proportions than chance in real networks. Motifs have been shown to exist across different types of networks, and are widely thought of as an organizing property of real networks (Alon, 2007; Sporns and Kötter, 2004). Motifs lie at a unique vantage point for both reductionist and systems-level analysis. From a reductionist viewpoint, the mathematical transformations performed by small network motifs can be studied in isolation through simulations. For example, two or three node auto-regulatory and feed-forward loops have been simulated and experimentally analyzed in isolation to study their computational properties (Becskei and Serrano, 2000; Becskei et al., 2001). From a systems perspective, there are at least two directions where studying motifs can be useful. First, network computations can be seen as emerging from the relations between various motifs. Second, motifs can be empirically studied and used to design manipulations in the context of computations performed by the biological network (Braganza and Beck, 2018).

Arguably, the most important property of motifs is that they are generalizable. Computational properties of a motif from one network may give rise to predictions for potential computations in another. These properties suggest that motifs are good candidates for investigation, as they can encompass the computational theory, the algorithm as well as the hardware implementation: all three levels of description suggested by David Marr (Marr and Poggio, 1976). As an example, the feedforward inhibitory circuitry in the hippocampal CA3-CA1 network (see Fig. 1.6 below) resembles the Incoherent Type 1 Feedforward Loop (I1-FFL) (Alon, 2007) found to be enriched in yeast and bacterial gene regulatory networks (Mangan and Alon, 2003; Mangan et al., 2006). Interestingly, I1-FFLs have been suggested (Goentoro et al., 2009) to be responsible for normalization in gene regulatory networks, analogous to our finding of Subthreshold Divisive Normalization in the CA3-CA1 network (Bhatia, Moza, and Bhalla, 2019), discussed in Chapter 3 of this thesis. Several contemporary systems biology and systems neuroscience studies are based on circuit-logic of this nature (Koyama et al., 2016). Several known circuit motifs and their computational functions have been reviewed by (Braganza and Beck, 2018) for the brain, and by (Shoval and Alon, 2010) for transcriptional and signaling networks.

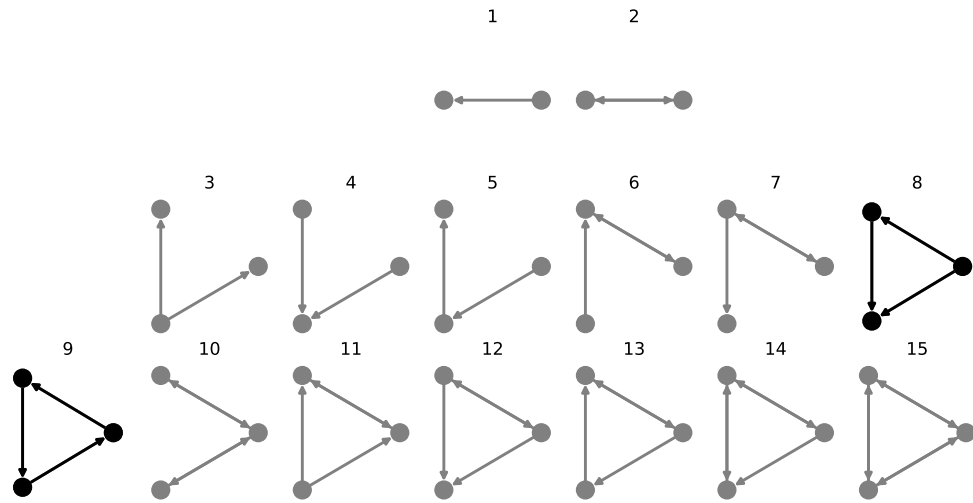


Figure 1.1: All possible 2-node and 3-node directed graphs. Pattern 8 is the feed-forward loop motif, and pattern 9 is a cycle.

In this body of work, I have attempted to study computations of two different network motifs at this level of detail: Feedback loop motifs and Feedforward loop motifs (Fig. 1.2).

Feedback loops

Feedback loops (Fig. 1.2a) are recurrent, *instability* causing structures and are one of the simplest motifs that give rise to interesting emergent nonlinear phenomena like *bistability* (positive feedback loops) and oscillations (negative feedback loops). If both the interactions are negative (Fig. 1.2a), that still leads to a net positive feedback loop and can give rise to robustly bistable toggle-switches (Shoval and Alon, 2010). In Chapter 2, I have studied the robustness properties of different kinds of perturbations to bistable graphs, with at least one net positive feedback loop, and other connections between nodes that affect the robustness properties of the network.

Feedforward loops

Feedforward loops (Fig. 1.2b) are one of the most common network patterns found in several biological systems, such as *E.coli* and yeast gene regulatory networks, and the nervous system. Since there are 3 directed edges in this network, and each interaction could be positive (excitatory) or negative (inhibitory), there are $2^3 = 8$ possible feed-forward loops. Out of these, in Chapter 3, I have looked at the hippocampal CA3-CA1 network, which is an Incoherent-Type-1 FFL with positive interactions from $a \rightarrow c$ and $a \rightarrow b$, and one negative (inhibitory) interaction from $c \rightarrow b$. In the neuroscience literature, this motif is called disynaptic feedforward inhibitory network motif. These motifs are computationally known to be pulse-generators and fold-change detectors in gene regulatory networks (Shoval and Alon, 2010).

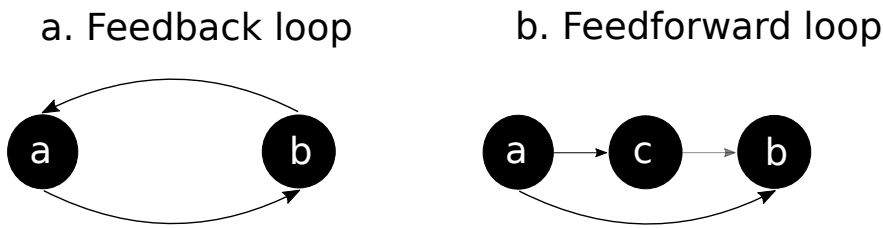


Figure 1.2: Important motifs for this thesis. **a.** Feedback loop motif. This is the backbone of multistability and many other emergent phenomenon in complex systems. The arrows could be either both positive or both negative interactions, giving rise to a net positive cycle, or a *positive* feedback loop. **b.** Feed-Forward Loop (FFL) motif. The gray arrow depicts a negative interaction from $c \rightarrow b$, making this Incoherent Type 1 FFL.

Chemical reaction networks

The representation of chemical reactions in binary relations between reactants (as described in Figure 1.1 and 1.2) is inherently lossy as it loses the bimolecular nature of most reactions, which are often the cause of interesting non-linearities. As an example, it is non-trivial to depict the simple reaction $A \leftrightarrow B + C$ in a network of the form shown in Fig. 1.1. Since our focus is on networks of this kind, we will use an alternative description of chemical reaction networks (Fig. 1.3), with the set of elementary reactions described in (Ramakrishnan and Bhalla, 2008). Here the nodes

(circles) are reacting entities, and each reaction confers a set of directed edges between them, as per the SBGN (Systems Biology Graphical Notation) formulation (Le et al., 2009). Bidirectional reactions are written as half arrows separated by a square. Enzymatic reactions have an additional circle impinging on the square from the entity that acts as an enzyme and the directionality of the reaction is marked with a full arrow. The reaction $A \leftrightarrow B + C$ is shown in Fig. 1.3 with signature $|Eabc|$, and the enzymatic reaction $A \xrightarrow{B} C$ with signature $|Jabc|$. Thus, the motifs described in the previous section would be composed of a combination of reactions of this kind.

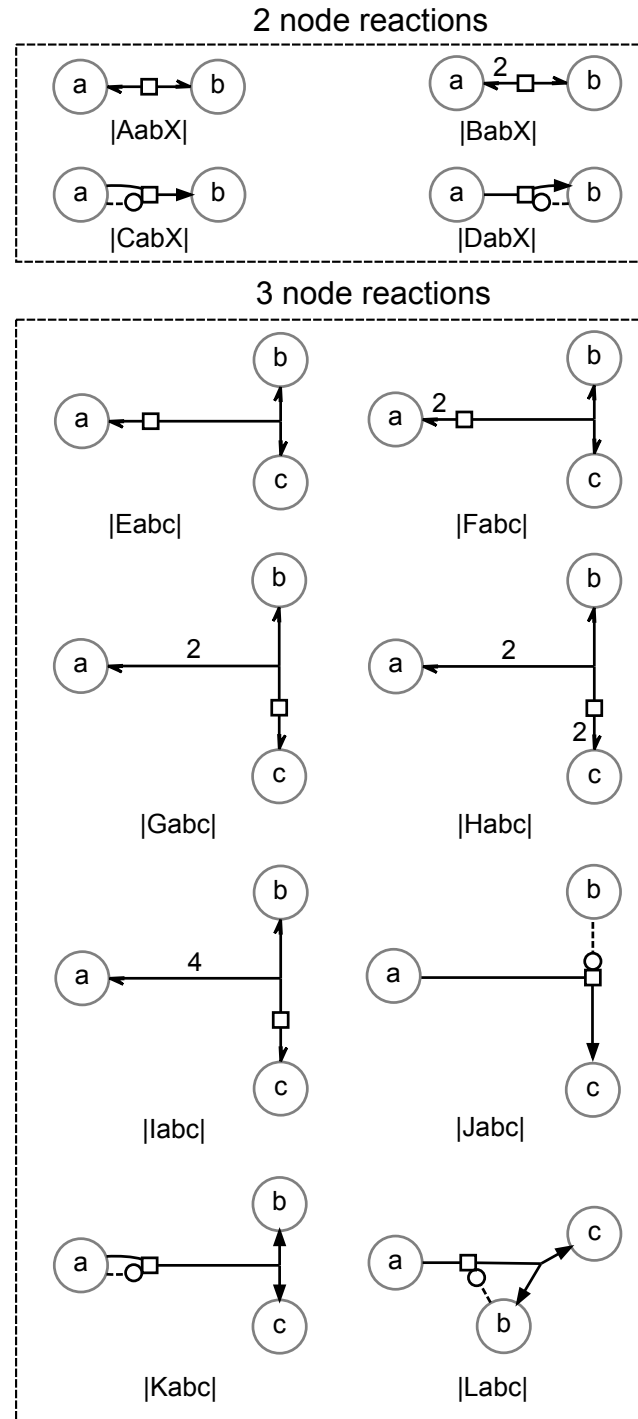


Figure 1.3: Individual chemical reactions (Ramakrishnan and Bhalla, 2008) as an SBGN network (Le et al., 2009). Box above and below are reactions with two and three reactants respectively, and each reaction has a signature displayed below. Big circles (nodes) depict reactants, and squares surrounded by arrows connecting nodes indicate reactions. Bidirectional reactions (e.g. signature $|AabX|$ with reaction $a \leftrightarrow b$) are depicted by half arrows. Enzymatic (directional) reactions are depicted by full arrows pointing towards the product, and the enzyme connects to the reaction with a dotted line attached to a small circle (signature $|Jabc|$ where b catalyzes a to c: $a \xrightarrow{b} c$).

Criticisms

There have been criticisms of this approach at different scales. These can be categorized into the following:

1. Over-representation of a set of patterns in comparison to a random network is not necessarily surprising: It has been suggested that the enrichment of feedforward loops in gene regulatory networks can be a byproduct of genome evolution (Cordero and Hogeweg, 2006), criticizing the comparison of the statistics of real networks with artificially generated networks using probabilistic growth (Erdos-Renyi type) or by preferential attachment of nodes to other nodes of a high degree (Albert and Barabási, 2002) algorithms.
2. Over-representation may be true, but this doesn't imply functional relevance to this structure (Ingram et al., 2006): To what extent does the structure of a network motif determine its function? This question is under active debate. While the observation of the existence of motifs stands, whether or not this is consequential in determining computational functions has proponents on either side of the argument.
3. Over-representation may be true, but possible function space is very high dimensional: There is very little consequence of network motif structure, and neither most motif structures have unique functions, nor can it be predicted from the function what structure of motifs to expect (Ingram et al., 2006; Payne and Wagner, 2015).

Even in the light of these criticisms, there is merit in looking at motifs in biological systems. This comes from the view that both the function and the *robustness* of networks to perturbations influence the sustenance of real networks over evolution. Thus, even with the presence of a kind of degeneracy of function in different motif structures, each motif may have different robustness to different kinds of perturbations, which may determine their eventual existence in real networks (Santolini and Barabási, 2018). This is discussed in more detail in Chapter 2. Thus, the dynamical systems that sit in these subnetworks may be “optimized”, in the presence of *robust*

motif structures.

Dynamical systems

A dynamical system is the set of rules according to which a physical system evolves in time. The evolving predator-prey population in an ecosystem, the sodium channel conductance in a neuron as it fires, the evolving concentration of CaMKII in a cell are all examples of dynamical systems. These are often formalized as a set of first-order time-dependent differential equations of the form:

$$\dot{X}(t) = F(X(t), \theta)$$

where $X = (x_1, x_2, x_3, \dots, x_n) \in \mathbb{R}^n$ are called *state variables* of the physical system, $F = (f_1, f_2, f_3, \dots, f_n) \in \mathbb{R}^n$ is the *vector field* according to which the state variables evolve in time, and $\theta \in \mathbb{R}^n$ is the vector of *parameters* that shapes the vector field F . For a fixed F and θ , the path taken by $x \in X$ in time is called a *trajectory*. Taking the CaMKII example, the concentrations of Ca^{2+} and $CaMKII$ are state variables, the nature of the chemical reactions between them will define the the vector field, or the differential equations for the change in their concentration, and the rates of reactions are the parameters for this dynamical system.

Paths in the vector field for which $f_i \in F = 0$ are called *nullclines*. The values of state variables for which the entire vector field $F = 0$ are called *fixed points*. If the vector field is pointing towards the fixed point, i.e., it is absorbing all nearby trajectories, the fixed point is called *stable* or an *attractor* or a *sink*, and the fixed point is called *unstable* or *source* if it is repelling surrounding trajectories, i.e. the vector field is pointing away from the fixed point. If the vector field has both attractive and repulsive components in different directions, it is called a *saddle node*.

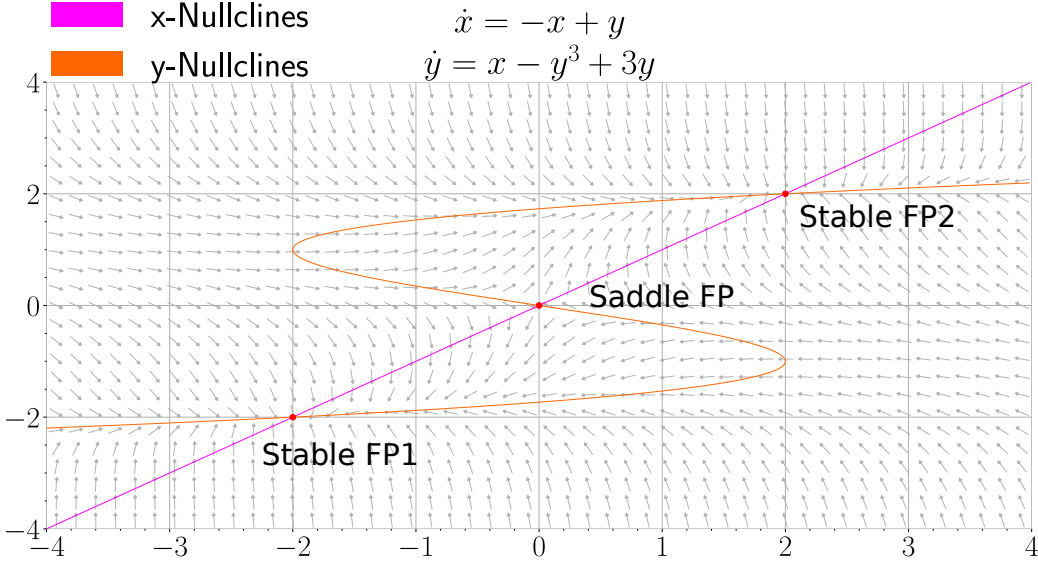


Figure 1.4: A dynamical system defined by the equations in the title. The phase plot here has arrows depicting the vector field F , and the pink and orange lines represent the x and y null-clines ($\dot{x} = 0, \dot{y} = 0$) respectively. The null-clines intersect thrice, giving this system 3 fixed points, two of which are stable and one is saddle.

Bistable systems

Bistable systems are dynamical systems with exactly two attractors. Fig. 1.4 depicts a bistable system with two stable fixed points and a saddle fixed point. Note that this requires three intersection points between the null-clines, and this process depends on the existence of net positive feedback in the network. This bistable behavior can be lost by changing the coefficients in these equations beyond certain special values called *bifurcation points*.

Bistable systems are ubiquitous and are known to be involved in decision-making processes in cells. Here decision making implies that an analog signal is converted into a digital (ON/OFF) signal: the *state space* can be divided into two regions for initial conditions or *basins of attraction*, each leading to a different equilibrium point. This can be seen in Fig. 1.4, where following the vector field always uniquely leads to one stable fixed point or the other. In a biological context, let's say that the concentration of a protein inside the cell sits at the first fixed point (Stable FP1) and

signals the *OFF* state at equilibrium. Now, at the arrival of an external stimulus, the concentration crosses a threshold (Saddle FP), defined by the structure of the connectivity of the chemical reaction network, and the rates of reactions. As the cell crosses over to the other basin of attraction, it will be pulled to the other fixed point (Stable FP2), which signals the *ON* state. The Cdk1 mitotic trigger (Trunnell et al., 2011), Sonic Hedgehog (Lai et al., 2004), MAP-K (Bhalla and Iyengar, 1999) are some examples of this kind of decision-making inside cells.

An early biological example of this analog to digital conversion is progesterone-induced maturation in *Xenopus* oocytes (Ferrell and Machleider, 1998). Increase in progesterone increases the proportion of mature oocytes. But for an individual oocyte, the graded progesterone concentration is converted into a cell-fate binary decision by the bistable MAP Kinase pathway, complementing other regulatory mechanisms.

In addition to decision making, the ability to switch states robustly can also be thought of as a mechanism for memory formation and storage. Indeed, flip-flops and light switches are both examples of devices that switch binary states to encode memory and then store memory in one stable state. There are multiple proposals of bistable synaptic chemistry responsible for memory formation, e.g. CamKII (Lisman, 1985; Zhabotinsky, 2000). Further, the size of dendritic spine sizes shows bimodality, potentially suggesting underlying bistable chemistry (Dorkenwald et al., 2019).

For many real systems, this deterministic picture of dynamics is deficient. This is because the real world is noisy. Behind the apparent reliability of biological processes, resides a constant fight against disorder posed by both the system and the environment. These are fluctuations from two sources: **Extrinsic**: structure and environment of real systems change dynamically, and **Intrinsic**: there is inherent stochasticity in real systems, which becomes apparent when the number of reacting entities (copy number) is low, and they can no longer be treated as continuous. These can lead to interesting phenomena like loss of bistability due to bifurcations, and spontaneous state

switching in bistable systems, which can be undesirable for both decision making and memory storage.

Stochastic dynamical systems

A stochastic dynamical system is a dynamical system that is subject to noise. Dynamical systems can be modeled using Langevin equations, which are of the form:

$$\dot{X}(t) = F(X(t), \theta) + \eta(t)$$

where $\eta(t)$ is the noise in the system which leads to fluctuations in the otherwise deterministically evolving states of the system. In this form, the statistical features of this noise can be approximated by linear noise approximation (Elf and Ehrenberg, 2003), and drawn at every time-step from a pre-defined distribution. However for small systems, this approximation is not required, and the time evolution of all occupied states by the system can be simulated using a *master equation*.

The master equation tracks the probabilities of occupancy of given states by the system over time. Let $P(x, t)$ be the probability that the system is in state x at time t . Then, the time evolution of state space can be written as (Kampen, 2007):

$$\frac{\partial P(x, t|x_0, t_0)}{\partial t} = \sum_{j=1}^n [a_j(x - v_j)P(x - v_j, t|x_0, t_0) - a_j(x)P(x, t|x_0, t_0)]$$

Here $a(x)$ is the *propensity* of the system to move towards state x from other states. This system can be simulated algorithmically with the Gillespie stochastic simulation algorithm (Gillespie, 1977).

Intrinsic noise is caused due to the thermal fluctuations or random spatiotemporal motion of particles. While the Gillespie algorithm helps us simulate the statistics of reactions between a few

particles effectively, it is assumed that space is uniformly filled with particles of a kind. As an example, Fig. 1.5 shows 5 instances of a radioactive decay process or reaction A from Fig. 1.3, simulated with the Gillespie algorithm using the MOOSE simulator (Dudani et al., 2015; Ray et al., 2008). If spatial effects are important, space can be compartmentalized into smaller *well-mixed* units, by using diffusion length-scales in combination with diffusion equation. Alternatively, a more computationally intensive, single-diffusing-particle tracking can be employed for simulations (Kerr et al., 2008; Andrews et al., 2010).

In many cases, this noise is ignored, if the system volume is large. If the change in concentration of molecules per reaction is much smaller in comparison to the total number of particles in the system, then the stochasticity caused in the smaller subsections of the full system can be ignored. However, if we think of individual cells, or smaller compartments like dendritic spines, when the number of particles is ~10s or ~100s of molecules of a given protein type, this noise become substantial enough that it cannot be neglected and it becomes useful to treat the system as an interacting set of discrete particles.

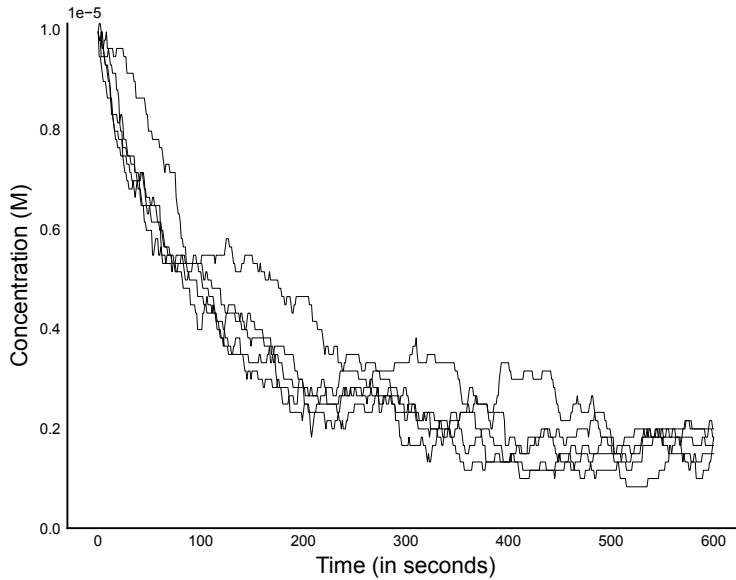


Figure 1.5: 5 instantiations of a radioactive decay system (Fig. 1.3 reaction A.) at 10 fL with concentrations of A plotted as a function of time.

Robustness and emergence of network motifs

(Prill et al., 2005) made an interesting observation by analyzing several biological networks: the abundance of motifs is directly correlated with the robustness of motifs to perturbations. They go on to suggest that robustness of network motifs to intrinsic noise and other perturbations, could be an organizing property of real networks. A direct consequence of this observation then, is: what determines the robustness of a network? Or conversely, are there any general principles of robustness that govern the existence of a certain set of motifs? In parallel, there is evidence that network motifs can emerge from interconnections that favor stability (Angulo et al., 2015). By quantifying the rate at which trajectories from closely separated points in the phase plane converge, something called *contraction loss*, (Angulo et al., 2015) showed that for real networks motifs seem to reduce contraction loss. What are the kinds of connections that can favor stability in forming these motifs?

Both these question can be addressed by investigating the various sources of perturbations that can be faced by the biological CRNs. These perturbations can be to the structure of the reaction network (due to loss-of-function mutations), parameters of the reaction network (SNPs that change protein binding affinities, the disorder in protein structures), stochasticity (small number of molecules per compartment), or state-vectors (In what ratio are the relative concentrations of signaling proteins sensible?). The synaptic proteome is shown to be a scale-free network (Chapter 2, (Hensch and Fagiolini, 2004)), which means that it is robust to random removal of nodes. However, this property may not give it much robustness to thermal noise. Are biological networks then tuned to be robust to many such perturbations? We can derive inspiration from protein structures, which have evolved to have conserved secondary structure motifs. Structural motifs, like the DNA binding zinc-finger motif (α -helix and antiparallel β -strands) and Calcium-binding domains (the loop-helix-loop motif) have evolved both functional and robustness properties.

Robustness	Persistence to	Pertains to	Example
Structural	Removal of reactions	Loss of bistability	Loss-of-function mutation
Parametric	Variation of reaction rates	Loss of bistability	Change in protein binding affinities
Stochastic	Thermal noise or # particles	Spontaneous transitions	Small compartments
State-vector	Signaling information	Multiple relative conc.	Non-sense signals

Table 1.1: Different persistence properties of a chemical reaction system and corresponding robustness.

As stated previously, bistable systems can arise from both double-negative feedback (toggle-switches) and double-positive feedback. Toggle switches are more robust to noise, given the presence of negative regulation, as negative feedback dampens noise-based transitions.

In Chapter 2, we use the SWITCHES database (<http://switches.ncbs.res.in>) which contains all possible chemical reaction networks at the level of up to 4 molecules with up to 6 reactions (Ramakrishnan and Bhalla, 2008). Then we pick up the bistable chemical reaction diagrams

from the SWITCHES database. By giving them random parameters and assessing stability, we find the basins of attraction of these bistable systems. We then proceed to perturb these systems with perturbations mentioned in Table 1.1 and show that there is a weak average correlation between the structures that lead to structural and parametric robustness of bistable systems. This would predict that by looking at real networks that are constrained by these different kinds of perturbations, we may see different kinds of network structure. However, by a suitable grouping of chemical reaction networks by their smallest bistable subnetworks (called *root groups*), we found a neat organizational principle. The existence of certain root groups indicated both a higher propensity of forming larger bistable networks and high resilience to changes in reaction-rate parameters. Interestingly, we observed that a mirror-symmetric network topology consisting of competitive autocatalytic loops showed both high structural and parametric robustness. We also analyze other forms of robustness mentioned in the table and suggest what kinds of network topologies lead to high robustness for these perturbations.

Akin to the dynamics of transcription factor and protein concentrations in transcriptional and protein-protein interaction networks, communication in the nervous system is based on the dynamics of membrane potential of neurons in a network. The flow of charge across the neuronal networks is mediated by synapses. A neural network can thus be constructed as neurons as nodes, with synapses as edges between these nodes. However, unlike protein-protein interaction networks, neural networks *can* be drawn much like Fig. 1.1 with neurons as nodes with directed, weighted positive and negative edges as they have direct excitatory and inhibitory synapses respectively.

Excitation and Inhibition in the brain

The nervous system has two antagonistic communication channels that race together from stimuli to responses: *excitation* and *inhibition*. Excitation acts as the driving force provided by chemical synapses, taking neurons towards depolarized potentials and spiking, inhibition works as the

brakes by bringing the neurons towards hyperpolarized potentials (away from spiking). Thus, the neural communication proceeds by the interplay between these two forces acting on neurons, one trying to win over the other. There are several examples in which this second parallel channel of inhibition can modulate excitation, and gate information flow across the nervous system. But what is the scope of computational benefits, if any, if the second channel is seemingly a delayed, scaled, inverted copy of the other?

Below I describe in the context of neural coding, the process and brief history of *precise excitation-inhibition balance*, a phenomenon in which random combinations of excitatory inputs received by a neuron are balanced by inhibition in their basal state.

The earliest description of the nervous system in terms of excitation and inhibition comes from the Autonomic Nervous System. Inhibition was first recognized as a distinct process in the mammalian heart under the control of vagus nerve. Eduard Weber and Ernst Heinrich Weber (of Weber's law) showed that irritation of the vagus nerve leads to decrease in the heart rate (Weber and Weber, 1845). Inspired by Weber's ideas, Charles-Édouard Brown-Séquard, another visionary, put forth in 1894, the *inhibition hypothesis* for the central nervous system, suggesting that, just like the vagus controls the heart, there is inhibition in the brain, acting alongside excitation, controlling motor movements (Aminoff, 2017; Engelhardt, 2014; Brown-Séquard, 1894). His intuition, based on his experiments with spinal cord lesions were even more profound. His experiments with monkeys showed that sensory loss produced by a lesion of the spinal cord on one side could be reversed, by an additional lesion made several segments below on the same side. This, in addition to the rescue of some sensory deficits by spinal lesions by stretching of the sciatic nerve, suggested to him that the observed effects must not be caused by the lesions alone, but due to a dynamic interplay between excitation and inhibition. He argued against the then mainstream *brain centers hypothesis*, which posited that there are different centers in the brain for specific higher-level functions. He proposed that the brain functions are composed by the integration of dynamic excitatory and inhibitory

tory activity, at multiple areas in the brain by activation of task-specific networks (Brown-Séquard, 1894; Aminoff, 2017; Engelhardt, 2014), which is both relevant and remarkably prophetic given our current understanding of brain function.

Around the same time, Sir Charles Sherrington, who was also a proponent of the inhibition hypothesis, was studying the antagonistic innervation of excitation and inhibition in the flexor-extensor muscles in various reflexes, including knee-jerk reflex. Sherrington showed the functional role of reciprocal inhibition in the alternating activity of these muscle pairs: when one is active, the other is inhibited (Sherrington, 1906). The vagus nerve preparation was utilized again by Otto Loewi (Loewi, 1921), who in combination with Sir Henry Dale took the fluid from one beating frog heart after vagus nerve stimulation, and applied it onto another beating frog heart. The decrease in the beating rate for the second heart established the existence of chemical neurotransmission, settling the long-standing debate between chemical and electrical neuronal communication. Thus, the first neurotransmitter was discovered: acetylcholine (ACh), as an inhibitory neurotransmitter. It is now known that ACh plays an important role in excitatory neurotransmission as well when it binds to *nicotinic* and some subtypes of *muscarinic* receptors. It took another three decades before the first intracellular inhibitory postsynaptic potentials (IPSPs) were recorded from Renshaw cells and Ia interneurons by Sir John Eccles, a former student of Sir Charles Sherrington, that mediated inhibition in motoneurons in the biceps-quadriceps antagonistic pair in a feedback and feedforward manner respectively (Brock et al., 1952).

Neural Coding

Soon after the discovery of the neurotransmitters, Adrian and Zotterman discovered that the sensory nerves innervating muscles emitted spikes in proportion to the increased weight hung from a muscle (Adrian and Zotterman, 1926). This established that the pattern of firing rates of neurons *encoded* information about the stimulus. In this sense, *encoding* generally implies that

it is possible to reliably reconstruct features of the stimulus using features extracted from neural activity measurements.

The broad role of inhibition in neural code was clear from very early measurements of circuit properties in the nervous system. However, Hubel and Wiesel shed light on the sophisticated nature of an inhibition-dependent neural code. In a series of papers, Hubel and Wiesel showed responses of neurons to selective orientations of bars of light by recording individual neurons, called complex cells in the cat visual cortex (Hubel and Wiesel, 1962). The activity of a given complex cell encoding different bar orientations could be drawn as a histogram, and this distribution of the neuron to the space of stimuli was called the *tuning curve* for that neuron. The computation leading to this observation was suggested to be *lateral inhibition* between complex cells (Blakemore and Tobin, 1972). Lateral inhibition is a circuit mechanism where neurons inhibit their neighbors in a graded manner. In this, the *nearest neighbors* are most strongly inhibited and the inhibition strength declines with distance on some metric, for example, physical space. It is important to say here that the field hasn't yet reached consensus about the computational mechanism leading to these observations.

Around the same time, Eccles postulated another inhibitory mechanism for oscillations in the thalamocortical recurrent inhibitory circuit (Anderson and Eccles, 1962). In this mechanism, called inhibitory phasing, the thalamocortical neurons excite the reticular nucleus neurons, which in turn inhibit back the thalamocortical neurons. This, in addition to the incoming depolarizing input on the thalamocortical neurons from the medial lemniscus, leads to the rhythmic activity of the thalamocortical neurons. This paved the way for several circuit based computations that have been found since then in various systems by an interplay of excitation and inhibition. For example, oscillations have also been observed to be produced by reciprocal inhibition: when tonically excited neurons inhibit each other: e.g. in locomotion in locusts (Lundberg, 1981), in aquatic vertebrates (Parker and Grillner, 2000), and mammals (Butt et al., 2002).

As the in-vivo recording technique got better, many intra-cellular recordings were made in awake behaving animals. Two interesting properties were observed that are relevant:

1. Neurons fire spontaneously in a manner that the variance of spike times is similar to the mean, and the inter-spike interval is close to exponentially distributed.
2. The rate of firing of neurons and their inter-spike intervals are correlated with behavioral variables, in a way that these can be used to reconstruct aspects of the stimulus.

Several studies demonstrated that the variability in the spike-times in cortical discharge in cat striate cortex and monkey visual cortex was Poisson-like. This implied that the variance in inter-spike-intervals of neurons divided by their mean spike-times was about 1.5 (Dean, 1981; Tolhurst et al., 1983). This soon was observed to be a general feature of cortical neuronal discharge. This noise was initially modeled as an intrinsically random process, as a function of the membrane potential fluctuations.

In 1964, Gerstain and Benoit Mandelbrot¹ suggested that an intrinsically time-varying random process was not required to model Poisson like activity of cortical neurons.

An average *balance between incoming excitatory and inhibitory* synaptic inputs was sufficient to explain the Poisson like behavior (Gerstain and Mandelbrot, 1964). In brief, they suggested that as the incoming synaptic inputs bombard the postsynaptic neurons, the membrane potential fluctuates close to an absorbing boundary (the spiking threshold of the neuron). The fluctuations produced by slight differences between excitatory and inhibitory inputs were sufficient to drive the neurons into irregular spiking.

¹also known for his contribution to discrete dynamical systems, Mandelbrot sets, fractal geometry, and chaos theory

Excitation Inhibition Balance

Excitation Inhibition (EI) balance is the property of the nervous system to maintain the ratio between excitation and inhibition across a range of conditions or time. The earliest usage of the term “excitation-inhibition balance” comes from ideas of a British psychologist Hans Eysenck (Eysenck, 1955, 1963), who was inspired by Ivan Pavlov’s work on excitation and inhibition in dogs. By studying patients and over 700 soldiers at Maudsley psychiatric hospital in London, he deduced that personality traits could be categorized into 2 axes: the Extroversion-Introversion axis and the Unstable-Stable axis. Putting this data and other data from twin studies, he proposed that the Extroversion-Introversion axis was linked to the observations of differences in Excitation and Inhibition in the Autonomic Nervous System. His key idea was that Extroverts have fast excitation and slow inhibition, while introverts have slow excitation and fast inhibition, which he proposed comes via the reticular formation, thought at the time to be responsible for personality and arousal.

Around the same time, this idea of excitation-inhibition balance was taken up by (Gerstain and Mandelbrot, 1964) to explain the irregular firing of cortical neurons. The effect of Excitation Inhibition balance at the level of the single neuron and its relation to the neural code was theoretically considered by (Shadlen and Newsome, 1994; van Vreeswijk and Sompolinsky, 1996). (Shadlen and Newsome, 1994) built upon the model presented by (Gerstain and Mandelbrot, 1964), along with an important observation that there was at least an order of magnitude difference between the number of excitatory inputs required to make a neuron spike, and the number of excitatory inputs that are active on a neuron in short periods. Below is a quote from (Shadlen and Newsome, 1994):

“Presumably, a balance between active dendritic conductances and cable properties yields a fairly stereotyped EPSP at the soma [62*]. Thus, the available data suggest that the entire dendritic tree may be capable of influencing somatic membrane potential in steps of approximately 0.5mV If so, just 10-40 excitatory inputs can depolarize the membrane from resting potential to a spike threshold of about -55 mV [47,49], yet hundreds of excitatory inputs probably bombard the postsynaptic cell during very brief epochs.”

They compared between two properties of neurons that could explain cortical Poisson spike-trains. First, neurons could function as coincidence detectors at fast timescales. That is, neurons only reach the spiking threshold when hundreds of randomly distributed inputs are received in short bursts. Alternatively, neurons could be embedded in a network of integrate-and-fire units with inhibition. In the first case, the low coincidence between inputs led to the observed spike statistics, and in the second case, inhibitory input balancing excitatory input led to a large number of inputs getting filtered out, leading to this spike time distribution. However, for the coincidence detection model to work, the neurons required an unrealistically short (< 1ms) membrane integration time.

Van Vreesjwik and Haim Sompolinsky showed that if the mean excitation and mean inhibition received by a neuron were correlated (also called **global EI balance**) at timescales of the order of membrane decay constant (of the order of **10 ms**) (also called **loose EI balance**), the spiking in leaky integrate and fire (LIF) neurons was, in fact, chaotic, which could explain the Poisson spiking activity (van Vreeswijk and Sompolinsky, 1996). However, there is an important corollary of this model: spike times in case of coincidence detection neurons are precise and carry information about the coincidence, and the spike times for loosely-globally balanced EI networks are imprecise and don't carry information. The information is in the average rate of firing of a population of such neurons.

While this was able to explain the Poisson-like spike trains, this system seemed like a poor choice for a neural code. This is because if the firing-rate based neural code is to be decoded downstream, the decoder would need an integration time proportional to the square root of the firing rate of the upstream neurons. This is because the variance for a Poisson spiking neuron is proportional to its average firing rate. Also, a firing rate based decoder must integrate over time to ascertain the rate code with accuracy. In another perspective, a spike-rate code is a spike-time code with a poor measurement resolution decoder. This assumes that the spikes could be randomly distributed in a period defined by measurement time of the decoder neurons, say, their membrane time constant. In this perspective, neurons are either too noisy to respond precisely to an incoming stimulus; or neurons can respond precisely, but their precise spike-times don't carry information.

The first major challenge this idea of loose EI balance was the measurement of intracellular EI balance by Anthony Zador. He noted that intracellularly recorded excitatory and inhibitory currents were tightly proportional (Wehr and Zador, 2003). Moreover, these synaptic inputs were both co-tuned to the set of stimuli that drove responses (*receptive fields*) in the rat auditory cortical pyramidal neurons. However, surprisingly, they observed that inhibition followed excitation in a stereotyped sequence, with a delay an order of magnitude smaller than the membrane time constant (**1 - 4 ms**). This phenomenon is now called **tight EI balance**. Inhibition thus reduced temporal imprecision in spiking, rather than increase it, as had been proposed in models above. It is also known now that this tight correlation between EI balance emerges early in development in the rat auditory cortex in a stimulus-dependent manner, and can be observed at around 3 weeks postnatal (Dorrn et al., 2010).

In addition, the reasons for imprecise spike times as a coding strategy, were unsatisfactory, due to other reasons discussed above. It was observed that neurons are capable of producing a neural code that is precise in timing (Mainen and Sejnowski, 1995). Randomly injected excitatory and inhibitory currents at the soma of neocortical neurons were able to reliably generate precise spike

times. Further, it was observed that spike times carried information about the stimulus. In fact, for OFF Ganglion cells (Fig. 4, (Gollisch and Meister, 2008)), stimulus image recovery was more accurate using relative latency of spikes, than spike counts from recordings of salamander retina. Similar observations were made for hippocampus place cells (O’Keefe, Lisman): Spike latencies from theta (phase code) considerably improve location decoding accuracy.

A precise EI balance (as opposed to loose and global) balance between excitation and inhibition mitigates these problems (Hennequin et al., 2017), while retaining the properties of Poisson spiking under some circumstances. Precise balance is defined as the condition where the EI balance is at fast (**<10ms**) timescales (tight EI balance) and random subsets of inputs from the presynaptic network are balanced, i.e., give proportional excitation and inhibition at the postsynaptic neurons (**detailed EI balance**). Recent ideas about neural coding in the brain have considered such a precise EI balance as a central organizing principle. Tim Vogels and Sophie Deneve independently suggested efficient encoding principles which rely on a precise balance between excitation and inhibition (Boerlin et al., 2013; Vogels and Abbott, 2009). (Boerlin et al., 2013) showed that for a recurrently connected set of neurons precisely balanced for excitation and inhibition, Poisson firing rate emerges as an epiphenomenon of an efficient neural code.

Tim Vogels also suggested an Excitatory dependent inhibitory plasticity rule that may exist in the cortices, that keeps the I/E ratio maintained at a homeostatic set-point (Vogels et al., 2011). Recent evidence from Rob Froemke (D’amour and Froemke, 2015) suggests that there is indeed such a homeostatic mechanism in the auditory cortex. (D’amour and Froemke, 2015) measured the receptive fields of auditory cortical principle neurons while playing different frequencies of sounds. They observed the same co-tuned *tightly balanced* excitatory and inhibitory synaptic currents matching the receptive fields of these neurons. Then, they artificially caused synaptic plasticity in these neurons by injecting current into them, while playing a frequency of sound that was not preferred by these neurons. They were able to shift the receptive fields towards the new frequency and obser-

ved that the excitatory currents to these neurons also shifted from their tuning curve peak frequency to this new tuning curve. Surprisingly, they found that inhibition to the neuron also readjusted to the new excitatory tuning-curve in the order of ~10 mins, suggesting homeostatic maintenance of the I/E ratios in neurons. They showed that this was due to an excitation-dependent heterosynaptic plasticity rule.

The next step in understanding the structure of EI balance in the brain was to show the existence of precise EI balance in the brain and establish the source of EI balance. It was unclear if the excitatory-inhibitory balance is maintained in the structure of connectivity at a single presynaptic layer, or only in-vivo, in the presence of real-world stimuli, or due to continuous dynamics of various neuronal layers acting together. We decided to ask this question in the *hippocampus*, known for its well defined layered architecture and central importance in learning and memory.

Hippocampus

The hippocampus is a deep-brain structure in the temporal lobe associated with spatiotemporal encoding and episodic memory. Before 1950s, the hippocampus was associated with olfaction, but the landmark study published by William Scoville and Brenda Milner (Scoville and Milner, 1957) on patient H.M., established the role of hippocampus as the brain region responsible for episodic memory. Patient H.M. had been operated for epileptic seizures originating from the temporal lobe. To alleviate this, H.M.'s hippocampi were bilaterally removed. This lead to a severe and specific deficit in the formation of long term episodic memory. About a decade later, (O'Keefe and Dostrovsky, 1971) showed that the picture for rodents was somewhat different: hippocampal CA1 neurons were encoding a spatial map. Using unit recordings in behaving rats, they showed that certain CA1 neurons called *place cells* selectively and robustly fired, i.e., showed receptive fields for specific locations. They also discovered that this hippocampal place cell neural code is a mixture of both rate and temporal information (Huxter et al., 2003): place cells encode place and velocity

information independently in timing with reference to theta phase and their firing rate respectively. Soon after this, Edvard and May-Britt Moser (Hafting et al., 2005), showed cells in the Entorhinal cortex (EC) which synapsed on to the hippocampal CA1 directly and indirectly (via dentate gyrus and CA3) were also encoding spatial information. They discovered that these cells were active regularly in their environment to a specific spatial frequency, arranged in the form of a uniformly spaced hexagonal lattice, and called them *grid cells*. Recently it has also been discovered that the hippocampus encodes sequences of events by the representation of intervals of time by the sequential activity of cells in the CA1 called time cells (Modi et al., 2014; MacDonald et al., 2011). Given that the nature of hippocampal neural code is reliable, at least in part temporal, and that it itself encodes temporal intervals, hints towards a fine control of membrane potential dynamics. Such fine control of membrane potential dynamics can be possible by the existence of **precisely balanced excitation and inhibition**. Precise EI balance can dampen out large fluctuations in the V_m which can lead to random spiking.

Further, it is still unclear how hippocampal CA1 cells become place cells. (Lee et al., 2012) showed that arbitrary CA1 cells could be converted into place cells by a spatially uniform depolarizing current injection into a silent (non-place) CA1 cell. This was later shown to be possible for arbitrary locations in the behavior arena (Bittner et al., 2015). This implies that most cells in the hippocampus receive inputs for different locations in space, but only some are naturally chosen to become place cells, while others end up remaining silent cells. Again, a possible mechanism for this could be precisely balanced excitation and inhibition in the CA3-CA1 circuit. Precisely tuned inhibition can maintain the activity levels within neurons, giving them potential (but subdued) receptive fields for all locations that an animal traverses. However, a select subset of neurons become place cells, as the inhibition to excitation ratio reduces, a phenomenon known as *inhibitory gating*.

Fig. 1.6 shows the reduced hippocampal CA3-CA1 network. In this network, CA3 pyramidal neurons send excitatory synapses to both CA1 pyramidal neurons and CA1 interneurons. CA1

interneurons, in turn, inhibit the CA1 pyramidal neurons, completing the feedforward inhibitory loop.

Hippocampal CA3-CA1 network

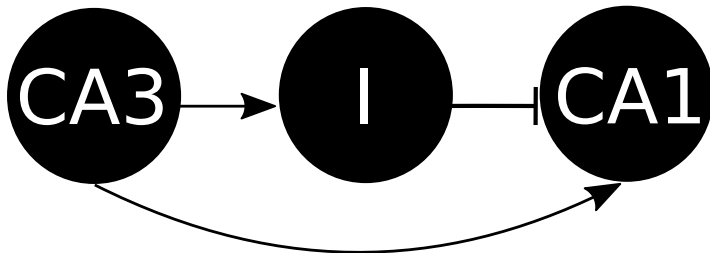


Figure 1.6: The feedforward inhibitory hippocampal CA3-CA1 network. The arrow-head edges represent excitation and the flat-head edge represents inhibition.

Precise EI balance and Subthreshold Divisive Normalization

We wanted to ask if **precise EI balance** exists in the brain. To answer this question, we needed to stimulate many subsets of presynaptic inputs, while recording synaptic currents from postsynaptic neurons. To do this, we used patterned optical stimulation to stimulate channelrhodopsin expressing hippocampal CA3 neurons in hundreds of different combinations. Channelrhodopsin is a light-sensitive ion channel that conducts in the presence of blue light and was expressed selectively in the hippocampal CA3 cells using a *Cre-lox* setup (Boyden et al., 2005). CA3 neurons impinge on CA1 neurons via a direct excitatory pathway, and an indirect disynaptic inhibitory pathway (Figure 1.6). Then, we recorded from CA1 neurons intracellularly using whole-cell patch-clamp and recorded excitatory and inhibitory postsynaptic currents.

We found that **randomly chosen groups of cells in CA3 gave precisely balanced excitation and inhibition to CA1** (Chapter 3). We also showed that given the statistics of the hippocampal CA3-CA1 network connectivity and release probability, the emergence of precise E/I balance is non-trivial and needs to be maintained at the level of tens of synapses. The discovery of this structured input in the brain implies that individual layers in the brain may be independently EI

balanced. This has important implications on our understanding of neuronal communication and opens up a lot of new questions concerning both the emergence and the role of this balanced state in the brain.

Moreover, we found that the window of opportunity for integration in a neuron changes dynamically in this balanced regime, based on the input amplitude. An increase in input amplitude causes a proportionally smaller delay between excitation and inhibition (Chapter 3).

In combination, the twin observations of precise EI balance and EI delay lead to a normalization operation at the subthreshold regime, which leads to gain-control and a transformation of information from amplitude to time, called **Subthreshold Divisive Normalization (SDN)**, which can be approximated by the following equation:

$$O = \frac{\gamma E}{\gamma + E}$$

where O is the observed PSP from the neuron, E is the expected sum of individual EPSPs, and γ is the measurable normalization parameter, which depends on I/E ratio, the rate of change of EI delay with input amplitude, reversal potentials of synaptic channels and the synaptic timecourses.

In summary, we propose that there is a spectrum of balance for neural networks:

1. **Resolution of synaptic currents:** This ranges from *global balance*, where synaptic currents are balanced only on average, to *detailed balance* where all subsets of inputs from a presynaptic network impinge on the postsynaptic neurons to give rise to balanced excitation and inhibition.
2. **Timescale:** *Loose balance* (slow $\sim O(>10 \text{ ms})$) to *tight balance* at fast ($\sim O(<10 \text{ ms})$ timescales)
3. **Inhibition type:** Feedback or feedforward
4. **Number:** Number of excitatory and inhibitory synaptic inputs impinging on the postsynaptic neuron

Detailed and *tight* balance together are called *precise EI balance*. The first three are discussed in (Hennequin et al., 2017) but the fourth type remains unattended. There are important theoretical consequences of having different numbers of synaptic inputs. This is because, for synapses with low release probability, a large number of small weight synapses will have different trial-to-trial variability, than a small number of large weight synapses, even though the average synaptic weight over trials is identical.

Subthreshold computation

Our observations further the suggestion that neurons with spike-time codes can compute with their spike time employing subthreshold computational schemes like SDN. We had two key findings in this regard: first, a tightly maintained correlation in the amplitude of excitatory and inhibitory synaptic currents, and second, excitation dependent inhibitory delay. Together, these make the window of opportunity for spiking dynamic. Neurons at large input amplitudes have a narrow window of opportunity. Thus, they function more like coincidence detectors, bestowing the neurons with precise spike-times. For smaller inputs, neurons have a wide window of opportunity, allowing for a large dynamic range of the integrate-and-fire neurons. Further, Subthreshold Divisive Normalization allows the neurons to maintain a economic spike-time code, by clamping the subthreshold activity of the neuron in proportion to the excitatory input received.

Thus, neurons are likely **neither just integrate-and-fire, nor coincidence detectors, but stand dynamically between the two, due to the variable delay between excitation and inhibition** we observed. Second, at least across the Feed-forward loop from $CA3 \rightarrow CA1$, **neurons transmit information about their input in the timing of their postsynaptic potentials**, due to the existence of SDN (Bhatia, Moza, and Bhalla, 2019).

Inhibitory gating

Lastly, we propose that stimulus-induced neuronal firing results as an opening of the I/E balance gate: the breaking of E/I balance. Neural networks sit balanced and take trajectories away from this balanced state to communicate information across the nervous system and for plasticity. This allows neurons to have a combinatorially large number of potential receptive fields. Only a handful number of synapses can drive a neuron precisely and selectively, even though the neuron is being bombarded with hundreds of excitatory inputs.

Thus, I have described above the evolution of thought about excitation-inhibition balance in the context of neural coding: from the current that broadly clamps down excitation, to the current that sculpts the activity of the nervous system at different timescales. How this symmetry in excitation and inhibition constrain the network structure and learning rules is yet to be seen. In one perspective, the homeostatically maintained E/I balance could set the *learning rate* for the neurons. Neurons with high I/E ratios are less likely to fire and undergo plasticity. Synaptic weights need to change with each surprise in the world: this is when the neurons exit the balanced regime and fire a larger number of spikes, possibly due to disinhibition or short-term facilitation/depression, inducing long-term plasticity. However, the homeostatic balance of I/E ratios is eventually regained, as the inhibition follows up and plugs the excess excitation, maintaining the E/I balance.

In summary, I have outlined two investigations in this thesis. First, I discuss the topological and parametric determinants of the robustness of bistable chemical reaction networks. In this study, I looked at the exhaustive chemistry possible made of networks of up to 6 reactions between up to 4 molecules. I found that on average, the topology that determines different forms of robustness are different, however, the presence of certain subnetworks can increase both structural and parametric robustness. We also found that a symmetric network with competitive autocatalysis was conducive to addition of more edges to form larger bistable networks, and had high robustness to parametric fluctuations chemical reaction networks.

Second, I discuss information propagation in a feedforward inhibitory loop neuronal network in the hippocampal CA3-CA1. In this study, we discovered that the CA3-CA1 feedforward inhibitory network in the hippocampus has precise excitatory-inhibitory balance. Further, we discovered a novel subthreshold gain-control computation that exists in the hippocampus that results from this motif. Since the subthreshold state of the neuron can be compared to chemical reaction networks due to their smooth, continuous nature, perhaps inspiration can be drawn from chemical reaction networks for architectures other than feedforward networks to make predictions about other sub-threshold computations.

Note: Figures in this section were made using Python, and graphs were generated using networkx (Hagberg et al., 2008)

Bibliography

E. D. Adrian and Yngve Zotterman. The impulses produced by sensory nerve-endings. *The Journal of Physiology*, 61(2):151–171, apr 1926. doi: 10.1113/jphysiol.1926.sp002281. URL <https://doi.org/10.1113/jphysiol.1926.sp002281>.

Réka Albert and Albert-László Barabási. Statistical mechanics of complex networks. *Reviews of Modern Physics*, 74(1):47–97, jan 2002. doi: 10.1103/revmodphys.74.47. URL <https://doi.org/10.1103/revmodphys.74.47>.

Uri Alon. *An Introduction to Systems Biology: Design Principles of Biological Circuits*. Chapman & Hall/CRC, London, 2007. ISBN 1584886420.

Michael J. Aminoff. The life and legacy of Brown-Séquard. *Brain*, 140(5):1525–1532, apr 2017. doi: 10.1093/brain/awx071. URL <https://doi.org/10.1093/brain/awx071>.

P. Anderson and John Eccles. Inhibitory Phasing of Neuronal Discharge. *Nature*, 196(4855):

645–647, nov 1962. doi: 10.1038/196645a0. URL <https://doi.org/10.1038%2F196645a0>.

P. W. Anderson. More Is Different. *Science*, 177(4047):393–396, aug 1972. doi: 10.1126/science.177.4047.393. URL <https://doi.org/10.1126%2Fscience.177.4047.393>.

SS Andrews, NJ Addy, R Brent, and AP Arkin. Detailed simulations of cell biology with Smoldyn 2.1. *PLoS Comput Biol*, 6:e1000705, Mar 2010.

Marco Tulio Angulo, Yang-Yu Liu, and Jean-Jacques Slotine. Network motifs emerge from interconnections that favour stability. *Nature Physics*, 11(10):848–852, jul 2015. doi: 10.1038/nphys3402. URL <https://doi.org/10.1038%2Fnphys3402>.

AL Barabasi and R Albert. Emergence of scaling in random networks. *Science*, 286:509–12, Oct 1999.

A Becskei and L Serrano. Engineering stability in gene networks by autoregulation. *Nature*, 405:590–3, Jun 2000.

A Becskei, B Séraphin, and L Serrano. Positive feedback in eukaryotic gene networks: cell differentiation by graded to binary response conversion. *EMBO J*, 20:2528–35, May 2001.

U. S. Bhalla and Ravi Iyengar. Emergent Properties of Networks of Biological Signaling Pathways. *Science*, 283(5400):381–387, jan 1999. doi: 10.1126/science.283.5400.381. URL <https://doi.org/10.1126%2Fscience.283.5400.381>.

A Bhatia, S Moza, and US Bhalla. Precise excitation-inhibition balance controls gain and timing in the hippocampus. *Elife*, 8, Apr 2019.

Katie C Bittner, Christine Grienberger, Sachin P Vaidya, Aaron D Milstein, John J Macklin, Junghyup Suh, Susumu Tonegawa, and Jeffrey C Magee. Conjunctive input processing drives

- feature selectivity in hippocampal CA1 neurons. *Nature Neuroscience*, 18(8):1133–1142, jul 2015. doi: 10.1038/nn.4062. URL <https://doi.org/10.1038%2Fnn.4062>.
- C Blakemore and EA Tobin. Lateral inhibition between orientation detectors in the cat’s visual cortex. *Exp Brain Res*, 15:439–40, 1972.
- M Boerlin, CK Machens, and S Denève. Predictive coding of dynamical variables in balanced spiking networks. *PLoS Comput Biol*, 9:e1003258, 2013.
- Edward S Boyden, Feng Zhang, Ernst Bamberg, Georg Nagel, and Karl Deisseroth. Millisecond-timescale genetically targeted optical control of neural activity. *Nature Neuroscience*, 8 (9):1263–1268, aug 2005. doi: 10.1038/nn1525. URL <https://doi.org/10.1038%2Fnn1525>.
- O Braganza and H Beck. The Circuit Motif as a Conceptual Tool for Multilevel Neuroscience. *Trends Neurosci*, 41:128–136, Mar 2018.
- L. G. Brock, J. S. Coombs, and J. C. Eccles. The recording of potentials from motoneurones with an intracellular electrode. *The Journal of Physiology*, 117(4):431–460, aug 1952. doi: 10.1113/jphysiol.1952.sp004759. URL <https://doi.org/10.1113%2Fjphysiol.1952.sp004759>.
- CE Brown-Séquard. Remarques à propos des recherches du Dr. F.W. Mott sur les effets de la section d’une moitié latérale de la moelle épinière. *Arch Physiol Norm Pathol*, 6, 1894.
- Simon J.B Butt, James M Lebret, and Ole Kiehn. Organization of left-right coordination in the mammalian locomotor network. *Brain Research Reviews*, 40(1-3):107–117, oct 2002. doi: 10.1016/s0165-0173(02)00194-7. URL <https://doi.org/10.1016%2Fs0165-0173%2802%2900194-7>.
- OX Cordero and P Hogeweg. Feed-forward loop circuits as a side effect of genome evolution. *Mol*

Biol Evol, 23:1931–6, Oct 2006.

James A. D'amour and Robert C. Froemke. Inhibitory and Excitatory Spike-Timing-Dependent Plasticity in the Auditory Cortex. *Neuron*, 86(2):514–528, apr 2015. doi: 10.1016/j.neuron.2015.03.014. URL <https://doi.org/10.1016/j.neuron.2015.03.014>.

A.F. Dean. The variability of discharge of simple cells in the cat striate cortex. *Experimental Brain Research*, 44(4), dec 1981. doi: 10.1007/bf00238837. URL <https://doi.org/10.1007/bf00238837>.

Sven Dorkenwald, Nicholas L. Turner, Thomas Macrina, Kisuk Lee, Ran Lu, Jingpeng Wu, Agnes L. Bodor, Adam A. Bleckert, Derrick Brittain, Nico Kemnitz, William M. Silver-smith, Dodam Ih, Jonathan Zung, Aleksandar Zlateski, Ignacio Tartavull, Szi-Chieh Yu, Sergiy Popovych, William Wong, Manuel Castro, Chris S. Jordan, Alyssa M. Wilson, Emmanouil Froudarakis, JoAnn Buchanan, Marc Takeno, Russel Torres, Gayathri Mahalingam, Forrest Collman, Casey Schneider-Mizell, Daniel J. Bumbarger, Yang Li, Lynne Becker, Shelby Suckow, Jacob Reimer, Andreas S. Tolias, Nuno Maçarico da Costa, R. Clay Reid, and H. Sebastian Seung. Binary and analog variation of synapses between cortical pyramidal neurons. dec 2019. doi: 10.1101/2019.12.29.890319. URL <https://doi.org/10.1101/2019.12.29.890319>.

Anja L. Dorrn, Kexin Yuan, Alison J. Barker, Christoph E. Schreiner, and Robert C. Froemke. Developmental sensory experience balances cortical excitation and inhibition. *Nature*, 465(7300):932–936, jun 2010. doi: 10.1038/nature09119. URL <https://doi.org/10.1038/nature09119>.

Niraj Dudani, Upinder S. Bhalla, and Subhasis Ray. MOOSE the Multiscale Object-Oriented Simulation Environment. In *Encyclopedia of Computational Neuroscience*, pages 1751–1754. Springer New York, 2015. doi: 10.1007/978-1-4614-6675-8_257. URL https://doi.org/10.1007/978-1-4614-6675-8_257.

[org/10.1007%2F978-1-4614-6675-8_257](https://doi.org/10.1007%2F978-1-4614-6675-8_257).

J Elf and M Ehrenberg. Fast evaluation of fluctuations in biochemical networks with the linear noise approximation. *Genome Res*, 13:2475–84, Nov 2003.

Eliasz Engelhardt. Brown-Séquard: On neural networks and brain localization of functions. *Dementia & Neuropsychologia*, 8(1):79–82, mar 2014. doi: 10.1590/s1980-57642014dn81000012. URL <https://doi.org/10.1590%2Fs1980-57642014dn81000012>.

H. J. Eysenck. A Dynamic Theory of Anxiety and Hysteria. *Journal of Mental Science*, 101(422):28–51, jan 1955. doi: 10.1192/bjp.101.422.28. URL <https://doi.org/10.1192%2Fbjp.101.422.28>.

H. J. Eysenck. Biological Basis of Personality. *Nature*, 199(4898):1031–1034, sep 1963. doi: 10.1038/1991031a0. URL <https://doi.org/10.1038%2F1991031a0>.

JE Jr Ferrell and EM Machleider. The biochemical basis of an all-or-none cell fate switch in *Xenopus* oocytes. *Science*, 280:895–8, May 1998.

GL Gerstain and B Mandelbrot. Random walk models for the spike activity of a single neuron. *Biophys J*, 4:41–68, Jan 1964.

Daniel T. Gillespie. Exact stochastic simulation of coupled chemical reactions. *The Journal of Physical Chemistry*, 81(25):2340–2361, dec 1977. doi: 10.1021/j100540a008. URL <https://doi.org/10.1021%2Fj100540a008>.

L Goentoro, O Shoval, MW Kirschner, and U Alon. The incoherent feedforward loop can provide fold-change detection in gene regulation. *Mol Cell*, 36:894–9, Dec 2009.

T. Gollisch and M. Meister. Rapid Neural Coding in the Retina with Relative Spike Latencies. *Science*, 319(5866):1108–1111, feb 2008. doi: 10.1126/science.1149639. URL <https://doi.org/10.1126%2Fscience.1149639>.

- Torkel Hafting, Marianne Fyhn, Sturla Molden, May-Britt Moser, and Edvard I. Moser. Microstructure of a spatial map in the entorhinal cortex. *Nature*, 436(7052):801–806, jun 2005. doi: 10.1038/nature03721. URL <https://doi.org/10.1038%2Fnature03721>.
- Aric A. Hagberg, Daniel A. Schult, and Pieter J. Swart. Exploring Network Structure, Dynamics, and Function using NetworkX. In Gaël Varoquaux, Travis Vaught, and Jarrod Millman, editors, *Proceedings of the 7th Python in Science Conference*, pages 11 – 15, Pasadena, CA USA, 2008.
- Guillaume Hennequin, Everton J. Agnes, and Tim P. Vogels. Inhibitory Plasticity: Balance Control, and Codependence. *Annual Review of Neuroscience*, 40(1):557–579, jul 2017. doi: 10.1146/annurev-neuro-072116-031005. URL <https://doi.org/10.1146%2Fannurev-neuro-072116-031005>.
- Takao K. Hensch and Michela Fagiolini, editors. *Excitatory-Inhibitory Balance*. Springer US, 2004. doi: 10.1007/978-1-4615-0039-1. URL <https://doi.org/10.1007%2F978-1-4615-0039-1>.
- D. H. Hubel and T. N. Wiesel. Receptive fields binocular interaction and functional architecture in the cat's visual cortex. *The Journal of Physiology*, 160(1):106–154, jan 1962. doi: 10.1113/jphysiol.1962.sp006837. URL <https://doi.org/10.1113%2Fjphysiol.1962.sp006837>.
- J Huxter, N Burgess, and J O'Keefe. Independent rate and temporal coding in hippocampal pyramidal cells. *Nature*, 425:828–32, Oct 2003.
- PJ Ingram, MP Stumpf, and J Stark. Network motifs: structure does not determine function. *BMC Genomics*, 7:108, May 2006.
- N.G. Van Kampen. Stochastic processes. In *Stochastic Processes in Physics and Chemistry*, pages 52–72. Elsevier, 2007. doi: 10.1016/b978-044452965-7/50006-4. URL <https://doi.org/10.1016%2Fb978-044452965-7%2F50006-4>.

RA Kerr, TM Bartol, B Kaminsky, M Dittrich, JC Chang, SB Baden, TJ Sejnowski, and JR Stiles.
FAST MONTE CARLO SIMULATION METHODS FOR BIOLOGICAL REACTION-DIFFUSION SYSTEMS IN SOLUTION AND ON SURFACES. *SIAM J Sci Comput*, 30:3126, Oct 2008.

Minoru Koyama, Francesca Minale, Jennifer Shum, Nozomi Nishimura, Chris B Schaffer, and Joseph R Fetcho. A circuit motif in the zebrafish hindbrain for a two alternative behavioral choice to turn left or right. *eLife*, 5, aug 2016. doi: 10.7554/elife.16808. URL <https://doi.org/10.7554%2Felife.16808>.

K Lai, MJ Robertson, and DV Schaffer. The sonic hedgehog signaling system as a bistable genetic switch. *Biophys J*, 86:2748–57, May 2004.

Novère N Le, M Hucka, H Mi, S Moodie, F Schreiber, A Sorokin, E Demir, K Wegner, MI Aladjem, SM Wimalaratne, FT Bergman, R Gauges, P Ghazal, H Kawaji, L Li, Y Matsuoka, A Villéger, SE Boyd, L Calzone, M Courtot, U Dogrusoz, TC Freeman, A Funahashi, S Ghosh, A Jouraku, S Kim, F Kolpakov, A Luna, S Sahle, E Schmidt, S Watterson, G Wu, I Goryanin, DB Kell, C Sander, H Sauro, JL Snoep, K Kohn, and H Kitano. The Systems Biology Graphical Notation. *Nat Biotechnol*, 27:735–41, Aug 2009.

D. Lee, B.-J. Lin, and A. K. Lee. Hippocampal Place Fields Emerge upon Single-Cell Manipulation of Excitability During Behavior. *Science*, 337(6096):849–853, aug 2012. doi: 10.1126/science.1221489. URL <https://doi.org/10.1126%2Fscience.1221489>.

J. E. Lisman. A mechanism for memory storage insensitive to molecular turnover: a bistable autophosphorylating kinase. *Proceedings of the National Academy of Sciences*, 82(9):3055–3057, may 1985. doi: 10.1073/pnas.82.9.3055. URL <https://doi.org/10.1073%2Fpnas.82.9.3055>.

O. Loewi. Über humorale übertragbarkeit der Herznervenwirkung. *Pflügers Archiv für die Gesamte*

- Physiologie des Menschen und der Tiere*, 189(1):239–242, dec 1921. doi: 10.1007/bf01738910.
URL <https://doi.org/10.1007%2Fbf01738910>.
- A. Lundberg. HALF-CENTRES REVISITED. In *Regulatory Functions of the CNS Principles of Motion and Organization*, pages 155–167. Elsevier, 1981. doi: 10.1016/b978-0-08-026814-9.50025-9. URL <https://doi.org/10.1016%2Fb978-0-08-026814-9.50025-9>.
- CJ MacDonald, KQ Lepage, UT Eden, and H Eichenbaum. Hippocampal time cells bridge the gap in memory for discontiguous events. *Neuron*, 71:737–49, Aug 2011.
- ZF Mainen and TJ Sejnowski. Reliability of spike timing in neocortical neurons. *Science*, 268:1503–6, Jun 1995.
- S Mangan and U Alon. Structure and function of the feed-forward loop network motif. *Proc Natl Acad Sci U S A*, 100:11980–5, Oct 2003.
- S Mangan, S Itzkovitz, A Zaslaver, and U Alon. The incoherent feed-forward loop accelerates the response-time of the gal system of Escherichia coli. *J Mol Biol*, 356:1073–81, Mar 2006.
- D. Marr and T. Poggio. From Understanding Computation to Understanding Neural Circuitry. Technical report, Cambridge, MA, USA, 1976.
- R Milo, S Shen-Orr, S Itzkovitz, N Kashtan, D Chklovskii, and U Alon. Network motifs: simple building blocks of complex networks. *Science*, 298:824–7, Oct 2002.
- MN Modi, AK Dhawale, and US Bhalla. CA1 cell activity sequences emerge after reorganization of network correlation structure during associative learning. *Elife*, 3:e01982, Mar 2014.
- J. O'Keefe and J. Dostrovsky. The hippocampus as a spatial map. Preliminary evidence from unit activity in the freely-moving rat. *Brain Research*, 34(1):171–175, nov 1971. doi: 10.1016/0006-8993(71)90358-1. URL <https://doi.org/10.1016%2F0006-8993%2871%2990358-1>.

David Parker and Sten Grillner. Neuronal mechanisms of synaptic and network plasticity in the lamprey spinal cord. In *Progress in Brain Research*, pages 381–398. Elsevier, 2000. doi: 10.1016/s0079-6123(00)25027-9. URL <https://doi.org/10.1016%2Fs0079-6123%2800%2925027-9>.

Joshua L. Payne and Andreas Wagner. Function does not follow form in gene regulatory circuits. *Scientific Reports*, 5(1), aug 2015. doi: 10.1038/srep13015. URL <https://doi.org/10.1038%2Fsrep13015>.

RJ Prill, PA Iglesias, and A Levchenko. Dynamic properties of network motifs contribute to biological network organization. *PLoS Biol*, 3:e343, Nov 2005.

N Ramakrishnan and US Bhalla. Memory switches in chemical reaction space. *PLoS Comput Biol*, 4:e1000122, Jul 2008.

Subhasis Ray, Raamesh Deshpande, Niraj Dudani, and Upinder S Bhalla. A general biological simulator: the multiscale object oriented simulation environment MOOSE. *BMC Neuroscience*, 9(Suppl 1):P93, 2008. doi: 10.1186/1471-2202-9-s1-p93. URL <https://doi.org/10.1186%2F1471-2202-9-s1-p93>.

M Santolini and AL Barabási. Predicting perturbation patterns from the topology of biological networks. *Proc Natl Acad Sci U S A*, 115:E6375–E6383, Jul 2018.

W. B. Scoville and B. Milner. LOSS OF RECENT MEMORY AFTER BILATERAL HIPPOCAMPAL LESIONS. *Journal of Neurology Neurosurgery & Psychiatry*, 20(1):11–21, feb 1957. doi: 10.1136/jnnp.20.1.11. URL <https://doi.org/10.1136%2Fjnnp.20.1.11>.

MN Shadlen and WT Newsome. Noise, neural codes and cortical organization. *Curr Opin Neurobiol*, 4:569–79, Aug 1994.

Charles S. Sherrington. *The integrative action of the nervous system*. Yale University Press, 1906.

doi: 10.1037/13798-000. URL <https://doi.org/10.1037%2F13798-000>.

O Shoval and U Alon. SnapShot: network motifs. *Cell*, 143:326–e1, Oct 2010.

Olaf Sporns and Rolf Kötter. Motifs in Brain Networks. *PLoS Biology*, 2(11):e369, oct 2004.
doi: 10.1371/journal.pbio.0020369. URL <https://doi.org/10.1371%2Fjournal.pbio.0020369>.

D.J. Tolhurst, J.A. Movshon, and A.F. Dean. The statistical reliability of signals in single neurons in cat and monkey visual cortex. *Vision Research*, 23(8):775–785, jan 1983. doi: 10.1016/0042-6989(83)90200-6. URL <https://doi.org/10.1016%2F0042-6989%2883%2990200-6>.

Nicole B. Trunnell, Andy C. Poon, Sun Young Kim, and James E. Ferrell. Ultrasensitivity in the Regulation of Cdc25C by Cdk1. *Molecular Cell*, 41(3):263–274, feb 2011. doi: 10.1016/j.molcel.2011.01.012. URL <https://doi.org/10.1016%2Fj.molcel.2011.01.012>.

C van Vreeswijk and H Sompolinsky. Chaos in neuronal networks with balanced excitatory and inhibitory activity. *Science*, 274:1724–6, Dec 1996.

T. P. Vogels, H. Sprekeler, F. Zenke, C. Clopath, and W. Gerstner. Inhibitory Plasticity Balances Excitation and Inhibition in Sensory Pathways and Memory Networks. *Science*, 334(6062):1569–1573, nov 2011. doi: 10.1126/science.1211095. URL <https://doi.org/10.1126%2Fscience.1211095>.

TP Vogels and LF Abbott. Gating multiple signals through detailed balance of excitation and inhibition in spiking networks. *Nat Neurosci*, 12:483–91, Apr 2009.

Duncan J. Watts and Steven H. Strogatz. Collective dynamics of 'small-world' networks. In *The*

Structure and Dynamics of Networks. Princeton University Press, dec 2011. doi: 10.1515/9781400841356.301. URL <https://doi.org/10.1515%2F9781400841356.301>.

Ernst Heinrich Weber and Eduard Friedrich Weber. Experimenta quibus probata nervos vagos rotatione machinae galvano-magneticae irritatos, motum cordis retardare et adeo intercipere. *Omodei's Ann. univ. de med., Milan*, 3. s., xx, 227, 1845.

Michael Wehr and Anthony M. Zador. Balanced inhibition underlies tuning and sharpens spike timing in auditory cortex. *Nature*, 426(6965):442–446, nov 2003. doi: 10.1038/nature02116. URL <https://doi.org/10.1038%2Fnature02116>.

Anatol M. Zhabotinsky. Bistability in the Ca²⁺/Calmodulin-Dependent Protein Kinase-Phosphatase System. *Biophysical Journal*, 79(5):2211–2221, nov 2000. doi: 10.1016/s0006-3495(00)76469-1. URL <https://doi.org/10.1016%2Fs0006-3495%2800%2976469-1>.

Chapter 2

Robustness properties of chemical switches

Abstract

Biological systems gather information and carry out computations for self-organization. Large biochemical reaction networks have been selected over billions of years of evolution to carry out these computations. Bistable chemical reaction networks (CRNs) form a fundamental subgroup of these biochemical networks with elementary computational functions such as decision making and memory storage. Bistability can be achieved by several suitable biochemical network architectures. However, each architecture may have different degrees of robustness against different forms of perturbations, that may determine its persistence over evolution. We compared the robustness of all possible bistable CRNs with ≤ 6 reactions between ≤ 3 reactants and 3 reactions between 4 reactants in maintaining bistability against perturbation to the reaction network structure (structural) and reaction rates (parametric). We found that the higher the number of minimal bistable CRNs (called root groups) in the network, the more it was robust to structural perturbations. Further, we discovered that the most parametrically robust networks contained a mirror-symmetric network structure. This symmetry was due to two autocatalytic feedback loops competing for a common substrate. Bistability implies the existence of two steady-states, and the two steady-state concentration vectors of the same CRN may change considerably as the reaction rates are varied. Thus, even

if a CRN has high parametric robustness, the information that the concentrations encode could be lost with perturbations to reaction rates. Thus we calculated state-vector robustness, i.e., the number of unique binarized steady-state concentrations for a CRN across all sets of parameters that gave bistability. We found that several CRNs with high parametric robustness also had low state-vector robustness. However, the mirror-symmetric competitive-autocatalytic feedback loop CRNs also scored high on state-vector robustness. Lastly, we looked at the robustness of bistable CRNs in persisting at a stable fixed point in the presence of various levels of stochastic noise. Since the set of perturbations to evolving biochemical networks may differ according to their microenvironment, their combined robustness to a set of perturbations may dictate the enrichment of functional motifs in biochemical reaction networks. Thus, we compared the structural and parametric robustness of all CRNs. We found that there was a weak correlation between them. However, when grouped according to their root groups, the members of root groups clustered together with similar structural and parametric robustness. We also compared noise robustness with structural and parametric robustness and found very little average correlation with other forms of robustness. In summary, we show that structural and parametric have a weak correlation with each other and no average correlation with noise robustness. However, grouping the CRNs by their root groups revealed patterns in their organization: CRNs which are members of a higher number of root groups have higher structural robustness, CRNs with competitive auto-catalytic feedback-loops have the highest parametric robustness, and CRNs with similar root groups had similar structural and parametric robustness. Further, we reveal a robustness map that can be used to gain insight about diverse questions, such as the structural properties of robust CRNs, comparing alternative CRNs for the synthesis of pure enantiomers from racemic mixtures, for synthetic biology constructs, and to search for computational motifs across different biochemical networks.

Introduction

Biological systems are adept at making decisions and remembering choices in the face of uncertainty. Both decision making and memory formation, two fundamental aspects of the dynamics of biological systems can be made possible by utilizing simple biochemical reaction systems. Decisions can be made by converting analog signals, say rapidly changing Ca^{2+} concentrations, into digital YES/NO signals by *bistable systems*. Bistable systems have two steady states, that can be reached from different starting points. Consequently, these transitions to one of these steady states can determine the decision, such as a given developmental fate of a cell (Bhalla, 2002; Wang et al., 2009). Similarly, memory can be reliably stored in biochemical compartments at various timescales by encoding it in stable reactant and product concentrations, which can be sustained or changed in response to external stimuli. Synapses between neurons have been shown to be structurally bi-modal (Dorkenwald et al., 2019), and synaptic chemistry responsible for long term memory is proposed to have bistable chemistry (Lisman and Zhabotinsky, 2001). Both these functions can be achieved by a chemical reaction system that is *bistable*.

Bistable systems have also been proposed as chemical mechanisms for the observed homochirality in biological systems (DECKER, 1973). Chirality or handedness is the property of certain molecules to be non-superimposable on their mirror reflections, called L and D forms. In most non-biological reactions, molecules are created heterochiral, i.e., with equal fractions of both L and D types. However, in biological systems, molecules such as DNA, RNA, and amino acids are observed to be almost exclusively homochiral, i.e., either only L or only D enantiomers exist. For example, sugars are typically observed in D-enantiomers and amino acids in L-enantiomers. A contending hypothesis (Avetisov and Goldanskii, 1996) claims that homochirality arose chemically before biological complexity. Experimental evidence supporting this hypothesis has accumulated from meteorite samples containing homochiral molecules (Cooper and Rios, 2016) and laboratory synthesis of homochiral molecules (Shibata et al., 1996). Certain small bistable CRNs have

been proposed that use autocatalysis to amplify slight asymmetries in the enantiomeric fraction of the products to create homochiral products from achiral substrates (Frank, 1953; Viedma, 2005). However, a systematic comparison of several small bistable CRNs in this regard has not been undertaken. Further, it is important to understand such proposed mechanisms of homochirality in the context of their robustness against environmental perturbations, as that may be an important determinant of their evolutionary success.

A bistable chemical reaction network (CRN) can be constructed with just two reactions (Ramaskrishnan and Bhalla, 2008). Fig 2.1c shows this minimal bistable chemistry. This forms a feedback reaction motif: a small group of connected nodes present in higher than chance levels in large reaction networks (Milo et al., 2002). Bistability requires the presence of core positive feedback loops (Wilhelm, 2009), and other connections between reactants can alter the stability and robustness of these systems (Pfeuty and Kaneko, 2009). Biochemical reaction networks such as signalling pathways, are exposed to different kinds of perturbations and have evolved to sustain their dynamical behavior (Barkai and Leibler, 1997). Chemical systems can thus be called *robust*, defined as **a property that allows a system to maintain its functions despite external and internal perturbations (Kitano, 2004)**. Perturbations to CRNs can be 1) Structural (or topological): addition, deletions, or mutations in the chemical reactions between reactants in the CRN; 2) Parametric: changes in reaction rates and concentrations of reactants, or 3) By virtue of fluctuations, i.e., intrinsic or extrinsic noise in the system. Robustness to these perturbations can shape the complexity and evolvability of CRNs in biological systems.

Robustness in bistable systems can be attained by augmenting the core feedback network with stabilizing connections. Thus, the diversity of architectures across different biological systems may reflect the *robustness* of the underlying chemical network to the unique set of perturbations in the evolutionary past of that system. For example, in compartments with small volumes such as dendritic spines, thermal noise may constrain a reaction network to have higher noise-robustness,

than in a rapidly replicating genome of a single-stranded RNA virus, that may be more prone to parametric perturbations to combat copying errors. This raises two questions. First, are systems robust to one kind of perturbation also robust to other kinds of perturbations? Second, can the addition of a certain set of reactions coherently increase or decrease multiple forms of robustness?

Here, we exhaustively analyze all bistable reaction systems from the chemistry possible with up to 4 reacting entities and 6 reactions (Ramakrishnan and Bhalla, 2008). Then, we explore the robustness of these small bistable CRNs to changes in the reaction network structure (*topology*), parameters, and intrinsic noise to probe for common network structure between different forms of robustness (Chang et al., 2010; Cheng et al., 2008). We found that constraints posed on CRNs for robustness to different kinds of perturbations selected topologies with different features. Structurally robust topologies generally contained several different core minimal bistable networks called root groups. Root groups are networks that cannot be structurally broken down into smaller bistable networks. We found that the topologies with highest parametric robustness contained a mirror-symmetric structure in the chemical reaction network. This symmetry corresponded to two autocatalytic feedback loops competing for a shared substrate. We propose that the map that we obtained can be used as a guide for designing small CRNs for synthetic biology constructs, for comparing alternative models of enantioselective synthesis, and in general for understanding structural determinants of different forms of robustness.

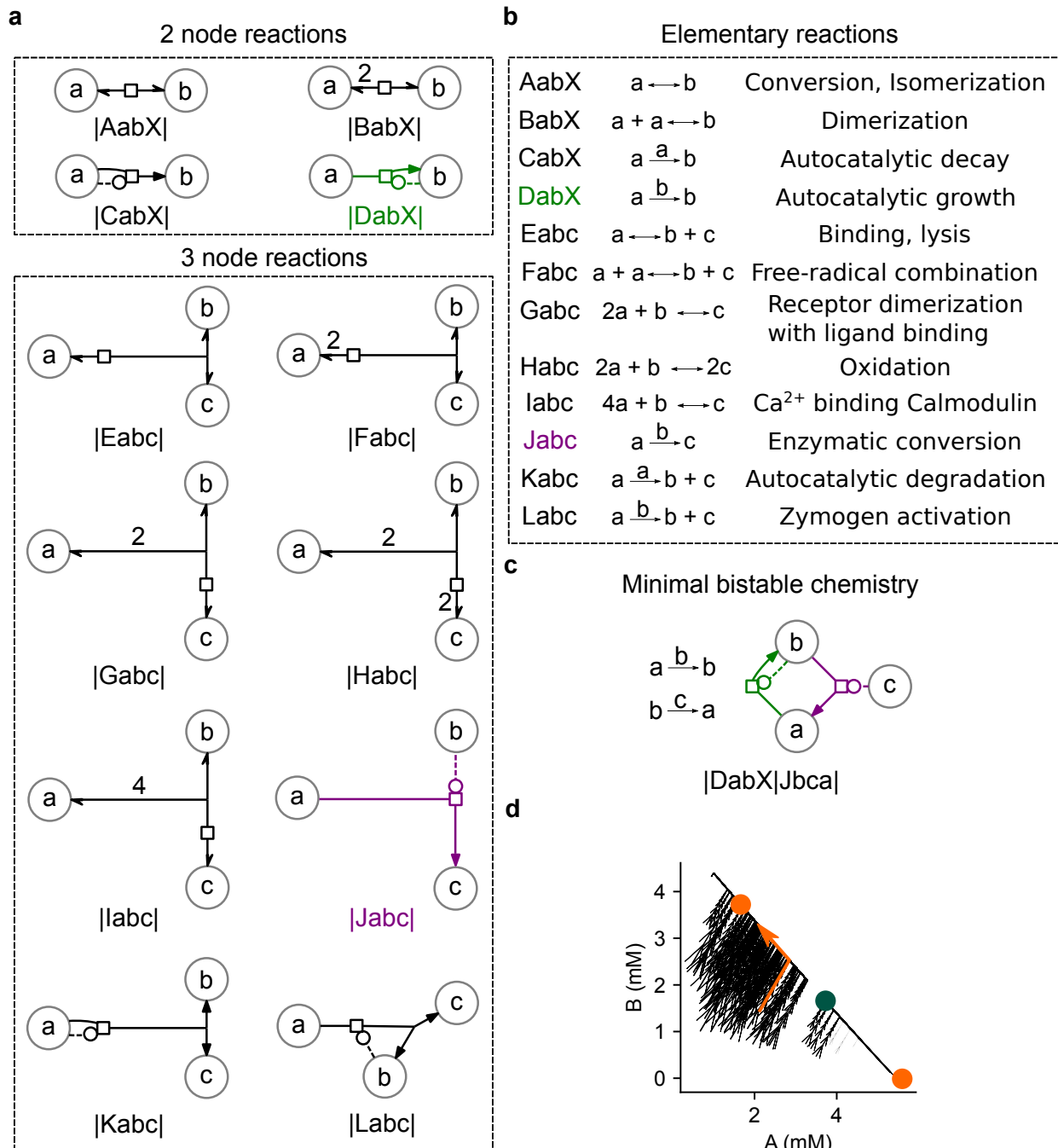


Figure 2.1: **a)** Chemical reactions used in this framework. Circles are reactants and arrows represent reactions. Reaction signature (below) in CSPACE format. Each reaction is flanked by 'l'. The capitalized first letter denotes 1/12 reaction types (A, B,... L). The next 2 or 3 letters are the reactant labels for reactions with 2 (top box) and 3 molecules (bottom box). **b)** Reactions graphically depicted in **a** represented in the canonical form with the reaction signature (left) (Adapted from (Ramakrishnan and Bhalla, 2008)). **c)** The smallest bistable CRN colored by reaction types (**a,b**). **d)** Phase portrait of the bistable system in **c**, showing 2 stable fixed points in orange and a saddle point in green. Trajectories from several initial conditions in black with one highlighted in orange seen moving towards a fixed point and away from the saddle. For reaction DabX, $K_m = 0.25 \text{ mM}$, $k_{cat} = 6.97e-2 \text{ s}^{-1}$; for reaction Jbca, $K_m = 4.28 \text{ nM}$, $k_{cat} = 9.98e-03 \text{ s}^{-1}$.

Results

In the first section, we extracted known bistable CRNs from the SWITCHES database and analyze their network structure (Ramakrishnan and Bhalla, 2008). Using this, we group the CRNs by their smallest independently bistable subnetworks and also calculate their structural robustness. In the second section, we allocate reaction rates to the CRNs and calculate their parametric robustness. In the third, fourth and fifth sections we compare the structural and the parametric robustness for all CRNs. In the sixth section, we calculate state-vector robustness for all CRNs and compare it with parametric robustness. In the final section, we calculate the noise robustness and compare it to the other forms of robustness.

Bistable CRNs have a higher proportion of a small set of reaction types

Structural Robustness for a reaction system can be defined as the resistance to change in the dynamical property of bistability with changes in the structure of the reaction system, i.e., insertion, removal or mutation of reactions. Below, we look at network structure of 3561 bistable CRNs extracted from the SWITCHES database, and their structural robustness. These CRNs were constructed by using reactions shown in Fig 2.1**a,b**. The smallest bistable CRN in the SWITCHES database is shown in Fig 2.1**c**. In Fig 2.1**d** we show the phase portrait of this CRN, demonstrating several initial conditions leading to one of two stable fixed points (orange) and the saddle fixed point between the two stable fixed points (green).

We extracted and counted all possible subnetworks of all 3561 bistable CRNs (**Subnetwork counting, Methods**). We then calculated the structural robustness as the fraction of these subnetworks that were bistable (**Structural robustness, Methods**).

First, we wanted to look at the distribution of individual reaction types in bistable systems. We counted the individual reaction types in each CRN and divided it by the total number of bistable

topologies. We observed that a subset of reactions was over-represented in bistable systems. For example, almost all bistable topologies had a 'D' type reaction. This was not surprising, given that it is a positive autocatalysis reaction, regularly found in bistable systems. We found that the set consisting of **A**, **C**, **D**, **F** and **J** reactions had a much higher frequency than other reactions (Fig 2.2a). Similarly, the pair **D**, **J** was the most common motif within the SWITCHES database (Fig 2.2b). These are also the constituent reactions of the smallest bistable in Fig 2.1c. The distribution of the structural robustness of all topologies is shown in Fig 2.2c. The orientation of the reactions with respect to each other is important to determine the dynamical behavior. A few examples of bistable and non-bistable topologies are displayed to show different bistable and non-bistable reaction sets (Supp. Fig 2.11). The structurally most robust topology is shown in Fig 2.2d which could be broken into 59 unique CRNs, out of which 26 were bistable. Structurally robust topologies were not preferentially enriched for any specific reaction type. We compared the structural robustness for all CRNs as a function of the frequency of each reaction within the CRN and found no clear correlations between the two (Supp. Fig 2.7).

Structurally robust systems contain many independently bistable subnetworks

(Ramakrishnan and Bhalla, 2008) had shown that bistable dynamics run in CRN "families", i.e., many bistable CRNs formed a highly interconnected set in a graph containing all configurations as nodes and addition and subtraction of reactions as edges. Thus, structurally robust topologies must have many edges in this graph, down to the smallest member of their family. There were only 80/3561 (~2.2%) CRNs which could not be further broken down into smaller bistable CRNs (. For 56/80 of these minimal bistable CRNs, we did not find larger CRNs that contained them. This means that either these CRNs were at the limit of the maximum network size we constructed, or that they did not retain bistability upon addition (or deletion) of reactions to them. Consequently, the rest of the 3481 topologies originated from just 24 root topologies (Table 2.1, Supp. Fig 2.8).

We called the grouping of all CRNs by these minimal bistable subnetworks “root groups”, and sorted them by the decreasing size of their family, i.e., number of CRNs the root CRNs were subsets of (Methods, Fig 2.2e,f). These form the core feedback network, on top of which other reactions that retain bistability can be added. Group I, the most common root CRN is also the smallest bistable topology (Fig 2.1c) and was a subset of about 47% of bistable CRNs. Note that a single CRN can be a member of more than one root group. Similarly, many root CRNs could compose a larger CRN.

First, we asked, are there some CRN families which have high structural robustness? We found that members of root groups V and VI had the highest median structural robustness (Supp. Fig 2.9). This implies that these root group CRNs are more conducive to growth by attachment of new reactions. Second, since CRNs could be members of many such families, we asked, do structurally robust topologies connect many families? On average, we found that the larger the number of root CRNs composing a larger CRN, the higher was its structural robustness. The structurally most robust CRN (Fig 2.2d) was the only topology that contained 8 out of the 24 root CRNs. In summary, only 24 root groups (containing unique minimal bistable CRNs) were present in 3481 out of 3561 CRNs, members of root groups V and VI showed high structural robustness, and a higher number of root groups implied higher structural robustness for a CRN.

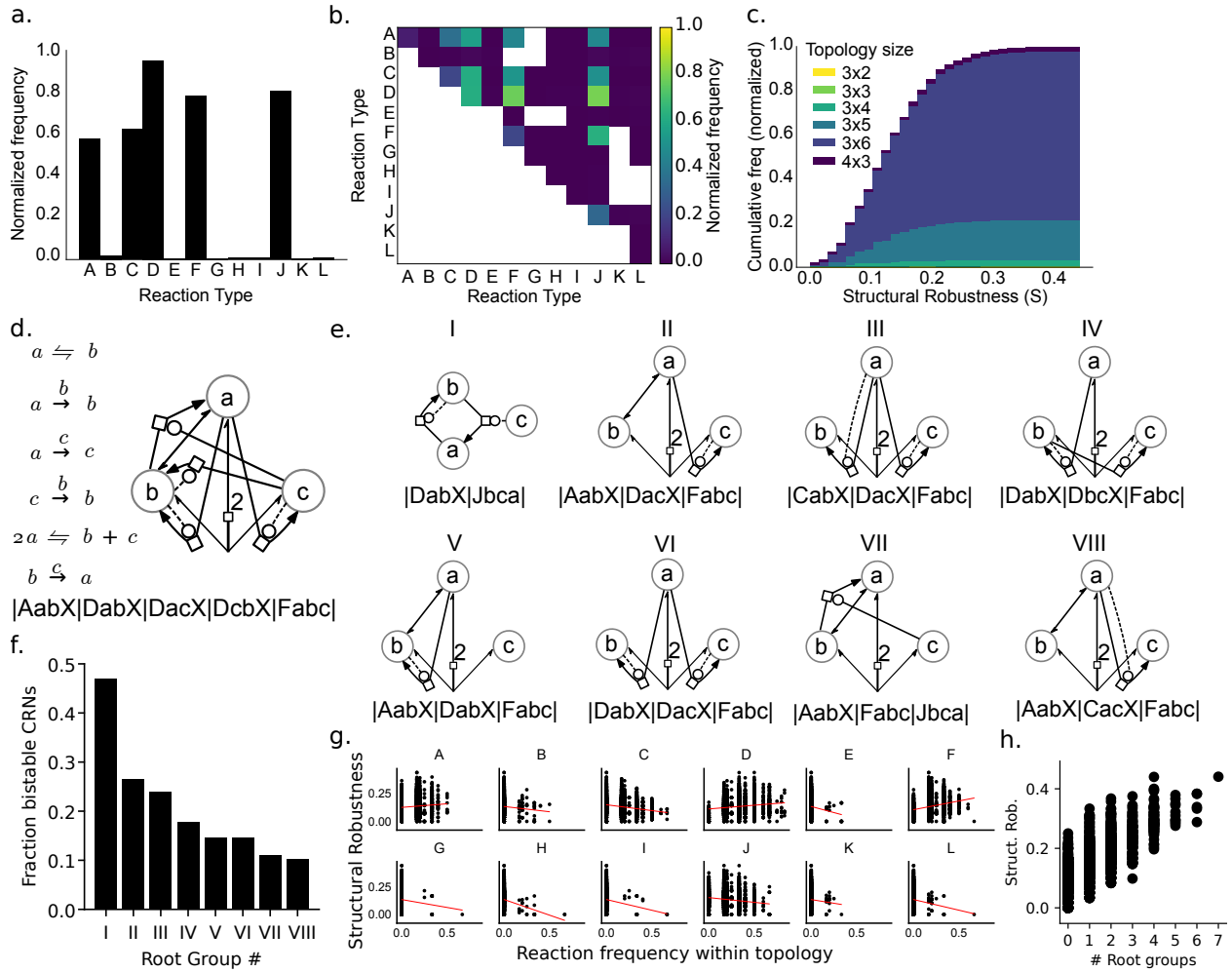


Figure 2.2: **a.** Distribution of individual reaction types in bistable systems. A subset of reactions enriches the space of bistables. **b.** Distribution of pairs of reactions in bistable systems (upper triangle only). White squares denote missing pairs. Lighter colors represent higher frequency. The pair “DJ” is over-represented in the space of bistables, which is also the smallest bistable topology (Fig 2.1c). **c.** Distribution of structural robustness across different reaction topologies. Different colors represent different dimensions of the chemical topology: In the description, the first number indicates the number of chemical species and the second number of reactions, e.g. 3x6 indicates three different chemical species and 6 reactions between them. **d.** Most structurally robust topology in the database. **e.** Root CRNs for 8 out of 24 root groups. **f.** A bar chart showing the fraction of total bistable CRNs that contain root CRNs as subsets. 8 out of 24 total root CRNs (as in e.) are shown here, the remaining 16 root CRNs were a subset of <5% of the total CRNs. **g.** Increase in the number of root CRNs as subnetworks (x-axis) on average meant an increase in structural robustness (y-axis). Our highest structural robustness topology was also the only topology that was a member of 8 root groups.

Small bistable CRNs have generally high parametric robustness

Parametric robustness is defined as the extent of resilience in retaining bistability with changes in the chemical reaction rates of the system (Bhalla and Iyengar, 2001). We assigned 2000 randomly-sampled biologically relevant sets of rates across 6 orders of magnitude to each of the 3561 CRNs, using Latin-hypercube method for high-dimensional uniform sampling (Deutsch and Deutsch, 2012; Moza, 2019). Each CRN with an associated set of reaction rates was called a *model*. Bistability was then assessed for each model by starting from several initial conditions and finding steady states using the steady-state finder in MOOSE. In this method the dynamical system is simulated in time, constrained by stoichiometry. Then local linear stability is checked by calculating the eigenvalues of the Jacobian around the state. When the real part of the eigenvalues is found to be negative, it is marked as a stable fixed point. With two stable equilibrium points, a chemical kinetic model was called bistable (Methods, 2.4). We found that 531313 out of the total 7.122 million models (7.46%) were bistable, which is a rather large fraction considering the very high dimensional parameter space (4-12 dimensions) from which we sampled. To obtain such a high average parametric robustness, bistability would have to persist over roughly 4.5 log-10 units of the 6 log units we sampled for each parameter.

Note that this definition of parametric robustness only requires flexibility of the reaction rates while retaining bistability. It doesn't take into account the bistable thresholds, i.e., the saddle fixed points that the system must cross in order to switch states, which can be another measure of the robustness of a bistable system. We checked how much the saddle points move in state-space by taking the pairwise distances between all saddle fixed points for all models belonging to a CRN and calculating the root mean square distance. We found that the larger the parametric robustness of the CRN, the more dispersed saddle points were in the state space (Fig 2.10). This correlation can arise because the higher parametric robustness models span a larger volume of reaction-rate parameter space, and hence the fixed points would also move correspondingly in the state-space.

CRNs in root group VI have high parametric robustness

We compared parametric robustness across the 8 largest root groups from Fig 2.1 and saw that root group VI had the highest median parametric robustness (0.77), followed by group III (0.74) and group IV (0.71) (Fig 2.3a). While there were 2 other root groups with higher median parametric robustness, they had much fewer members, and have been ignored in this study. Note that the root CRNs of group III and IV share some similarity in structure to the root CRN of group VI and differ from it in only one reaction (Fig 2.3b). Further, a large fraction (44.5%) of the distribution for members of root group VI was in the very high parametrically robustness (>0.8) range. This was followed by root groups III (32.9%), I (25.2%) and IV (22.2%). Indeed, even the CRN with highest of all parametric robustness (1.0) (Fig 2.3b, left) was the root CRN of group VI (Fig 2.2f). This CRN had a mirror-symmetric network topology and was found to be bistable for all parameters tested. In summary, membership of certain root groups, particularly group VI, pulled CRNs to high parametric robustness.

Weak correlation between structural and parametric robustness

Biological networks may have evolved network structures with different robustness attributes, in response to the sets of selection pressures depending on the stresses available to them. We wanted to ask if topologies that are robust to structural perturbations also show robustness to parametric perturbations. In Fig 2.3c, we show the distribution of parametric robustness for all CRNs combined. Some of these showed parametric robustness of 0 which indicated that the parameter space in which the CRNs are bistable were small, and could not be found by our random search method. In Figure 2.3d, we compare the structural and parametric robustness of all bistable CRNs. We found that for all CRNs combined, the structural and parametric robustness had a weak average correlation with each other (Slope of best fit = 0.43, $R^2 = 0.12$).

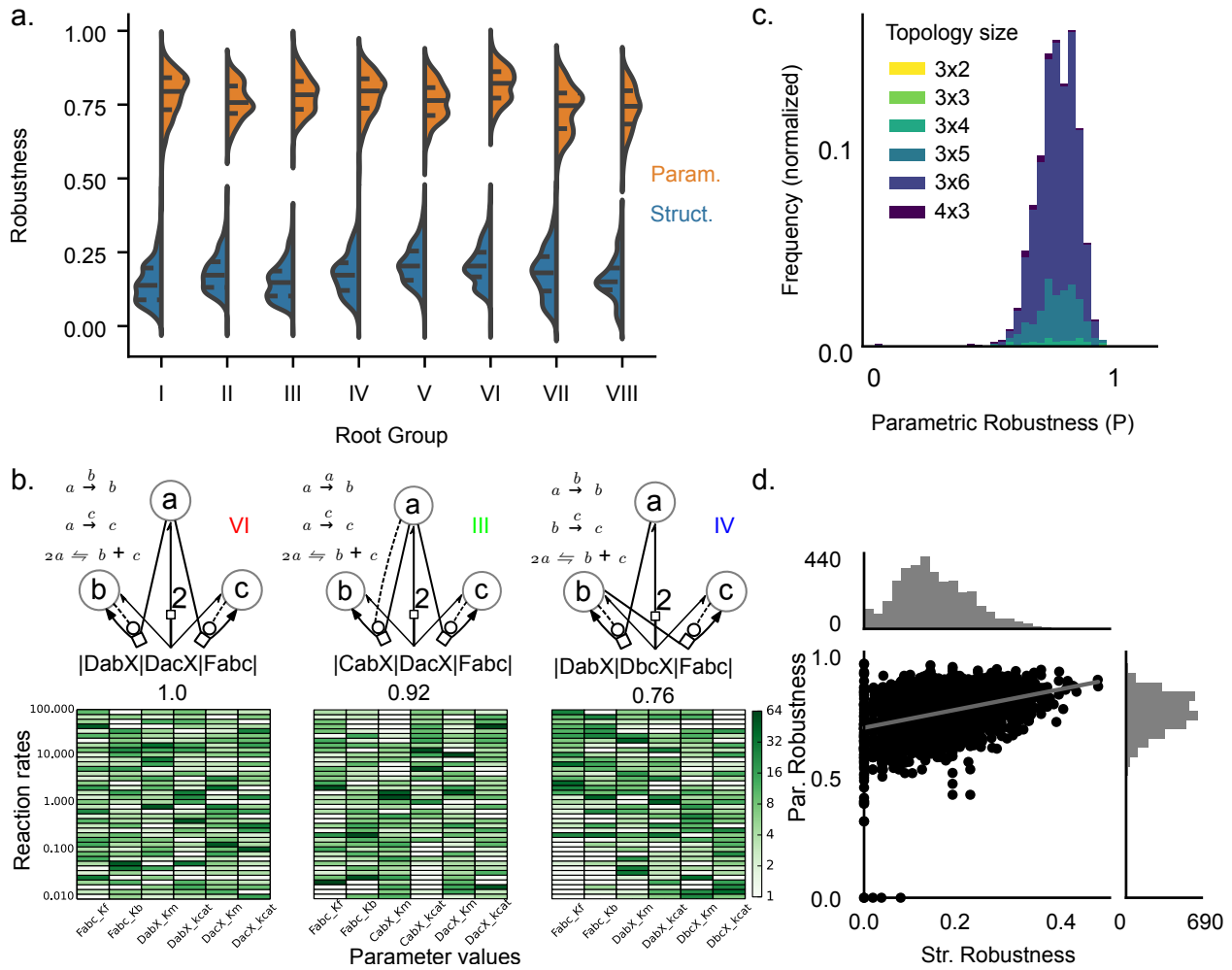


Figure 2.3: **a.** Distributions of structural (blue) and parametric robustness (orange) for CRNs grouped by their root topology from Fig 2.2e. Black lines inside the violin-plots mark the quartiles. Gray vertical lines indicate the median of the distribution. **b.** (Top) Root CRNs of the three root groups (VI, III and IV) with highest median parametric robustness in a. Each subpanel shows the chemical reactions, root CRN diagram, group number, reaction signature and the parametric robustness for the CRN below. (Bottom) Heatmaps representing showing the spread of bistable sets of parameters found for the randomly assigned reaction-rates across 4 orders of magnitude for the corresponding root CRN above. Darker colors indicate that a higher number of bistables were found in the region. **c.** Distribution of parametric robustness colored according to the number of reactions in the network. **d.** The relationship between structural and parametric robustness for all CRNs with histograms in gray. All the root CRNs lay at 0 structural robustness. There is a weak average correlation between the two (Slope of best fit = 0.43, $R^2 = 0.12$).

CRNs with similar root groups have similar parametric robustness

We then looked at the relationship between structural and parametric robustness by grouping the data with respect to the root groups which showed high parametric robustness (Fig 2.3b, 2.4a,b). We made three key observations here. First, we observed that the CRNs which were members of the same two (or more) root groups had similar parametric robustness to each other, as well as to the multiple roots groups they belonged to (Fig 2.4a,b). In Fig 2.4a,b we can see the three root groups (VI, III and IV) and their pairwise combinations (bottom). Second, almost all of the very high structural and high parametric robustness combination CRNs were members of root group VI (Fig 2.4 a,b). This is most clearly seen in Fig 2.4b, where all three groups are overlaid. Third, by virtue of membership of two (or more) root groups the structural robustness of the CRN also increased (Fig 2.4b). The combination colors that represent a membership of multiple groups show up at high structural robustness. Thus, CRNs which were members of group VI root, in addition to other root groups were more likely to be both structurally and parametrically robust CRNs.

Highly parametrically robust systems have a mirror-symmetric architecture

On investigating the high parametric robustness CRNs further, we found that very high parametrically robust topologies had not only group VI but also other similar looking architectures. We found that out of the top 1% (35/3561) parametrically robust bistable topologies, 91.4% (32/35) had either $|DabX|DacX|Fabc|$ or $|DabX|DacX|Jbca|Jcba|$ (or both) as their subnetwork. Note the mirror symmetry in these CRNs. For the top 10% (356/3561) parametrically robust bistable CRNs, they were present in about 47% (167/356) CRNs. However, if we considered their frequency in all CRNs, they showed up only 16.3% (580/3561) of the times. Thus, having a pair of mutually-competitive autocatalytic feedback-loops was the best strategy for very high robustness to parameter fluctuations, showing bistability for almost all parameters tested. These CRNs show a “symmetric winner-takes-all” strategy, i.e., if we observe Fig 2.4d (left), molecules b and c com-

pete with each other by auto-catalyzing their own formation. If there is a slight excess of one over the other, the CRN is driven to a state with all molecules of one type and none of the other. The top 3 highest parametrically robust topologies after the group VI root CRN are shown in Fig 2.4d, where the mirror-symmetric core of the network across the molecule a can be observed.

The root CRN of the second-highest parametric robustness (root group III) was $|CabX|DacX|Fabc|$, which also shows a winner-take-all strategy. However, in this case, reactant a autocatalyzes its own degradation to b , while competing with c which is autocatalyzing its formation. Root group III was present in 54% of the top 1% parametrically robust CRNs, and 38% CRNs for the top 10%. For all CRNs combined, it was present in 24% of the networks.

Does the existence of symmetry universally imply high parametric robustness? We found that this was not the case. By permuting node labels, we looked at all possible models which had a *global symmetry*, i.e., when permuting node labels preserved the relationships between the nodes (Methods). There were a total of 36 such topologies. Unsurprisingly, we did not find the converse relation: CRNs with global symmetry were not necessarily associated with high parametrically robustness (2 sample KS-test, pvalue=0.034).

Then we asked, do the higher parametrically robust topologies preferentially contain some of these symmetric topologies as a subnetwork? To answer this, we had to look at *local symmetries* within the network topology. We created all possible subgraphs of networks and listed the set of all subgraphs that had globally symmetric topologies. For topologies which contained such subgraphs, we asked: how many reactions are there added on top of these core symmetric motifs? Using this approach, we were able to group all topologies by the number of excess reactions, called the “order” of the topology. We found that the distributions of topologies that contained locally symmetric motifs were preferentially higher in parametric robustness than a random sample from the distribution (Fig. 2.4b, 2-sample KS-test, p-value = 5e-07, 4e-10, 1e-50, 8e-56 for orders 1-4).

In summary, symmetric mutually-competitive autocatalytic reaction networks were the best strategy attained by multiple CRNs with different structures for optimizing parametric robustness of CRNs.

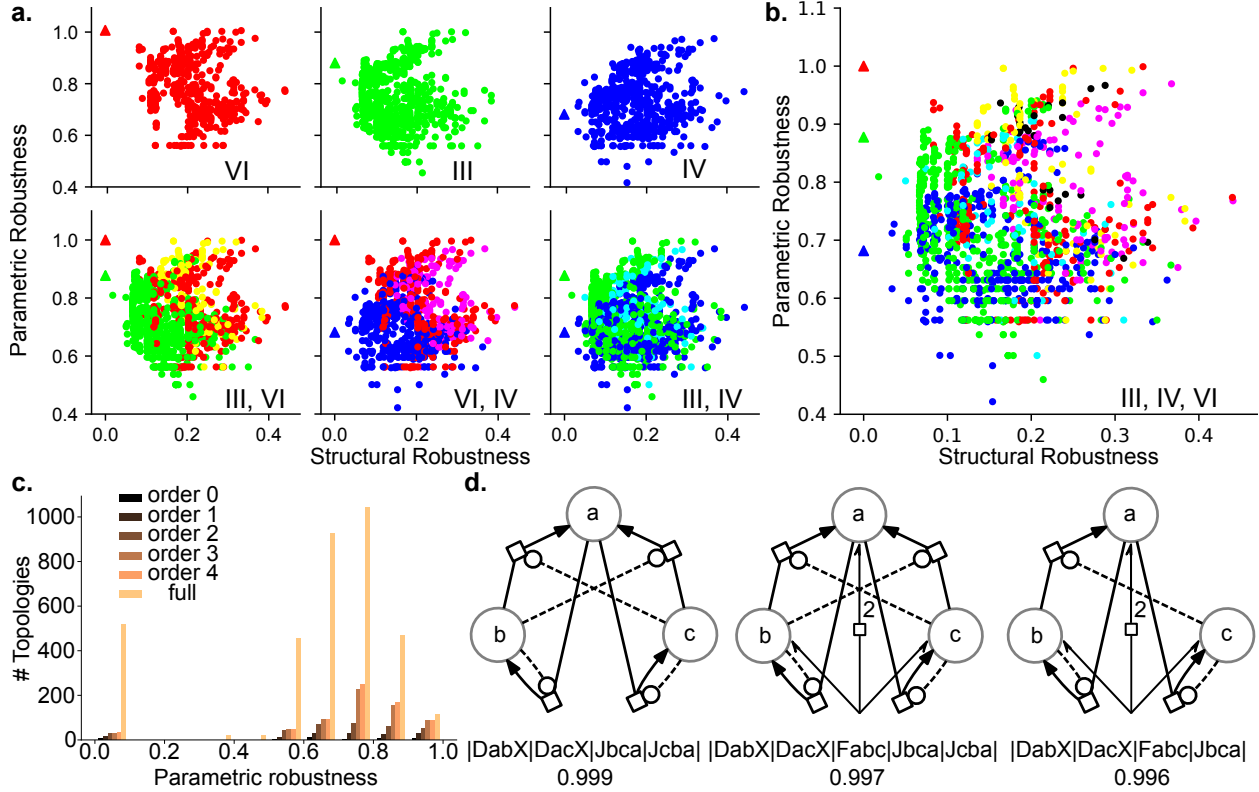


Figure 2.4: **a.** (Top) Relationship between the structural robustness and parametric robustness for CRNs from three CRN root groups (VI, III and IV) colored in ‘r’, ‘g’ and ‘b’. (Bottom) A pairwise overlay of the three plots above, with CRNs that belonged to both groups colored with the combination of the corresponding colors, i.e., yellow indicates ‘r’ and ‘g’, magenta indicates ‘r’ and ‘b’, cyan indicates ‘b’ and ‘g’. Colored triangles indicate the root CRN for the group. **b.** All three groups in a. plotted together. When a CRN belonged to all three root groups ((‘r’, ‘g’, ‘b’) = (1,1,1)), we colored the dots black instead of white for visualization. **c.** Parametric Robustness of topologies on the basis of local symmetries. ‘Order’ implies the number of additional reactions on top of the symmetric motif. ‘Full’ is the corresponding bin of the complete distribution of Parametric robustness for all CRNs. **d.** The second to fourth highest parametrically robust topologies from left to right, with reaction signature and parametric robustness below. Note the mirror symmetry across the molecule *a*. The right-most CRN will have an order 1.

Several CRNs with high parametric robustness have low state-vector robustness

CRNs are employed in signalling cascades for communicating information to perform various computations. In this sense, bistable systems carry binary codes within their steady-state concentrations. To robustly ascertain the state at a decision point, multiple entities from the chemistry may be measured simultaneously by the downstream reaction system. This can reduce absolute intrinsic noise and differences across compartment volumes. However, bistable signaling systems face the following challenge: the parameter space of reaction rates where the topology is bistable may be large, but the relative concentrations of individual reacting moieties between the two steady-states may change drastically as reaction-rates change. For example, consider the steady-state concentrations for each of 3 reacting moieties at the two stable fixed points of a bistable system (Fig 2.5a). If the concentration for a given moiety is larger for one of the fixed points, it is marked High (1) and the other state is correspondingly marked Low (0). Thus, the configuration of the two stable states in this example is 010 and its complement 001, where the molecule 'a' does not show a change between the two stable states (Fig 2.5a). However, a perturbation in reaction-rate parameters while retaining bistability, could add two more relative configurations, such as 011 and 101 (Fig 2.5b). We calculated the state-vector robustness as the sparsity of the number of such configurations (**Methods**). We show example configurations found on altering two rate parameters using root CRNs of root groups VI, III and IV (Fig 2.5c). The distribution for relative concentration robustness of all topologies is shown in **Fig 2.5d**. We noticed that there were several CRNs with only one bistable configuration. Then we compared the parametric and state-vector robustness for all CRNs (**Fig 2.5e**). We observed a slight negative correlation between state-vector and parametric robustness. This implied that there were several high parametrically robust topologies which had many alternate relative steady-state configurations. Curiously, the parametrically highest CRN (Fig 2.3b left) also had state-vector robustness = 1, which implies that there was a unique binary steady-state configuration for all parameters tested. In summary, we noticed that there may be

several high parameter robust CRNs with low state-vector robustness. This may pose a limitation on their roles as signalling molecules, as although parametric fluctuations retain bistability, the information-content in their concentrations may be lost.

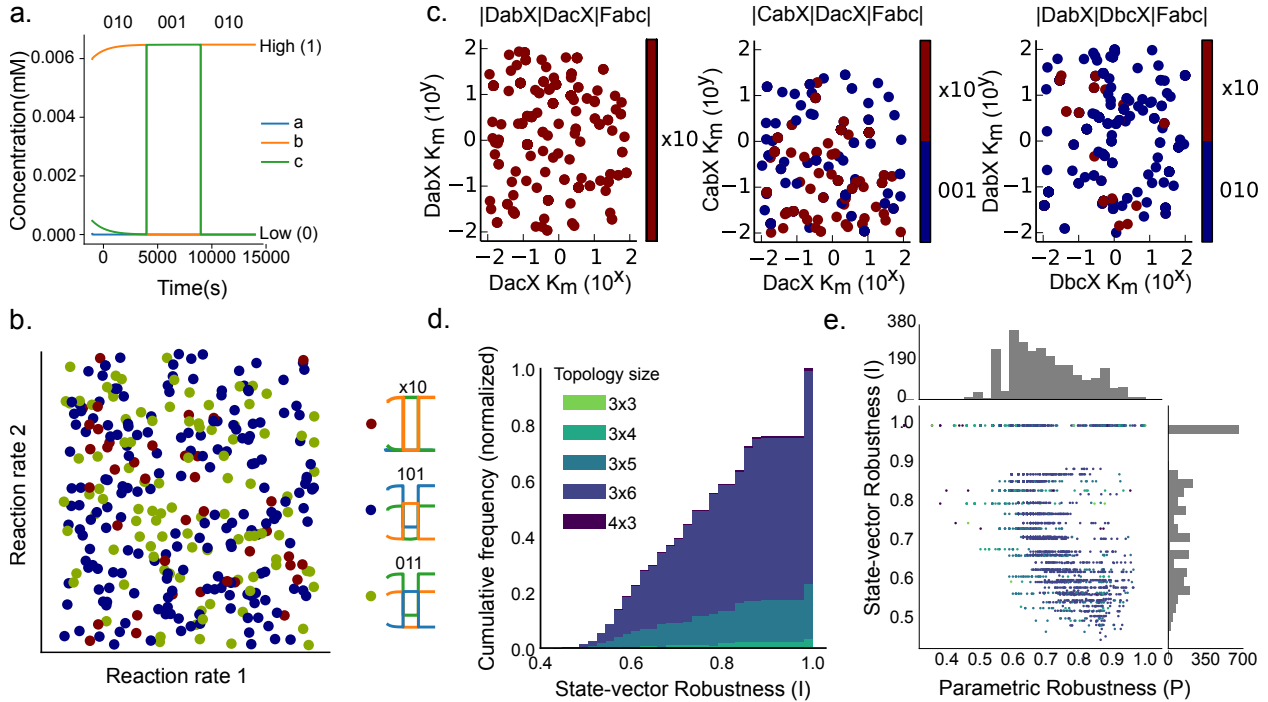


Figure 2.5: **a.** Deterministic simulation of the group VI root CRN in Fig. 2.3b (left), and the schema used for calculating State-vector Robustness. High concentrations (for a given reactant) were labelled as 1 and low as zero, and a binary vector was generated. At 5000 s, the molecules of b and c (and complexes) were swapped, so that the system switched to the second stable state, and at 10000s it was switched back, displaying its 2 different stable states. **b.** A schematic showing 3 different binary steady-state vectors at bistable fixed points as a function of variation of two different rates. Each point in the graph is a unique configuration of reactants a, b and c, shown in the legend (reactant colors in legend the same as in **a**). x in the binarized state-vector indicates that it did not change across the two stable states for this pair of bistable states. **c.** The different configurations of binary steady-state vectors for root group CRNs VI, III and IV (left to right) for variation of two different reaction-rate parameters. Both x and y-axes are \log_{10} -scale. Both group III and IV show two different configurations, while group VI shows only one configuration. **d.** Distribution of state-vector robustness (I) across all topologies. Several topologies showed state-vector robustness of 1., ie., they retained the relative order in the concentration of molecules at their steady states when swept through parameter space. **e.** The relation between parametric and state-vector robustness for all CRNs has a slight inverse relationship.

Noise Robustness

CRNs are often compartmentalized in biological systems, such as dendritic spines in small volumes, with a relatively small (order of 10) number of molecules of a given type (copy number). Small copy numbers can lead to fluctuations also called intrinsic noise at steady-state concentrations. For bistable systems, this can lead to spontaneous state transitions between the two stable fixed points, which implies a loss of memory, imprecise decisions, and general loss-of-function (Bhalla, 2004c,a,b). We calculated the ability of CRNs to be resistant to intrinsic noise by measuring the time they spend in a stable state before they spontaneously transition, also called *residence time*. In Fig. 2.6**b-e** we show the stochastic time-series evolution of a model in Fig 2.6**a**, over 4 different volumes sampled logarithmically. The concentration of molecule b (in orange) can be observed to stochastically relax to the two different fixed points. We ran the stochastic simulation for each parameter set that was found to be bistable for each CRN for a period of 86400s for 10 trials each. An example simulation can be seen in Fig. 2.6**f** where we start the model in Fig 2.6**a** at the same initial condition at volume 0.5 fL for 10 trials. The different residence times in the initial state can be seen before the system relaxes to the other stable state. From these simulations, we calculated a CRN's Noise Robustness (N) at a given volume, as the geometric mean of the average residence times in either direction, averaged over all the different parameter combinations for that CRN.

In Fig. 2.6**g**, we show the Noise robustness (N) distribution for all CRNs (n=519) that had positive Residence times at a volume of 0.5fL. The residence time distribution and hence the noise robustness increases with volume, as the probability that the intrinsic noise causes state transitions reduces. This also limited our ability to measure residence time distributions at larger volumes. The change in N across volumes for a subset of topologies for which N could be calculated over several volumes can be seen in Fig. 2.6**h**.

No average correlation of noise robustness with structural and parametric robustness

Lastly, we compared the noise robustness with structural and parametric robustness for the CRNs where we had all three measurements (Fig 2.6i). We found that structural and parametric robustness had no average correlation with noise robustness. In summary, we found no average correlation between the measured robustness to structural and parametric perturbations and robustness to intrinsic noise for CRNs.

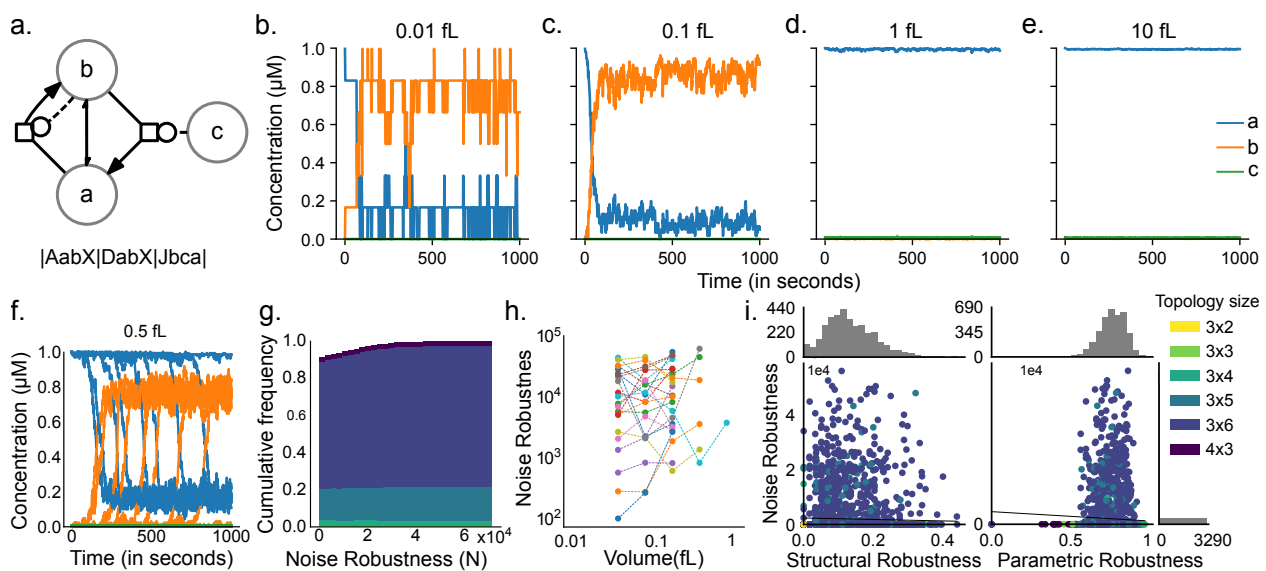


Figure 2.6: **a.** Representative CRN used to display stochastic simulations. **b-e.** Stochastic simulation of model in Fig 2.6a at 4 different volumes (0.01fL, 0.1fL, 1fL and 10fL from left to right) starting from the same initial concentrations and reaction rate parameters. Notice the decrease in noise and reduction in the transition probability between fixed points. **f.** 10 different trials of stochastic simulation of the model in Fig 2.6a at volume 0.5 fL. The residence time in each state varies across trials. **g.** Distribution of first passage times (residence time) across all CRNs where we could measure residence time at 0.5 fL. **h.** A subset of topologies from which we could calculate residence time on at least 4 different volumes. **i.** The relationship between Structural and Parametric robustness to Noise robustness. No average correlations were observed.

Discussion

We have compared different robustness properties of all bistable CRNs in the SWITCHES database with ≤ 6 reactions between ≤ 3 molecules and 3 reactions between 4 molecules. We

found that ~98% bistable CRNs had bistable subsets from one of 24 minimal bistable CRNs (or root CRNs). Further, we found that simple mirror-symmetric CRNs had very high parametric robustness. On average, we found that different forms of robustness had very little average correlation between them with the exception of parametric & state-vector robustness; and structural & parametric robustness) . However, we found that grouping them by their smallest bistable members (or root CRNs) revealed a simple organization, where CRNs with similar root groups clustered together. It also revealed that the presence of a mirror-symmetric competing-autocatalytic network (group VI) to a CRN correlated with both a high structural and high parametric robustness. Further, the presence of multiple root CRNs meant higher structural robustness. It is important to note that this doesn't mean a higher propensity of the existence of bistable systems if they are composed using these 24 root groups. However, if a CRN composed using many root groups turns out to be bistable, it is likely to be robust to structural perturbations. Importantly, we observed a lack of average pairwise correlation between noise and structural and noise and parametric robustness. This implies, for example, that a CRN optimized for being robust to parametric variations might not be able to retain steady-state concentrations in the face of intrinsic noise if compartmentalized in a small volume. However, by grouping the CRNs based on their root groups, we observed that certain root groups had a higher propensity for structural and parametric robustness.

Some bistable families are conducive to evolvability

(Ramakrishnan and Bhalla, 2008) suggested a *relatedness* of bistable CRNs to each other, and that evolution could stumble upon bistable network structures with relative ease, the smallest with just 2 chemical reactions between 3 reactants. This relatedness is relevant for both the emergence of complexity and *evolvability* in complex CRNs. The addition of certain reactions to a CRN can lead to additional control mechanisms for the CRN or an increase in the complexity of the reaction system by adding newer dynamics while retaining the old ones. For instance, the system could become tri- or n-stable to have multiple steady-state concentrations. This may be relevant, for

example, in the case of dendritic spines with membrane receptor concentrations of ligand-gated ion channels. Structurally robust networks can enable such evolvability as they can retain the dynamics of the smaller network in pockets of parameter space while acquiring newer dynamics.

On average, we observed that there was a weak correlation between structural and parametric robustness. Thus, the constraints faced by a growing CRN may also partly alleviate some rigidity in parameter space. However, classifying the CRNs by their minimal members (root CRNs) reveals the fact that the members of root group VI show both high structural and exceptional parametric robustness. To our knowledge, this is the first study to systematically shows that competitive-autocatalytic feedback-loops are the best strategy for structural and parametric robustness in small CRNs. This naturally leads us to an alternative interesting interpretation in the context of network growth. Regardless of the mechanism of network growth over evolution, if the pre-existing network is retained, it will contain one or more minimal subnetworks with appropriate dynamics for its function. Now, the propensity of the addition of new edges or new nodes to the network would depend on how conducive the previous network is to such addition, without disastrous effects on its existing function. Thus, the existence of group VI CRNs functions as facilitators of network expansion for bistable networks.

A general strategy for parametric robustness

An interesting feature of root group VI CRN is its mirror-symmetric mechanism. These structurally symmetric competitive feedback-loops allow the CRN to expand slight asymmetries in rates of reactions or concentrations on the two symmetric sides of the network into all-or-none steady-states. Here, one of the two competing autocatalysts converts all the substrate and the other enzyme to itself. Certain mirror-symmetric structures have been reported earlier in different systems and have been termed *reciprocal regulation*. Here, a molecule can catalyze its formation, as well as inhibit its inhibitor to lead to double-positive feedback and hence ultrasensitivity. For example

CDK1–Cdc25–Wee1 system for mitotic cell-cycle transitions (Ferrell, 2008). Our mechanism is greedy, implying a high sensitivity to concentration and rate asymmetry in the competing feedback loops. This implies that starting from the saddle, the bistable system quickly reaches the steady-state magnifying any asymmetry in reaction rates or concentrations.

This strategy of competing autocatalytic loops is also relevant for enantioselective synthesis in biological systems. Bistable systems have been proposed for a long time as chemical means of abiogenic selection of L-type or D-type enantiomers observed in biological systems. Parametrically robust enantioselective mechanisms can sustain and allow for the creation of a variety of different biomolecules by being resilient to substrate and enzyme alterations without losing the bistable mechanism. Curiously, the group VI root CRN (Fig 2.4b) was proposed by (Frank, 1953) for the synthesis of pure enantiomeric (only L or only D-forms) from an achiral substrate and later experimentally validated by the Soai reaction (Shibata et al., 1996). This mechanism can be understood by considering *a* as the achiral precursor of the pure enantiomeric forms (*b* and *c*) of the product, which catalyze their own formation (Fig. 2.4b). In this CRN, *b* and *c* react together to give back 2 molecules of *a*. Note that this reaction network suggested for the generation of homochirality shows up as the top parametrically robust reaction system. This is an important consideration for this mechanism, as this CRN is robust to the addition of new reactions, and members of the group VI are bistable for a large volume of parameter space. Thus, once the enantiomers have been synthesised asymmetrically, it is conducive to the addition of reaction to increase the enantiomeric asymmetry without losing its bistable dynamics. (Viedma, 2005) proposed an alternative model with cross-catalysis to generate back *a*, which surprisingly, shows up as our second highest parametrically robust topology shown in Fig. 2.4c (first from the left). It is worth noting that this CRN is a mirror-duplication of our smallest possible bistable CRN across the axis through *a* (Fig 2.1c).

In the case of signaling pathways, another important consideration needs to be made. As reaction networks change by either addition of new reactions or reacting molecules, or by changes in

reaction rates of the system, the steady-state concentrations of molecules can change drastically. This can make the robustness of otherwise parametrically robust CRNs not very useful if the concentrations of signaling molecules are meaningful and important for downstream networks. Due to the greedy nature of the mutually-competitive autocatalytic-feedback loops strategy, the group VI root CRN and similar CRNs maintained their relative binarized steady-state vectors.

Future directions

The next step would be to construct network growth models with increasing complexity while retaining older dynamics. It would be interesting to see similar root groups for other dynamical behaviours, such as oscillators, or chaotic systems, and also minimal chemical systems with multiple dynamical behavior under different parameter regimes. Our work has taken an exhaustive map of CRNs generated in (Ramakrishnan and Bhalla, 2008) and constructed a map of different kinds of perturbations available to a bistable system. This map has proved to be valuable for comparing alternate small CRN models for their robustness by revealing a neat grouping using minimal CRNs called root groups. We also propose that this map can be used as a tool for composing robust complex networks using root groups, and for designing simple switches with tunable properties in synthetic biology.

Methods

Bistable CRN selection

Bistable CRNs were extracted from Searchable Web Interface for Topological CHEmical Switches (SWITCHES, <http://switches.ncbs.res.in>), an online resource curated using the results of its parent publication (Ramakrishnan and Bhalla, 2008). SWITCHES contains ~7e5 chemical kinetic models of 2-5 reactants with 35967 bistable models in cspace and SBML formats along with their steady states. **3561** bistable CRNs were extracted from these bistable models. This is an

exhaustive list of all bistable CRNs possible with up to 3 reactants and 6 reactions or 4 reactants and 3 reactions.

Graph Generation

SBGN graphs (Novère et al., 2009) were generated for all CRNs using elementary chemical reactions depicted in Figure 2.1a. We used Python with the free graph visualization library Graphviz (Ellson et al., 2001) and implemented a Cspace CRN graphing library to generate SBGN graphs.

Simulations

All simulations were performed in the python with MOOSE (Ray et al., 2008). The steady-state finding routine uses a deterministic simulation of the coupled chemical reaction differential equations using the rk4 integration method. The stochastic simulation was also performed in MOOSE, which uses the Gillespie algorithm (Gillespie, 1977) to exactly simulate the chemical master equation to get the stationary distributions of state-space over time. Steady State Solving and Stochastic simulations were done on 1000 cores in an array job on a cluster computing framework using Sun Grid Engine (SGE), bash and Python.

Generating random models

Bistable CRNs selected from the SWITCHES database were populated with rates uniformly from across 6 orders of magnitude. Since the number of dimensions across which the random rates had to be sampled was typically large (between 4 and 12), an efficient sampling scheme was utilized to sample the rates efficiently. We implemented a uniform sampling method called Latin Hypercube Sampling with multi-dimensional uniformity (Moza, 2019; Deutsch and Deutsch, 2012). In this method, the parameter space is divided into strata by oversampling (5 times) using a uniform sampling method. Then these grids are sorted, and the pairwise distances are calculated

between all pairs of strata. This is followed by calculating the average distance of each stratum with its neighbouring stratum. Finally, the stratum with the minimum average distance from other strata is eliminated. This process is repeated until the required number of samples is reached. Real numbers between consecutive strata are then sampled uniformly using conventional Monte Carlo methods. This helps in maintaining reasonable uniformity of sampling in high dimensional space that is not achievable using simple Monte Carlo methods. This implementation is publicly available at <https://github.com/sahilm89/lhsmdu>. More details about the algorithm can be found in (Deutsch and Deutsch, 2012). In this way, we sampled 2000 sets of random rates, with two rates for each reaction in the CRN. For reversible reactions, this was forward (k_1) and backward (k_{-1}) rates. For enzymatic reactions, although we sampled K_m and k_{cat} from the Michaelis Menten formalism, they were internally converted in MOOSE into mass-action formalism, with $4k_{-1} = k_2 = 4k_{cat}$ and $K_m = \frac{k_{-1}+k_2}{k_1}$.

Finding steady states

We used the steady-state solver in MOOSE to find steady-states for these models, which uses time-course analysis in conjunction with linearization around the fixed point to find and assess the dynamical behavior of steady-states. We systematically swept across the initial condition space by random, stoichiometrically-constrained jumps and found steady states. Then the algorithm analyzed the stability of the fixed points found based on the signs of the eigenvalues of the Jacobian matrix. While this process does not guarantee that all possible fixed points will be found, it is faster than other algorithms (Ramakrishnan and Bhalla, 2008). We started from 1000 different initial conditions to get a list of steady states for each model. This process was repeated for all 2000 random rates for the topology.

Classifying bistables

We clustered the steady states obtained from above into one or points to classify a model as bistable if there were exactly two clusters found. We used the following element-wise distance measure for this classification:

$$D_i = \frac{|a_i - a'_i|}{a_i + a'_i + \theta} \quad (2.1)$$

a_i is the concentration of the entity at the i^{th} index in the steady-state vector being tested for similarity against a'_i , the corresponding concentration in the running-average solution vector(s), θ is the offset = 1e-3, and where D_i is the element-wise distance of the i^{th} entity. The offset θ avoids divisions by zero. If *all* the elements of the solution vector fall under 5% tolerance, the vectors are considered identical. If this process yields two sets of solutions at the end, the model is called bistable.

Subnetwork counting

To count the subnetworks, we first took the reaction signatures for the CRN and created all possible combinations of the reactions, keeping the relative connections between reactants constant. For example, the CRN from Fig 2.2b, $|DabX|DacX|Fabc|$ would have the following combinatorial subnetworks: $\{|DabX|, |DacX|, |Fabc|, |DabX|DacX|, |DabX|Fabc|, |DacX|Fabc|\}$. Also, for some reversible reactions, certain node labels can be permuted without loss of relative relations between reactants. For example, reactants a and b can be permuted in signature $|AabX|$ to give $|AbaX|$ without changing the meaning of the reaction. This is also true for permutations of molecules b and c in reactions $|Eabc|$, $|Fabc|$ and $|Kabc|$. We performed these permutations at the second step to generate the set of all subnetworks. Lastly, the node labels were globally permuted, i.e., all possible permutations of the reactant label set $\{a, b, c, d\}$ were done to generate the final

subnetwork set for each CRN. Then, for each topology, we compared these subnetworks against bistable CRNs and counted the exact matches.

Structural Robustness

We quantified Structural Robustness (S) as the number of subnetworks of the CRN that were bistable normalized to the total number of subnetworks.

$$S = \frac{b}{t} \quad (2.2)$$

where b is the total number of subnetworks that are bistable, and t is the total number of subnetworks in the topology. We utilized the string-based string-based (Cspace) format of the CRN for counting subnetworks, as explained above.

Symmetry analysis

The node label permutations mentioned above were also used for symmetry analysis. We measured the subnetworks for a given CRN that were independent, but identical to each other. If these subnetworks were sufficient to construct the entire CRN, the CRN was called globally symmetric. 36 such CRNs were found. If other reactions besides the identical independent subnetworks were required to constitute the CRN, the network was called locally symmetric, and the number of reactions that needed to be added were called the order of the CRN. Yet other CRNs had no symmetry at all.

Parametric Robustness

Parametric Robustness, P was quantified as the fraction of the n-dimensional volume of the bistable parameter space. It was calculated as the fraction of the total number of random parameter

models for a given topology that were bistable normalized by raising to the power of 1/number of parameters.

$$P = \sqrt[D]{\frac{b}{T}} \quad (2.3)$$

where b = Number of bistable parameter sets, T = Total number parameter sets, and D = Number of parameters in CRN.

State-vector Robustness

We listed all distinct steady-state vectors from the stable solutions found for each CRN. We then calculated the element-wise difference between the two stable states α_1 and α_2 . If the concentration difference between the two followed equation (4), the concentrations were considered identical. If not, we applied the Heaviside function, H elementwise (\odot) to the difference to get an ordered binary vector \vec{b} (equation 5).

$$|\alpha_1 - \alpha_2| \leq tol_{abs} + tol_{rel} \times max(\alpha_1, \alpha_2) \quad (2.4)$$

with $tol_{\{abs\}}=1e-9$ and $tol_{\{rel\}}=1e-6$.

$$\vec{b} = H \odot (\vec{\alpha}_1 - \vec{\alpha}_2) \quad (2.5)$$

where the Heaviside function is defined as:

$$H(x) = \begin{cases} 0 & n < 0 \\ 1 & n \geq 0 \end{cases}$$

Then we listed the set of all binary vectors $B = \{b^i\}$ with cardinality $L = |B|$. State-vector Robustness (I) was quantified as the number of distinct binary vectors that exist in the space of all possible steady states for the CRNs.

$$I = 1 - \frac{\log_2 L}{d} \quad (2.6)$$

where I = State-vector robustness, and L = Total number of distinct binary vectors in the steady states of a CRN, d = dimension of \vec{b} .

Noise Robustness

Noise robustness for a bistable model at a given volume is quantified as the geometric mean of the average time spent in the basins of the two stable fixed points before the system switches to the other fixed point due to statistical fluctuations. The time spent before the transition in each state is called the Residence Time (RT) (Curtin et al., 2004), or Kramers' time (Kramers, 1940). For a CRN, the Noise robustness was averaged over all parametrized models.

$$N = \sum_{B=1}^{num_B} \sqrt{\overline{RT}_{forward} \times \overline{RT}_{backward}} \quad (2.7)$$

where, B = Across all bistable models

num_B = Number of bistable models

RT = Residence Time

Forward and Backward Kramers' times $\overline{RT}_{forward}$ and $\overline{RT}_{backward}$ for a given volume were calculated by starting off a stochastic simulation using Gillespie's exact stochastic simulation algorithm (Gillespie, 1977) and measuring before a state transition. We started off all simulations from a saddle point to measure the relaxation times to the stable states for other calculations, which can then be used to normalize the residence times. We measured transitions using a cutoff on the continuously calculated element-wise distance between the measured stochastic state vector, and two deterministic fixed points using Equation 1 with $\theta = 1e-1$. This was then repeated for various volumes from $1e-21 m^3$ to $1.024 e-18 m^3$ in 10 logarithmic steps of base 2, with a simulation time of 1 day (86400 seconds), or until a spontaneous transition happened. The whole run was repeated 50 times.

Removing stuck states

In some CRNs with irreversible reactions, all gradients and all but one concentration can become zero, called a “stuck” state. Once the system achieves this state, it is not possible to escape from it with intrinsic fluctuations, because all transition probabilities are zero which leads to a no-noise state. Thus, before running stochastic simulations, the continuous fixed point vectors (in concentrations units) were converted into discrete molecule counts at $100 fL$. If there were models whose steady states had less than 2 non-zero elements in their state vector, they were labelled “stuck” and were omitted from stochastic simulation and further analysis.

Table 2.1: Root groups

Label	Root
I	DabX Jbca
II	AabX DacX Fabc
III	CabX DacX Fabc
IV	DabX DcbX Fabc
V	AabX DabX Fabc
VI	DabX DacX Fabc
VII	AabX Fabc Jbca
VIII	AabX CacX Fabc
IX	AabX DacX DcbX Jbca
X	AabX DabX DacX DcbX
XI	AabX DacX Fbac Jbca
XII	AabX CabX DacX DcbX
XIII	AabX CacX DabX Jcba
XIV	AabX CacX Jbca Jcba
XV	AabX BacX Jbca
XVI	CabX DacX DcbX Fbac Jbca
XVII	CabX CbaX DacX DcbX Jbca
XVIII	CabX DacX DcbX Jabc Jbca
XIX	CabX DacX DcbX Fcab Jbca
XX	AabX CcaX DbaX DcbX Jabc
XXI	AabX BcaX DabX Hcba
XXII	AabX CabX CacX DcbX Jbca
XXIII	AabX AacX CbaX DacX Jbca
XXIV	BabX BacX DbcX Hacb

Bibliography

- V. Avetisov and V. Goldanskii. Mirror symmetry breaking at the molecular level. *Proceedings of the National Academy of Sciences*, 93(21):11435–11442, oct 1996. doi: 10.1073/pnas.93.21.11435. URL <https://doi.org/10.1073/pnas.93.21.11435>.
- N. Barkai and S. Leibler. Robustness in simple biochemical networks. *Nature*, 387(6636):913–917, jun 1997. doi: 10.1038/43199. URL <https://doi.org/10.1038/43199>.
- U. S. Bhalla. MAP Kinase Phosphatase As a Locus of Flexibility in a Mitogen-Activated Protein Kinase Signaling Network. *Science*, 297(5583):1018–1023, aug 2002. doi: 10.1126/science.1068873. URL <https://doi.org/10.1126/science.1068873>.
- Upinder S Bhalla. Signaling in small subcellular volumes. I. Stochastic and diffusion effects on individual pathways. *Biophysical journal*, 87(2):733–44, aug 2004a. ISSN 0006-3495. doi: 10.1529/biophysj.104.040469. URL <http://dx.doi.org/10.1529/biophysj.104.040469>.
- Upinder S Bhalla. Models of cell signaling pathways. *Current Opinion in Genetics & Development*, 14(4):375–381, aug 2004b. doi: 10.1016/j.gde.2004.05.002. URL <https://doi.org/10.1016/j.gde.2004.05.002>.
- Upinder S. Bhalla and Ravi Iyengar. Robustness of the bistable behavior of a biological signaling feedback loop. *Chaos (Woodbury, N.Y.)*, 11(1):221–226, mar 2001. ISSN 1089-7682. doi: 10.1063/1.1350440. URL <http://www.ncbi.nlm.nih.gov/pubmed/12779455>.
- US Bhalla. Signaling in small subcellular volumes. II. Stochastic and diffusion effects on synaptic network properties. *Biophys J*, 87:745–53, Aug 2004c.
- Dong-Eun Chang, Shelly Leung, Mariette R Atkinson, Aaron Reifler, Daniel Forger, and Alexander J Ninfa. Building biological memory by linking positive feedback

- loops. *Proceedings of the National Academy of Sciences of the United States of America*, 107(1):175–80, jan 2010. ISSN 1091-6490. doi: 10.1073/pnas.0908314107. URL <http://www.ncbi.nlm.nih.gov/pmc/articles/PMC2806707/>.fcgi?artid=2806707&tool=pmcentrez&rendertype=abstract.
- Zhang Cheng, Feng Liu, Xiao-Peng Zhang, and Wei Wang. Robustness analysis of cellular memory in an autoactivating positive feedback system. *FEBS letters*, 582(27):3776–82, nov 2008. ISSN 0014-5793. doi: 10.1016/j.febslet.2008.10.005. URL <http://www.ncbi.nlm.nih.gov/pubmed/18930050><http://www.sciencedirect.com/science/article/pii/S0014579308008223>.
- G Cooper and AC Rios. Enantiomer excesses of rare and common sugar derivatives in carbonaceous meteorites. *Proc Natl Acad Sci U S A*, 113:E3322–31, Jun 2016.
- D. Curtin, S. Hegarty, D. Goulding, J. Houlihan, Th. Busch, C. Masoller, and G. Huyet. Distribution of residence times in bistable noisy systems with time-delayed feedback. *Physical Review E*, 70(3):031103, sep 2004. ISSN 1539-3755. doi: 10.1103/PhysRevE.70.031103. URL <http://link.aps.org/doi/10.1103/PhysRevE.70.031103>.
- P. DECKER. Evolution in Open Systems: Bistability and the Origin of Molecular Asymmetry. *Nature New Biology*, 241(107):72–74, jan 1973. doi: 10.1038/newbio241072a0. URL <https://doi.org/10.1038%2Fnewbio241072a0>.
- Jared L. Deutsch and Clayton V. Deutsch. Latin hypercube sampling with multidimensional uniformity. *Journal of Statistical Planning and Inference*, 142(3):763 – 772, 2012. ISSN 0378-3758. doi: <https://doi.org/10.1016/j.jspi.2011.09.016>. URL <http://www.sciencedirect.com/science/article/pii/S0378375811003776>.
- Sven Dorkenwald, Nicholas L. Turner, Thomas Macrina, Kisuk Lee, Ran Lu, Jingpeng Wu, Agnes L. Bodor, Adam A. Bleckert, Derrick Brittain, Nico Kemnitz, William M. Silver-

smith, Dodam Ih, Jonathan Zung, Aleksandar Zlateski, Ignacio Tartavull, Szi-Chieh Yu, Sergiy Popovych, William Wong, Manuel Castro, Chris S. Jordan, Alyssa M. Wilson, Emmanouil Froudarakis, JoAnn Buchanan, Marc Takeno, Russel Torres, Gayathri Mahalingam, Forrest Collman, Casey Schneider-Mizell, Daniel J. Bumbarger, Yang Li, Lynne Becker, Shelby Suckow, Jacob Reimer, Andreas S. Tolias, Nuno Maçarico da Costa, R. Clay Reid, and H. Sebastian Seung. Binary and analog variation of synapses between cortical pyramidal neurons. dec 2019. doi: 10.1101/2019.12.29.890319. URL <https://doi.org/10.1101%2F2019.12.29.890319>.

John Ellson, Emden Gansner, Lefteris Koutsofios, Stephen C North, and Gordon Woodhull. Graphviz—open source graph drawing tools. In *International Symposium on Graph Drawing*, pages 483–484. Springer, 2001.

James E. Ferrell. Feedback regulation of opposing enzymes generates robust all-or-none bistable responses. *Current Biology*, 18(6):R244–R245, mar 2008. doi: 10.1016/j.cub.2008.02.035. URL <https://doi.org/10.1016%2Fj.cub.2008.02.035>.

F.C. Frank. On spontaneous asymmetric synthesis. *Biochimica et Biophysica Acta*, 11:459–463, jan 1953. doi: 10.1016/0006-3002(53)90082-1. URL <https://doi.org/10.1016%2F0006-3002%2853%2990082-1>.

Daniel T Gillespie. Exact stochastic simulation of coupled chemical reactions. *The Journal of Physical Chemistry*, 81(25):2340–2361, dec 1977. ISSN 0022-3654. doi: 10.1021/j100540a008. URL <http://pubs.acs.org/doi/abs/10.1021/j100540a008>.

Hiroaki Kitano. Biological robustness. *Nature reviews. Genetics*, 5(11):826–37, nov 2004. ISSN 1471-0056. doi: 10.1038/nrg1471. URL <http://www.ncbi.nlm.nih.gov/pubmed/15520792>.

HA Kramers. Brownian motion in a field of force and the diffusion model of chemical reactions.

Physica, (4):284–304, 1940. URL <http://www.sciencedirect.com/science/article/pii/S0031891440900982>.

John E Lisman and Anatol M Zhabotinsky. A Model of Synaptic Memory. *Neuron*, 31(2):191–201, aug 2001. doi: 10.1016/s0896-6273(01)00364-6. URL <https://doi.org/10.1016%2Fs0896-6273%2801%2900364-6>.

R Milo, S Shen-Orr, S Itzkovitz, N Kashtan, D Chklovskii, and U Alon. Network motifs: simple building blocks of complex networks. *Science (New York, N.Y.)*, 298(5594):824–7, oct 2002. ISSN 1095-9203. doi: 10.1126/science.298.5594.824. URL <http://www.ncbi.nlm.nih.gov/pubmed/12399590>.

Sahil Moza. . (2019, February 27). sahilm89/lhsmdu: First release for this code (Version v1.0.0). Zenodo., 2019.

Nicolas Le Novère, Michael Hucka, Huaiyu Mi, Stuart Moodie, Falk Schreiber, Anatoly Sorokin, Emek Demir, Katja Wegner, Mirit I Aladjem, Sarala M Wimalaratne, Frank T Bergman, Ralph Gauges, Peter Ghazal, Hideya Kawaji, Lu Li, Yukiko Matsuoka, Alice Villéger, Sarah E Boyd, Steven Watterson, Guanming Wu, Igor Goryanin, Douglas B Kell, Chris Sander, and Herbert Sauro. The Systems Biology Graphical Notation. *Nature Biotechnology*, 27(8):735–741, 2009. ISSN 1087-0156. doi: 10.1038/nbt.1558. URL <http://www.nature.com/doifinder/10.1038/nbt.1558>.

Benjamin Pfeuty and Kunihiko Kaneko. The combination of positive and negative feedback loops confers exquisite flexibility to biochemical switches. *Physical Biology*, 6(4):046013, nov 2009. doi: 10.1088/1478-3975/6/4/046013. URL <https://doi.org/10.1088%2F1478-3975%2F6%2F4%2F046013>.

Naren Ramakrishnan and Upinder S Bhalla. Memory switches in chemical reaction space. *PLoS*

- computational biology*, 4(7):e1000122, jan 2008. ISSN 1553-7358. doi: 10.1371/journal.pcbi.1000122. URL <http://dx.plos.org/10.1371/journal.pcbi.1000122>.
- Subhasis Ray, Raamesh Deshpande, Niraj Dudani, and Upinder S Bhalla. A general biological simulator: the multiscale object oriented simulation environment MOOSE. *BMC Neuroscience*, 9(Suppl 1):P93, 2008. doi: 10.1186/1471-2202-9-s1-p93. URL <https://doi.org/10.1186%2F1471-2202-9-s1-p93>.
- Takanori Shibata, Hiroshi Morioka, Tadakatsu Hayase, Kaori Choji, and Kenso Soai. Highly Enantioselective Catalytic Asymmetric Automultiplication of Chiral Pyrimidyl Alcohol. *Journal of the American Chemical Society*, 118(2):471–472, jan 1996. doi: 10.1021/ja953066g. URL <https://doi.org/10.1021%2Fja953066g>.
- Cristobal Viedma. Chiral Symmetry Breaking During Crystallization: Complete Chiral Purity Induced by Nonlinear Autocatalysis and Recycling. *Physical Review Letters*, 94(6), feb 2005. doi: 10.1103/physrevlett.94.065504. URL <https://doi.org/10.1103%2Fphysrevlett.94.065504>.
- L Wang, BL Walker, S Iannaccone, D Bhatt, PJ Kennedy, and WT Tse. Bistable switches control memory and plasticity in cellular differentiation. *Proc Natl Acad Sci U S A*, 106:6638–43, Apr 2009.
- Thomas Wilhelm. The smallest chemical reaction system with bistability. *BMC systems biology*, 3(1):90, jan 2009. ISSN 1752-0509. doi: 10.1186/1752-0509-3-90. URL <http://www.biomedcentral.com/1752-0509/3/90>.

Supplementary Figures

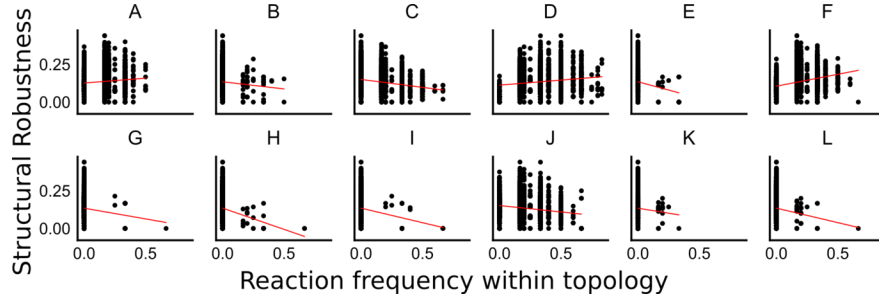


Figure 2.7: The relationship between the Structural Robustness for a topology, with the fraction of occurrence of a given reaction type within the topology. None of the reactions shows a strong correlation with structural robustness, suggesting that different structures may be required for different topologies to increase Structural Robustness.

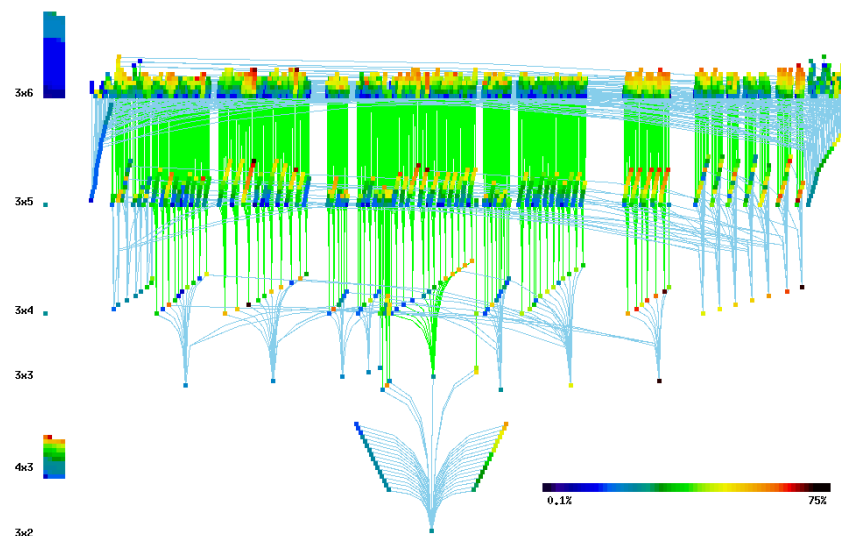


Figure 2.8: Taken from Ramakrishnan and Bhalla (2008, doi: <https://doi.org/10.1371/journal.pcbi.1000122>). This figure shows the relatedness (edges) between the different CRNs (nodes) and their propensity to be bistable (node colors). Different layers denote different dimensionalities (labelled on the left) of the CRNs. Nodes without any edges coming from bottom (smaller dimensionality) are the 80 root CRNs. This includes both 56 orphan nodes (stacked on the left), and the 24 root group CRNs.

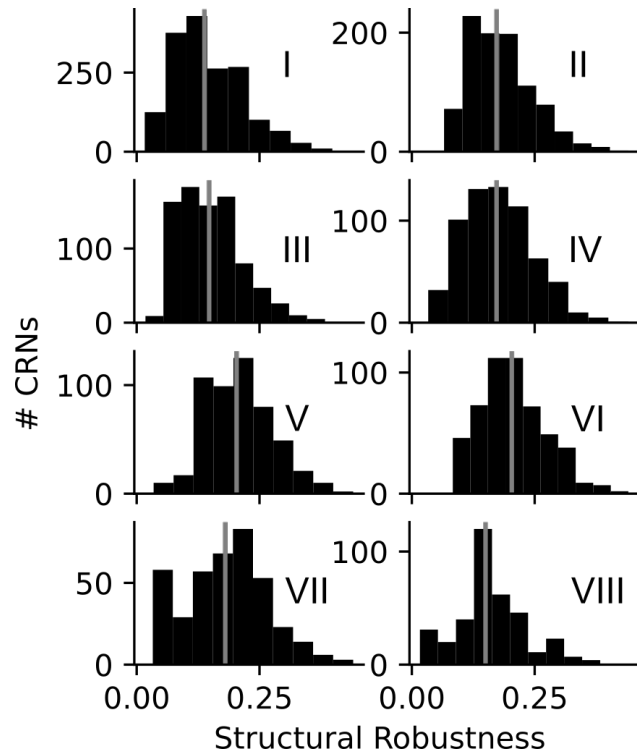


Figure 2.9: Distribution of structural robustness of CRNs organized by root groups. Group V and VI have the highest median structural robustness followed by Group VII. Group V and VI had about 30% members common to both the root groups.

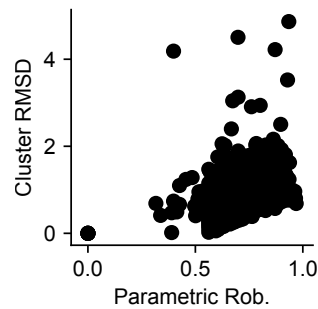
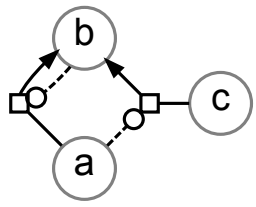
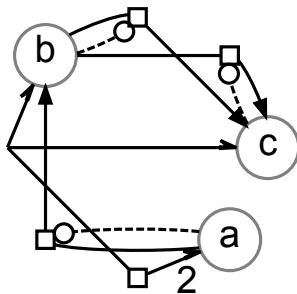


Figure 2.10: A comparison of parametric robustness of CRNs with the root mean square distance between all the saddle points (bistable thresholds) belonging to each CRNs.

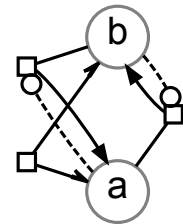
Non bistable topologies



$|DabX|Jcab|$

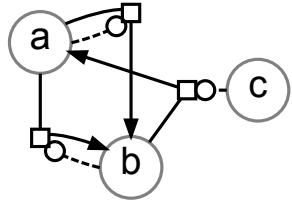


$|CabX|CbcX|DbcX|Fabc|$

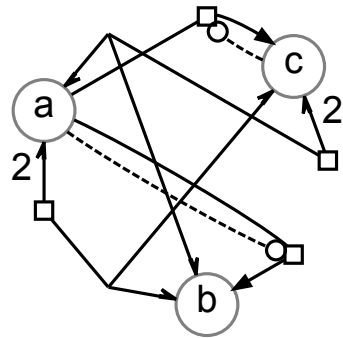


$|AabX|DabX|DbaX|$

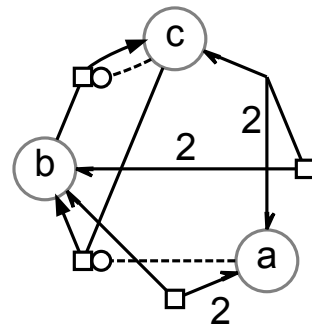
Bistable topologies



$|CabX|DabX|Jbca|$



$|CabX|DacX|Fabc|Fcab|$



$|BabX|DbcX|Hacb|Jcab|$

Figure 2.11: A few examples of bistable and non-bistable CRNs along with their reaction signatures.

Chapter 3

Precise excitation-inhibition balance controls gain and timing in the hippocampus

In this chapter I discuss the observation of precise excitation-inhibition balance and subthreshold divisive normalization in the feed-forward inhibitory circuit of hippocampal CA3-CA1. The manuscript was published in eLife, which is an open access journal. It has been directly attached as a chapter for this thesis. This work was jointly conceptualized by the authors. Aanchal Bhatia and I are the co-first authors. Aanchal did the experiments and I did the theoretical modeling and the data analysis for this paper.

Main article



Precise excitation-inhibition balance controls gain and timing in the hippocampus

Aanchal Bhatia, Sahil Moza, Upinder Singh Bhalla*

National Centre for Biological Sciences, Tata Institute of Fundamental Research, Bangalore, India

Abstract Excitation-inhibition (EI) balance controls excitability, dynamic range, and input gating in many brain circuits. Subsets of synaptic input can be selected or ‘gated’ by precise modulation of finely tuned EI balance, but assessing the granularity of EI balance requires combinatorial analysis of excitatory and inhibitory inputs. Using patterned optogenetic stimulation of mouse hippocampal CA3 neurons, we show that hundreds of unique CA3 input combinations recruit excitation and inhibition with a nearly identical ratio, demonstrating precise EI balance at the hippocampus. Crucially, the delay between excitation and inhibition decreases as excitatory input increases from a few synapses to tens of synapses. This creates a dynamic millisecond-range window for postsynaptic excitation, controlling membrane depolarization amplitude and timing via subthreshold divisive normalization. We suggest that this combination of precise EI balance and dynamic EI delays forms a general mechanism for millisecond-range input gating and subthreshold gain control in feedforward networks.

DOI: <https://doi.org/10.7554/eLife.43415.001>

Introduction

Individual neurons in the brain can receive tens of thousands of excitatory (E) and inhibitory (I) synaptic inputs. Under normal conditions, the ratio of excitatory to inhibitory input remains invariant, a robust property of the nervous system, termed EI balance (*Anderson et al., 2000; Atallah and Scanziani, 2009; Okun and Lampl, 2008; Okun and Lampl, 2009; Wehr and Zador, 2003*). Disruption of balance is linked with several pathologies, including epilepsy, autism spectrum disorders and schizophrenia (*Yizhar et al., 2011*).

Theoretically, neurons in ‘detailed balanced’ EI networks receive balanced responses from all subsets of presynaptic inputs (*Vogels and Abbott, 2009*), and neurons in ‘tightly balanced’ EI networks receive inputs balanced at fast (<10 ms) timescales (*Denève and Machens, 2016*). Together, these properties constitute a ‘precisely balanced’ network (*Hennequin et al., 2017*). This precise balance on all synaptic subsets can be exploited by the brain for ‘input gating’. In this process, neurons can be driven by selective shifts in EI ratios at specific inputs, while other inputs remain balanced in the background. This constitutes a flexible and instantaneous information channel local to the shifted synapses (*Kremkow et al., 2010; Vogels and Abbott, 2009*).

Our current understanding of EI balance is based on measurements made at single neurons in response to various stimuli. Strong EI correlations have been seen in response to series of tones in auditory cortex (*Wehr and Zador, 2003; Zhang et al., 2003; Zhou et al., 2014*), whisker stimulation in somatosensory cortex (*Wilent and Contreras, 2005*), during cortical up states in vitro (*Shu et al., 2003*) and in vivo (*Haider et al., 2006*), during gamma oscillations in vitro and in vivo (*Atallah and Scanziani, 2009*), and during spontaneous activity (*Okun and Lampl, 2008*). At the synaptic scale, the ratio of excitatory and inhibitory synapses on various dendrites of a neuron has been shown to

*For correspondence:
bhalla@ncbs.res.in

Competing interest: See
page 24

Funding: See page 24

Received: 06 November 2018

Accepted: 10 April 2019

Published: 25 April 2019

Reviewing editor: Ronald L
Calabrese, Emory University,
United States

© Copyright Bhatia et al. This article is distributed under the terms of the [Creative Commons Attribution License](#), which permits unrestricted use and redistribution provided that the original author and source are credited.

be conserved (*Iascone et al., 2018*). However, the precision and presynaptic origin of balance is not well understood. It remains to be established if EI balance arises transiently from complex temporal dynamics of several presynaptic layers, if it requires summation of inputs from multiple presynaptic populations, or if it exists even at subsets of a single presynaptic population. This granularity of EI balance, of both presynaptic identity and number of inputs, can determine the precision with which synaptic inputs can be selected or ‘independently gated’ to affect postsynaptic activity.

In this study, we address two key open questions in the field. First, can EI balance arise even in a single layer feedforward network, and if so, at what granularity of network subsets do postsynaptic cells experience balanced excitation and inhibition? Second, how do excitation and inhibition integrate to encode and communicate information at the postsynaptic neuron? We addressed these questions *in vitro*, to isolate the hippocampal network from background activity, and to deliver precisely controlled combinatorial stimuli. We stimulated channelrhodopsin-2 (ChR2) expressing CA3 neurons in several combinations using optical patterns, and measured responses in CA1.

We report that hundreds of randomly chosen subsets of CA3 neurons provide excitatory and feedforward inhibitory inputs to CA1 cells with a close to identical ratio, demonstrating for the first time, precise balance (*Hennequin et al., 2017*) in the brain. On examining the integration of excitation and feedforward inhibition, we found that inhibition arrives with a dynamically varying onset delay that decreases with increasing input amplitude. This leads to a characteristic initial linear portion in the neuronal input-output curve where the inhibition arrives too late to affect peak depolarization, and a progressively diminishing output as the EI delay decreases with increasing input. This novel gain control operation, termed Subthreshold Divisive Normalization (SDN) encodes input information in both amplitude and timing of the CA1 response.

Results

In our study, we first utilize and characterize an optical stimulation protocol for CA3 pyramidal neurons, and measure intracellular responses at CA1 pyramidal neurons (*Figure 1*). We then demonstrate precise EI balance for various combinations of CA3 inputs at CA1 using voltage clamp to separate the E and I components (*Figure 2*). Next, we measure the depolarization at CA1 due to summation of E and I using different input combinations (*Figure 3*), and show sublinearity of summation. Expansion of the range of inputs revealed divisive normalization and suggested that another factor such as inhibitory kinetics should be included to account for the sublinearity (*Figure 4*). In *Figure 5*, we confirm that blocking inhibition leads to much reduced sublinearity of summation, and that inhibition scales linearly with stimulus amplitude. We then establish that inhibitory delay is crucial for explaining the sublinearity in SDN (*Figure 6*). In *Figure 7*, we show that post-synaptic potential peak amplitude and timing both carry information about the summed stimulus amplitude, and show that this information carries over to spike timing. In *Figure 8*, we summarize the analysis and suggest how SDN could contribute to input gating in the hippocampus.

Optical stimuli at CA3 elicit subthreshold responses at CA1

To provide a wide range of non-overlapping stimuli, we projected patterned optical stimuli onto channelrhodopsin-2 (ChR2) expressing CA3 neurons in acute hippocampal slices. We used CA3-cre mice to achieve CA3-specific localization of ChR2 upon injection of a Lox-ChR2 virus (*Figure 1a*, Materials and methods). We used a Digital Micromirror Device (DMD) projector (Materials and methods, *Figure 1—figure supplement 1*) to generate spatiotemporal optical patterns in the form of a grid of several 16 $\mu\text{m} \times 16 \mu\text{m}$ squares, each square approximating the size of a CA3 soma (*Ishizuka et al., 1995*) (*Figure 1d*). This grid was centered at the CA3 cell body layer, and extended to the dendritic layer (*Figure 1a*). Each optical pattern consisted of 1 to 9 such randomly chosen grid squares, presented to CA3 cells as stimulus, at an inter-stimulus interval of 3 s (*Figure 1a,d*, Materials and methods). In a typical experiment, several randomly chosen stimulus patterns with different number of input squares were delivered to CA3, in three successive repeats. We first characterized how CA3 responded to the grid stimulation (*Figure 1b,e,f,g*). CA3 neurons fired reliably with a < 2 ms jitter, calculated as the standard deviation of the time of first spike (*Figure 1f*) ($n = 8$ CA3 cells, inputs = 52, median = 0.44 ms, $N = 1$ to 9 squares). No desensitization occurred during the timeframe of an experiment, and the probability of spiking remained constant between

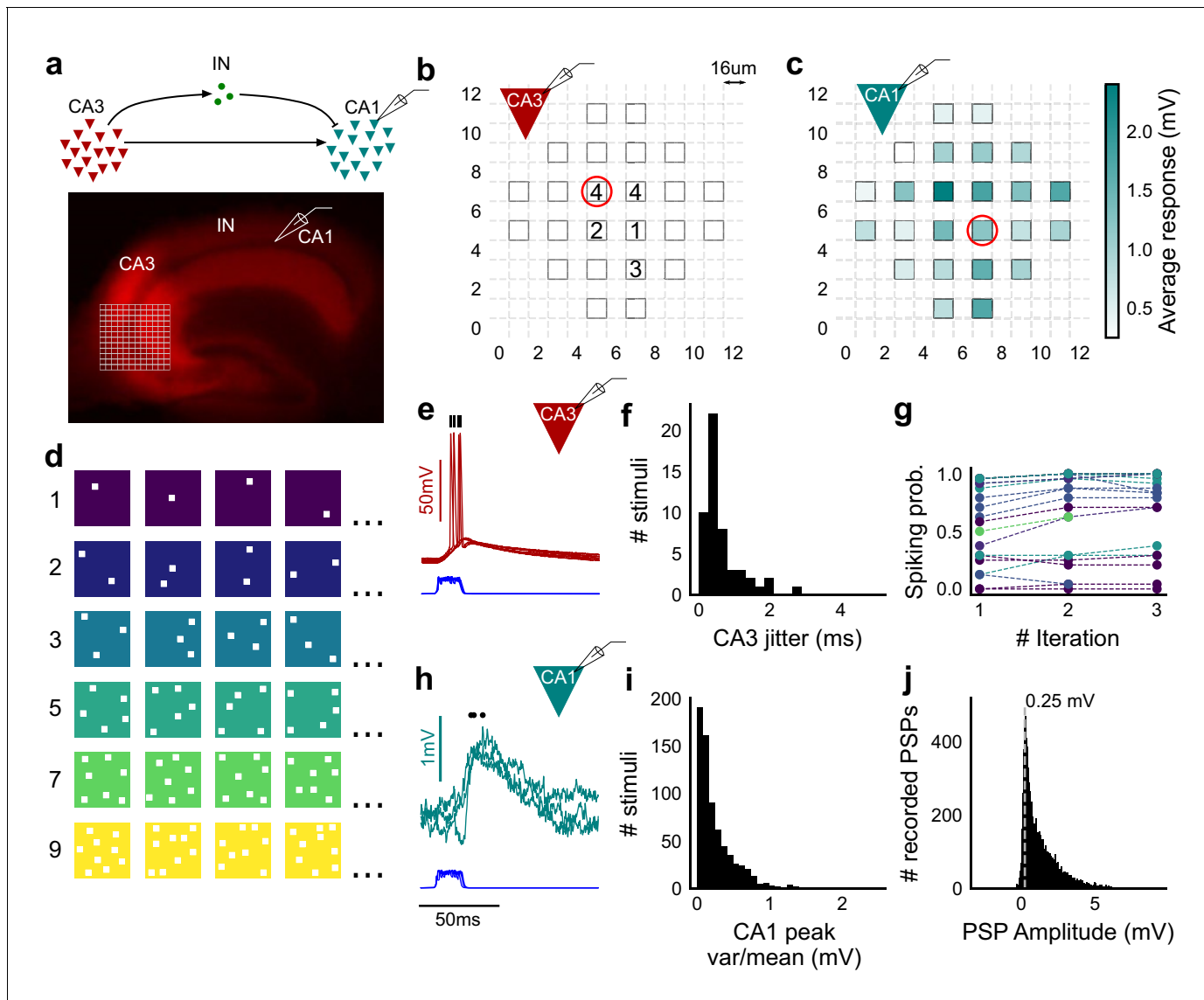


Figure 1. Stimulating CA3-CA1 network with hundreds of optical patterns. (a) Top, schematic of the CA3-CA1 circuit with direct excitation and feedforward inhibition. Bottom, image of a hippocampus slice expressing ChR2-tdTomato (red) in CA3 in a Cre-dependent manner. Optical stimulation grid (not drawn to scale) was centered at the CA3 cell body layer and CA1 neurons were patched. (b) Spike response map of CA3 neuron responses with one grid square active at a time. A CA3 neuron was patched and optically stimulated, in random spatio-temporal order, on the grid locations marked with grey border. This cell spiked (marked with number inside representing spike counts over four trials) in 5 out of 24 such one square stimuli delivered. (c) Heatmap of CA1 responses while CA3 neurons were stimulated with one square optical stimuli. Colormap represents peak V_m change averaged over three repeats. (d) Schematic of optical stimulus patterns. Examples of combinations of N-square stimuli where N could be 1, 2, 3, 5, 7 or 9 (in rows). (e) Spikes in response to four repeats for the circled square, in b. Spike times are marked with a black tick, showing variability in evoked peak times. Blue trace at the bottom represents photodiode measurement of the stimulus duration. Scale bar for time, same as h. (f) Distribution of jitter in spike timing (SD) for all CA3 cells ($n = 8$ cells). (g) CA3 spiking probability (fraction of times a neuron spiked across 24 stimuli, repeated thrice) is consistent over a single recording session. Randomization of the stimulus pattern prevented ChR2 desensitization. Circles, colored as in d depict spiking probability on each repeat of a stimulus set with connecting lines tracking three repeats of the set ($n = 7$ cells). (h) PSPs in response to three repeats of the circled square in c. Peak times are marked with an asterisk. Blue traces at the bottom represent corresponding photodiode traces for the stimulus duration. (i) Distribution of peak PSP amplitude variability (variance/mean) for all 1-square responses ($n = 28$ cells, stimuli = 695). (j) Histogram of peak amplitudes of all PSPs elicited by all 1-square stimuli, over all CA1 cells. Grey dotted line marks the mode ($n = 38$ cells, trials = 8845).

DOI: <https://doi.org/10.7554/eLife.43415.002>

The following figure supplement is available for figure 1:

Figure supplement 1. Experiment design.

Figure 1 continued on next page

Figure 1 continued

DOI: <https://doi.org/10.7554/eLife.43415.003>

the three repeats (**Figure 1g**) ($n = 7$ CA3 cells, $N = 1$ to 9 squares). Thus, we could stimulate CA3 with hundreds of distinct optical stimuli in each experiment.

We then recorded postsynaptic potentials (PSPs) evoked at patched CA1 neurons while optically stimulating CA3 cells (**Figure 1c,h,i,j**). A wide range of stimulus positions in CA3 excited CA1 neurons (**Figure 1c**). Stimulation of CA3 elicited excitation and feedforward inhibition at CA1 (**Figure 1a**, **Figure 2**). Most stimuli elicited subthreshold responses ($N = 1$ to 9 squares). Action potentials occurred in only 0.98% of trials (183 out of 18,668 trials, $n = 38$ cells, $N = 1$ to 9 squares). This helped rule out any significant feedback inhibition from CA1 interneurons for all our experiments. Restriction of ChR2 to CA3 pyramidal cells, coupled with the fact that ~99% of all recorded CA1 responses were subthreshold, ensured that the recorded inhibition was largely feedforward (disynaptic) (**Figure 1a**). Responses to the same 1-square stimulus were consistent, 84.74% responses showed less than 0.5 variance by mean (695 stimuli, three repeats each, $n = 28$ cells, $N = 1$ square) (**Figure 1i**). Notably, the distribution of all one square responses had a mode at 0.25 mV, which is close to previous reports of a 0.2 mV somatic response of single synapses in CA1 neurons (**Magee and Cook, 2000**) (8845 trials, $n = 38$ cells, $N = 1$ square) (**Figure 1j**).

Arbitrarily chosen CA3 inputs show precise EI balance at CA1

To examine the relationship between excitation and inhibition, we voltage clamped CA1 neurons, first at the inhibitory (-70 mV) and then at the excitatory (0 mV) reversal potential to record Excitatory and Inhibitory Post Synaptic Currents (EPSCs and IPSCs) respectively. We first presented five different patterns of 5 squares each, at both of these potentials, and recorded EPSCs and IPSCs. We found strong proportionality between excitation and inhibition for every stimulus pattern (**Figures 1d** and **2a**). This suggested that inputs from even random groups of CA3 neurons may be balanced at CA1. Repeats with the same stimulus pattern gave consistent responses, but different patterns evoked different responses (**Figure 2a**, **Figure 2—figure supplement 1b**). This indicated that the optically driven stimuli were able to reliably activate different subsets of synaptic inputs on the target neuron. Next, we asked, in what range of input strengths does random input yield balance? We presented five different patterns for each of 1, 2, 3, 5, 7 or 9 square combinations at both recording potentials. Surprisingly, all stimuli to a cell elicited excitatory and inhibitory responses in the same ratio, irrespective of response amplitude (**Figure 2b,c**) ($n = 13$ CA1 cells, area under curve, mean $R^2 = 0.89 + /- 0.06$ SD, **Figure 2—figure supplement 2**). Notably, the mode of single-square responses was ~0.25 mV, close to single synapse PSP estimates (**Magee and Cook, 2000**) (**Figure 1j**). However, accounting for the low (~0.2) release probabilities (P_r) at the CA3-CA1 synapse (**Murthy et al., 1997**), we should be able to see a single synapse response if approximately 1/ P_r synapses were activated. Hence, we estimate that the granularity of the balance as resolved by our method is of the order of 5–10 synapses (**Figure 2—figure supplement 1d,e**). The slope of the regression line through all stimulus-averaged responses for a CA1 cell was used to calculate the Inhibition/Excitation (I/E) ratio for the cell. IPSC/EPSC ratio was typically between 2 and 5 (**Figure 2d**). The variability of I/E ratios over all stimuli for a cell was lower than the variability of all stimuli across cells (for 12 out of 13 cells, **Figure 2—figure supplement 1c**). The high R^2 values for all cells showed tight proportionality for all stimuli (**Figure 2e**). The residual distribution remained symmetric for increasing numbers of spots, again showing that they were not affected by the number of stimulus squares presented (**Figure 2—figure supplement 1a**). While feedforward inhibition is expected to increase with excitation, convergence of I/E ratios for randomly chosen inputs to a cell to a single number was unexpected, since shared interneurons consist of only about 10% of the total neuronal population (**Woodson et al., 1989; Bezaire and Soltesz, 2013**).

Detailed balance requires co-tuning of EI weights

We next tested the hypothesis that the observed correlation between excitatory and inhibitory inputs was due to an averaged sum over many untuned (globally balanced) synapses, as opposed to a much finer granularity of tuning between excitatory and inhibitory synaptic weights (detailed

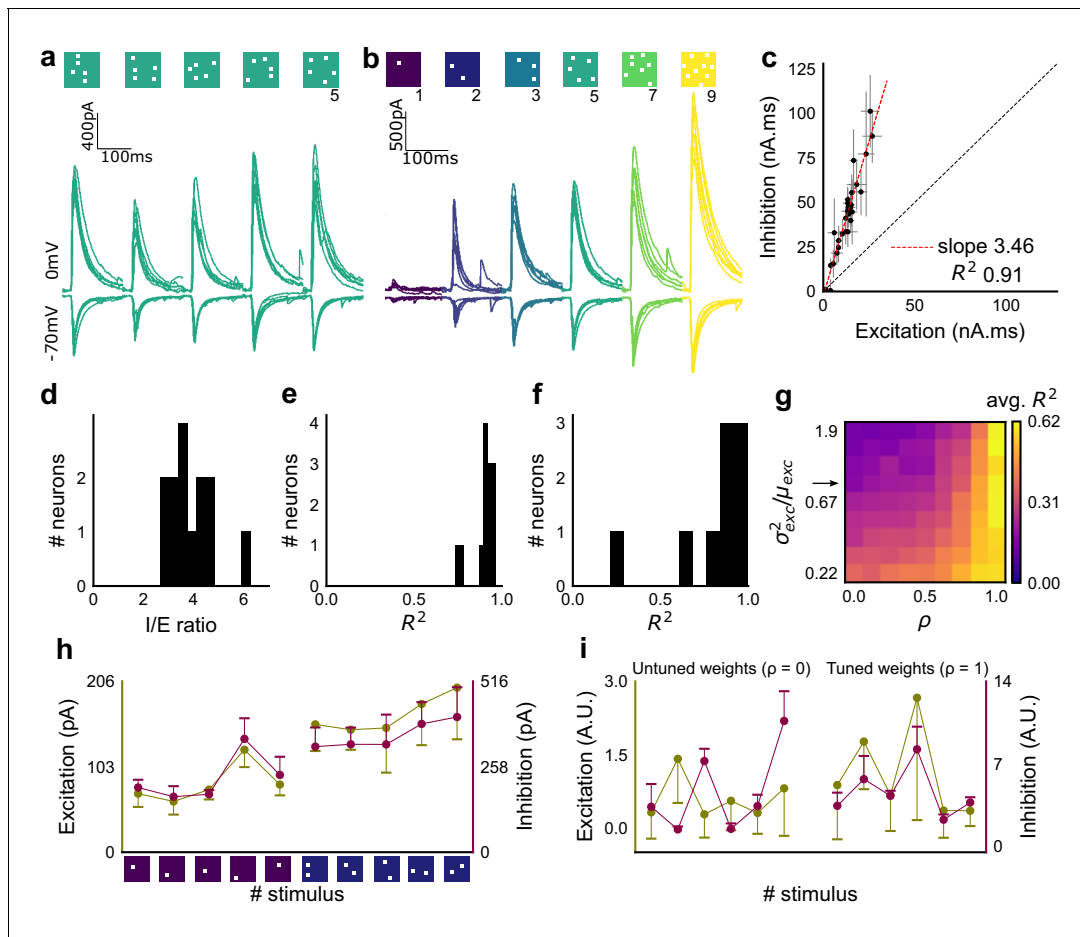


Figure 2. Excitation and inhibition are tightly balanced for all stimuli to a CA1 cell. (a) Monosynaptic excitatory postsynaptic currents (EPSCs, at -70 mV) and disynaptic inhibitory postsynaptic currents (IPSCs, at 0 mV) in response to five different stimulus combinations of 5 squares each. All combinations show proportional excitatory and inhibitory currents over six repeats. Top, schematic of 5-square stimuli. (b) EPSCs and IPSCs are elicited with the same I/E ratio in response to six repeats of a combination, and across six different stimuli from 1 square to nine squares, for the same cell as in a. Top, schematic of the stimuli. (c) Area under the curve for EPSC and IPSC responses, obtained by averaging over six repeats, plotted against each other for all stimuli to the cell in a, b. Error bars are s.d. (d) Summary of I/E ratios for all cells ($n = 13$ cells). (e) Summary for all cells of R^2 values of linear regression fits through all points. Note that 11 out of 13 cells had R^2 greater than 0.9, implying strong proportionality. (f) Same as e, but with linear regression fits for 1 and 2 square responses, showing that even small number of synapses are balanced for excitation and inhibition ($n = 9$ cells). (g) Phase plot from the model showing how tuning of synapses (ρ) affects observation of EI balance (R^2) for various values of variance/mean of the basal weight distribution. Changing the scale of the basal synaptic weight distributions against tuning parameter ρ affects goodness of EI balance fits. Arrow indicates where our observed synaptic weight distribution lay. (h) Example of EI correlations (from data) for 1 and 2 square inputs for an example cell. Bottom, schematic of the stimuli. Excitation and inhibition are colored olive and purple, respectively. Error bars are s.d. (i) Examples of EI correlation (from model) for small number of synapses, from the row marked with arrow in g. The left and right curves show low and high correlations in mean amplitude when EI synapses are untuned ($\rho = 0$) and tuned respectively ($\rho = 1$) (AU = Arbitrary Units). Colors, same as h. Error bars are s.d.

DOI: <https://doi.org/10.7554/eLife.43415.004>

The following figure supplements are available for figure 2:

Figure supplement 1. Detailed balance in CA3-CA1 feedforward network.

DOI: <https://doi.org/10.7554/eLife.43415.006>

Figure supplement 2. Raw data from all cells showing precise balance between excitation and inhibition.

DOI: <https://doi.org/10.7554/eLife.43415.005>

balance). To address this, we modelled excitatory and inhibitory synaptic weights to a neuron with different amounts of weight tuning, parameterized by rho (ρ), which takes values between 0 (no tuning or global balance) and 1 (detailed balance) (Materials and methods, **Figure 2—figure supplement 1h**). For values between 0 and 1, ρ determined the degree of correlation between the basal excitatory and inhibitory synaptic weights. To test if weight tuning was necessary to observe balance,

we modeled the summation of synaptic inputs with the premise that excitatory and inhibitory afferents will be activated strictly proportionally (number balance). We then tested how mean and variance correlations between EI amplitudes changed with different degrees of weight tuning.

We observed tight correlations between EI inputs without weight tuning, but only if the basal synaptic weight distribution was narrow. Further, for a narrow weight distribution, the change from global to detailed balance had little effect on mean EI amplitude correlations. In contrast, weight tuning was required to see EI balance for wider synaptic weight distributions, especially for stimuli which activated small numbers of synapses (*Figure 2g*). We next calculated the width of the smallest responses (1-square GABA_A EPSP) as a proxy for the basal weight distribution (*Figure 3—figure supplement 1a*). The observed responses were broadly distributed. With this basal weight distribution, the model exhibited EI balance only when the excitatory and inhibitory synaptic weights were co-tuned, that is, maintained at the same ratio (marked with arrow in *Figure 2g*, Materials and methods, *Figure 2—figure supplement 1h*).

With the reasoning developed above, we checked for EI balance in the smallest inputs in our datasets - 1 and 2 square data from voltage clamped cells (having five or more input patterns per cell) (*Figure 2—figure supplement 1d*), and only one square from current clamped cells (24 inputs per cell) (*Figure 2—figure supplement 1e,f*). We found that the responses corresponding to a few synapses per input were balanced (*Figures 1j* and *2f,h*, *Figure 2—figure supplement 1d,e,f*), suggesting tuning of excitatory and inhibitory weights.

In addition, the model also predicted a tuning dependent change in the correlations of variability of excitation and inhibition amplitudes for repeats of the same stimulus. For a wide synaptic weight distribution, increase in tuning increased EI variability correlations (*Figure 2—figure supplement 1i, k*). As with EI mean correlations (*Figure 2h,i*), weight tuning had little effect in the case of narrow synaptic weight distributions. Again, our calculated synaptic weight distribution was in the range where strong variability correlations would be seen only if synaptic weights were tuned. We found strong correlations between excitatory and inhibitory standard deviation between six repeats of the same stimulus in our voltage-clamp dataset, suggesting that there is detailed balance in the network (*Figure 2—figure supplement 1g,j*).

Thus, we present three observations using small (one and two square) stimulus strengths: a wide basal weight distribution, correlated mean EI amplitude and correlated EI amplitude variability. Together, these are inconsistent with the hypothesis that EI balance can emerge with no other requirement than a proportional increase in number of EI afferents in a globally balanced network. This supports the existence of weight tuning and hence detailed balance in the CA3-CA1 network.

Overall, we found stimulus-invariant proportionality of excitation and inhibition for any randomly selected input, over a large range of stimulus strengths from a single presynaptic network. In addition to detailed balance, we show below that there is tight balance, that is the timing of the balanced feedforward inhibition was within a few milliseconds of the excitation (*Figure 6g,h*). Thus, we concluded that the CA3-CA1 circuit exhibits precise (both detailed and tight) balance (*Hennequin et al., 2017*).

Combinatorial CA3 inputs sum sublinearly at CA1

We next asked how CA3 inputs, that lead to balanced excitatory and feedforward inhibitory conductances, transform into membrane potential change at CA1 neurons. Based on anatomical studies, CA3 projections are likely to arrive in a distributed manner over a wide region of the dendritic tree of CA1 pyramidal neuron (*Ishizuka et al., 1990*) (*Figure 3a*). While pairwise summation at CA1 has been shown to be largely linear in absence of inhibition (*Cash and Yuste, 1999*), the degree of heterogeneity of summation in response to spatially distributed excitatory and inhibitory synaptic inputs is not well understood (except, see *Lovett-Barron et al., 2012*). To avoid biases that may arise from a single response measure during input integration (*Poirazi et al., 2003*), we examined PSPs using four different measures (*Figure 3c*). These were peak amplitude, area under curve (AUC), average membrane potential and area under curve till peak (*Figure 3c*).

We looked at input integration by presenting stimulus sets of 5 input squares to a given cell, with each stimulus set ranging from 24 to 225 combinations of inputs. We initially tested the center of our range of 1–9 squares (5-square inputs) before expanding the dataset to the full range (*Figure 4*). We also recorded the responses to all squares of the grid individually (one square input). The one square PSP peak response amplitude with inhibition intact (control) was not distinguishable from

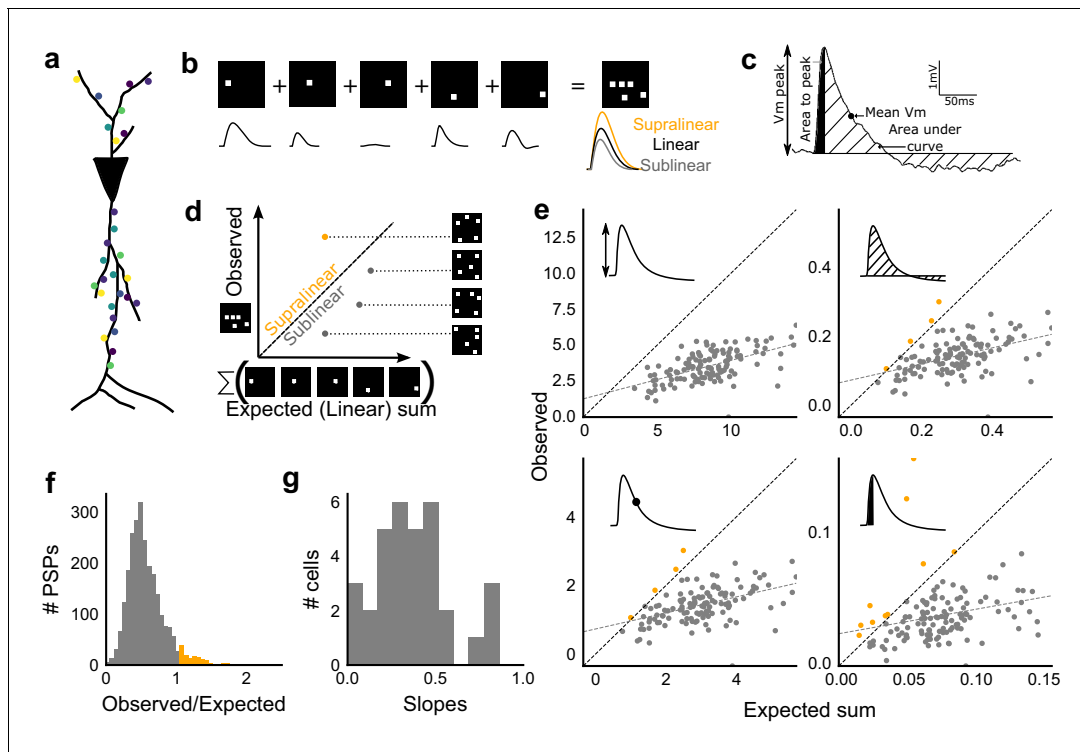


Figure 3. Excitatory and feed-forward inhibitory inputs from CA3 integrate sublinearly at CA1. (a) Schematic of a neuron receiving synaptic input distributed over its dendritic tree. (b) Schematic of input integration. Top, five 1-square stimuli presented individually, and a single 5-square stimulus comprising of the same squares. Bottom, PSPs elicited as a response to these stimuli. 5-square PSP can be larger (supralinear, orange), equal to (linear, black), or smaller (sublinear, grey) than the sum of the single square PSPs. (c) A PSP trace marked with the four measures used for further calculations. PSP peak, PSP area, area to peak and mean voltage are indicated. (d) Schematic of the input integration plot. Each circle represents response to one stimulus combination. ‘Observed’ (true response of 5 square stimulation) on Y-axis and ‘Expected’ (linear sum of 1 square responses) is on X-axis. (e) Most responses for a given cell show sublinear summation for a 5-square stimulus. The four panels show sublinear responses for four different measures (mentioned in c) for the same cell. The grey dotted line is the regression line and the slope of the line is the scaling factor for the responses for that cell. For peak (mV), area (mV.ms), average (mV), and area to peak (mV.ms); slope = 0.27, 0.23, 0.23, 0.18; R^2 0.57, 0.46, 0.46, 0.26, respectively. The responses to AUC and average are similar because of the similarity in the nature of the measure. (f) Distribution of Observed/Expected ratio of peaks of all responses for all 5-square stimuli (mean = 0.57, s.d. = 0.31), from all recorded cells pooled. 93.35% responses to 5-square stimuli were sublinear (2513 PSPs, n = 33 cells). (g) Distribution of slopes for peak amplitude of 5-square stimuli (mean = 0.38, s.d. = 0.22). Regression lines for all cells show that all cells display sublinear (<1 slope) summation (n = 33 cells).

DOI: <https://doi.org/10.7554/eLife.43415.007>

The following figure supplement is available for figure 3:

Figure supplement 1. Summation at CA3-CA1 network is sublinear.

DOI: <https://doi.org/10.7554/eLife.43415.008>

that with inhibition blocked (GABAzine) (Materials and methods, **Figure 3—figure supplement 1a**). As analyzed below (**Figure 6**), we find that the apparent lack of effect of GABAzine for very small inputs is because inhibition arrives with a delay that does not affect the peak response of the neuron (**Video 1**). Since individual neurons may be targeted by more than one grid square (**Figure 1b**), individual spots are not completely independent and may interact, especially given the spread in the CA3 pyramidal neuronal arbor. Our analyses show that this interaction does not have a strong or unidirectional effect on the responses of the combinations of squares (**Figure 4—figure supplement 1**, **Figure 5b,d**). The ‘observed’ response for a given square combination was plotted against the ‘expected’ response, obtained by linearly summing 1-square responses constituting that combination (**Figure 3b,d**). Perfectly linear summation would imply that a multi-square combination of inputs would elicit the same response as the sum of the responses to the individual squares (**Figure 3d**). **Figure 3e** shows responses of a single cell stimulated with 126 distinct 5-square combinations. The ‘observed’ response was sublinear as compared to the ‘expected’ summed response,

for most stimuli (**Figure 3e**). For all the four measures in **Figure 3c**, CA3 inputs summed sublinearly at CA1 (**Figure 3e,g, Figure 3—figure supplement 1c**). At this point, we hypothesised that the observed sublinearity might mostly be due to inhibition divisively scaling excitation, since excitatory and inhibitory conductances were proportional for all stimuli (**Figure 2**). We later tested this hypothesis by blocking inhibition (**Figure 5**). For all responses measured over all cells, 93.35% responses were individually sublinear, with distribution having mean 0.57 ± 0.31 (SD) (**Figure 3f, Figure 3—figure supplement 1d**). The slope of the regression line, which indicated the extent of sublinearity, varied between cells, with mean 0.38 ± 0.22 (SD) ($n = 33$ cells) (**Figure 3g**).

Thus, we found that the CA3-CA1 network exhibits sublinear summation over a large number of inputs.

CA3-CA1 network performs Subthreshold Divisive Normalization

We then tested how summation sublinearity scaled with a larger range of inputs. We noted that non-linear functions can be observed better with a large range of inputs (**Poirazi et al., 2003**), and therefore increased the stimulus range (**Figure 4—figure supplement 2**). GABAergic inhibition has been shown to be responsible for sublinear summation when Schaffer collateral and perforant path inputs are delivered simultaneously to CA1 (**Enoki et al., 2001**). We hypothesized that the sublinearity within the CA3-CA1 network might also occur due to the effect of inhibition. In general, inhibition may interact with excitation to perform arithmetic operations like subtraction, division, and normalization (**Carandini and Heeger, 2011**). In order to predict the operation performed by EI integration at the CA3-CA1 network, we created a composite phenomenological model to fit and test for the above three possibilities: subtractive inhibition, divisive inhibition, and divisive normalization (**Equation (1)**). We later address the mechanism using a biophysical model (**Figure 6**). **Equation (1)** describes how inhibition controls the ‘observed’ response (θ) as a function of ‘expected’ response (ε), for the above three operations. Alpha (α) can be thought to be a subtractive inhibition parameter, beta (β) as a divisive inhibition parameter, and gamma (γ) a normalization parameter (**Figure 4a**).

$$\theta = \varepsilon - \frac{\beta\varepsilon}{\gamma + \varepsilon} \varepsilon - \alpha \quad (1)$$

Using the framework of **Equation (1)**, we asked what computation was performed at the CA3-CA1 network. We recorded from CA1 cells while stimulating CA3 with many combinations of 2, 3, 5, 7 or 9 squares (**Figure 4b**). We selected cells with at least 50 input combinations, and pooled responses from all stimuli to a cell. Then, we fit **Equation (1)** to the PSP amplitudes (**Figure 4b**). From visual inspection, the subtractive inhibition model, $\theta = \varepsilon - \alpha$ (fixing $\beta, \gamma = 0$) was a bad fit, since intercepts (α) were close to 0 (**Figure 4a**).

By fixing γ and α to 0 in **Equation (1)** we obtained the Divisive Inhibition (DI) model. In this form, β can be thought of as I/E ratio. Increasing β decreases the observed response (θ) (**Figure 4a**).

$$\theta = \varepsilon - \beta\varepsilon \quad (2)$$

Similarly, β was fixed to 1 and α to 0 to get the Divisive Normalization (DN) model. This form of the equation was inspired by the analogous canonical divisive normalization equation for firing rates (**Carandini and Heeger, 2011**). Here, decrease in γ implies increase in normalization (**Figure 4a**).

$$\theta = \varepsilon - \frac{\varepsilon}{\gamma + \varepsilon} \varepsilon = \frac{\gamma\varepsilon}{\gamma + \varepsilon} \quad (3)$$

We used least-squares polynomial regression to fit DI and DN models to our data. The goodness of fit for all cells was tested by comparing BIC (Bayesian Information Criterion) (**Figure 4c**) and reduced chi-squares of the models (**Figure 4—figure supplement 2o**, Materials and methods). DN ($\alpha = 0, \beta = 1$) was better than DI ($\alpha = 0, \gamma = 0$) model in explaining the data (BIC: Two-tailed paired t-test, $p < 0.00005$, reduced chi-square: Two-tailed paired t-test, $p < 0.00005$, $n = 32$ cells).

Subthreshold Divisive Normalization (SDN) can be clearly seen in **Figure 4b**, where observed responses to stimuli with 5 mV and 15 mV expected responses are very similar. This shows that SDN allows CA1 cells to integrate a large range of inputs before reaching spike threshold. Thus, testing with a larger range of inputs showed that the initial finding of constant I/E ratios from **Figure 2**

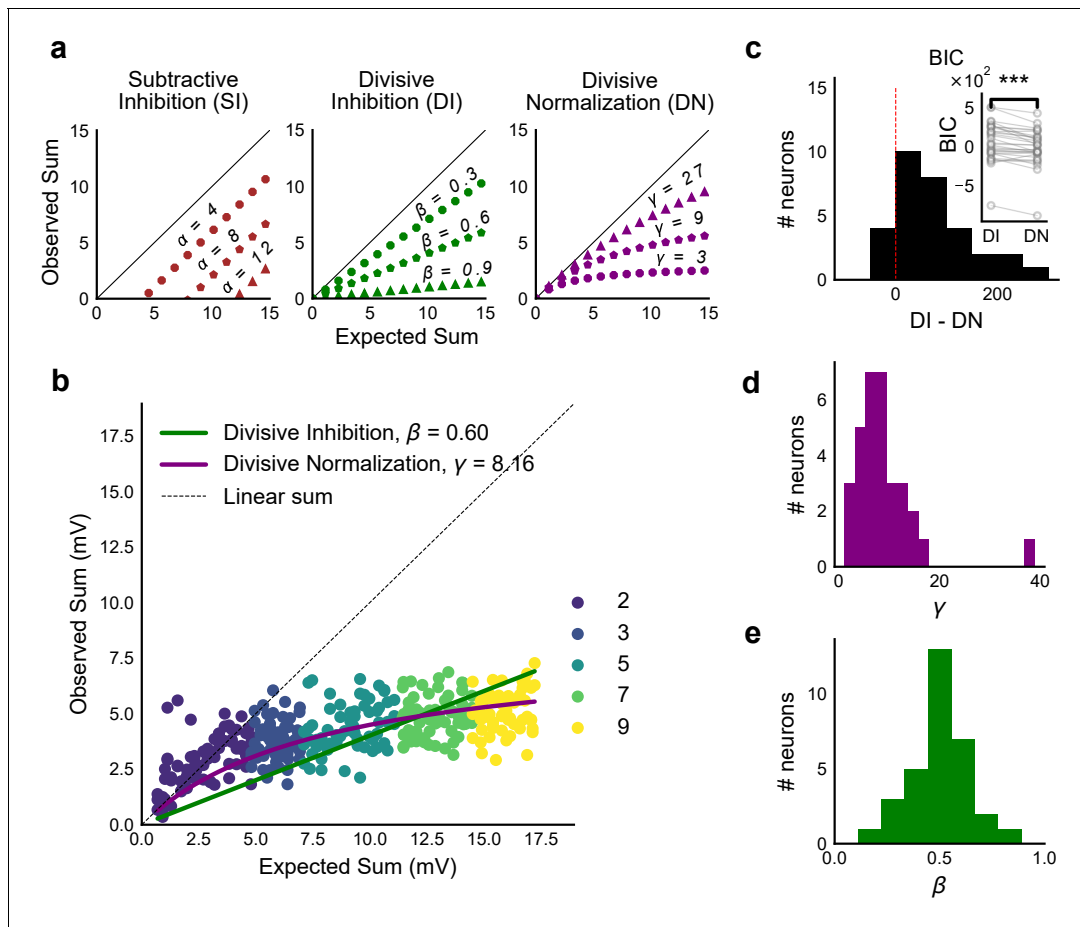


Figure 4. Over a wide input range, integration of CA3 excitatory and feed-forward inhibitory input leads to SDN at CA1. (a) Three phenomenological models of how inhibition interacts with excitation and modulates membrane potential: (left to right) Subtractive Inhibition (SI), Divisive Inhibition (DI) and Divisive Normalization (DN). Note how parameters α , β and γ from **Equation (1)** affect response output. (b) Divisive normalization seen in a cell stimulated with 2, 3, 5, 7 and 9 square combinations. DN and DI model fits are shown in purple and green, respectively. (c) Difference in Bayesian Information Criterion (BIC) values for the two models - DI and DN. Most differences between BIC for DI and DN were less than 0, which implied that DN model fit better, accounting for the number of variables used. Insets show raw BIC values. Raw BIC values were consistently lower for DN model, indicating better fit (Two-tailed paired t-test, $p < 0.00005$, $n = 32$ cells). (d) Distribution of the parameter γ of the DN fit for all cells (median = 7.9, $n = 32$ cells). Compare with a, b to observe the extent of normalization. (e) Distribution of the parameter beta of the DI fit for all cells (mean = 0.5, $n = 32$ cells). Values are less than 1, indicating sublinear behaviour.

DOI: <https://doi.org/10.7554/eLife.43415.009>

The following figure supplements are available for figure 4:

Figure supplement 1. Interaction of squares does not affect summation unidirectionally.

DOI: <https://doi.org/10.7554/eLife.43415.011>

Figure supplement 2. Input range expansion for observing nonlinear summation and divisive normalization.

DOI: <https://doi.org/10.7554/eLife.43415.010>

needed to be elaborated based on the observed response saturation with increasing input strength. Potential mechanisms for this could be nonlinear summation of excitation and inhibition at the soma (tested in **Figure 5**) and inhibitory delays (examined in **Figure 6**). In summary, we observed SDN as an outcome of integration of precisely balanced inputs in the CA3-CA1 network.

CA3 feedforward inhibition is necessary for SDN

We first verified our hypothesis that SDN results from feedforward inhibition in the CA3-CA1 network, and not from intrinsic properties of the CA1 neuron. We thus blocked inhibition and repeated the above experiment. We expected that SDN would be lost and linearity would be reinstated upon blocking inhibition.

We recorded responses of CA1 cells to our array of optical stimuli (**Figures 1d** and **5a**), then applied GABAzine to the bath and repeated the stimulus array (**Figure 5b**). We found that when inhibition was blocked, summation approached linearity (**Figure 5b,c**). We compared the scaling parameter γ of the divisive normalization model fit, for the above two conditions (**Equation (3)**). The values of γ were larger with inhibition blocked, indicative of approach to linearity (Wilcoxon rank-sum test, $p < 0.05$, $n = 8$ cells) (**Figure 5c**). While inhibition accounted in large part for the observed sublinear summation, the cells with inhibition blocked showed some residual sublinearity at high stimulus levels, which has been previously attributed to I_A conductance in CA1 neurons (**Cash and Yuste, 1999**). Based on the conductance equation (**Equation (5)**), leak conductance also contributes in part to the residual sublinearity (Supplementary **Equations (6-8)**). Thus, we confirmed that blocking inhibition reduced sublinearity, attenuating SDN.

Precise balance is also seen at resting membrane potential

Then, we hypothesised that the membrane potential change evoked by inhibitory synaptic currents could be increasing non-linearly with increasing CA3 input, even though the I/E ratio of conductances would be consistent across the range of input strengths. To address this, we compared responses to identical patterns before and after GABAzine application. For a given cell, for each pattern, we subtracted the initial control response with inhibition intact from the corresponding response with inhibition blocked. This gave us the inhibitory component or 'derived inhibition' for each stimulus pattern (**Figure 5d**, inset). We found that all stimuli to a cell evoked proportional excitation and inhibition even when recorded at resting potential (**Figure 5d,e**). Thus, we rejected our hypothesis of non-linear increase in inhibitory post-synaptic potential (IPSP) with excitatory post-synaptic potential at resting membrane potential (EPSP). Over the population, the median slope of the proportionality line was around 0.7, indicating that the EI balance was slightly tilted towards higher excitation than inhibition (**Figure 5f**). IPSP/EPSP ratios (**Figure 5f**) were smaller than IPSC/EPSC ratios (**Figure 2d**) due to proximity of inhibition to its reversal (~ -70 mV), than excitation to its reversal (~ 0 mV), at resting membrane potential (~ -65 mV). Overall, we saw precise balance in evoked excitatory and inhibitory synaptic potentials for >100 combinations per neuron.

Advancing inhibitory onset with increasing input explains SDN

We made a single compartment conductance model (**Figure 6—figure supplement 1a, Equation (5)**) to analyze the mechanism of SDN. We first show a Hodgkin-Huxley (HH) type single compartment model (Materials and methods), where we have used data from our voltage clamp recordings (**Figure 2**), as input to the model. Simulation with both excitation and inhibition produced curves resembling SDN, while only excitation gave a more linear response (**Figure 6a, Figure 6—figure supplement 2**), hence reproducing the observations depicted in **Figure 5**. Again, fit parameter γ was significantly higher for the cases without inhibition (**Figure 6—figure supplement 2**, Wilcoxon rank sum test, $p < 1e-4$, $n = 13$). In order to dissect the mechanism, we wanted to have finer control over synaptic input parameters like kinetics and EI delay.

With this in mind, we fit a function of difference of exponentials (Materials and methods) to our voltage clamp data to extract the peak amplitudes and kinetics of excitation and inhibition currents (Materials and methods). We used these and other parameters from literature (**Supplementary files 1 and 2**), and constrained the model to have EI balance, that is have maximum excitatory (g_{exc}) and inhibitory conductance (g_{inh}) proportional to each other, with a given I/E ratio. To test for SDN, we simulated our model in the range of experimentally determined I/E ratios, ranging from 1 to 6.

We observed that EI balance with static EI delay led to a slightly sublinear response which can be approximated with a divisive inhibition model (**Figure 6**). In contrast, subthreshold divisive normalization (SDN) implies progressively smaller changes in peak PSP amplitude with increase in excitatory input. We surmised that without changing EI balance, SDN should result if the inhibitory onset delays were an inverse function of the excitation (**Figure 6e, Equation (4)**). Hence, we simulated the model with dynamic delay, that is with values of inhibitory delay (δ_{inh}) varying as a decreasing function of the excitation.

$$\delta_{\text{inh}} = \delta_{\min} + me^{-kg_{\text{exc}}} \quad (4)$$

Here, δ_{\min} is the minimum synaptic delay between excitation and inhibition, k sets the steepness
94

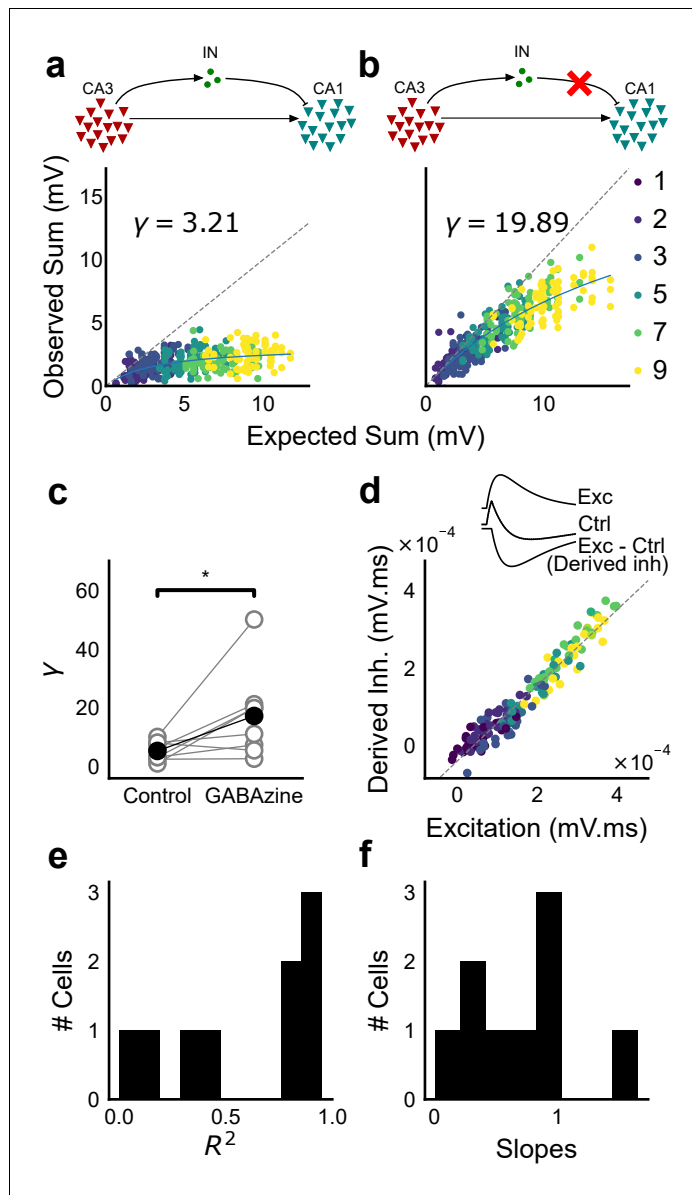


Figure 5. Blocking balanced inhibition at resting membrane potential attenuates SDN. (a) Top, schematic of experiment condition. Bottom, a cell showing divisive normalization in control condition. (b) Top, schematic of experiment condition with feedforward inhibition blocked (2 μ M GABAazine). Bottom, responses of the same cell with inhibition blocked. The responses are much closer to the linear summation line (dashed). The blue lines in a, b are the fits of the DN model. The value of γ of the fit increases when inhibition is blocked. (c) Parameter γ was larger with GABAazine in bath (Wilcoxon rank sum test, $p < 0.05$, $n = 8$ cells), implying reduction in normalization with inhibition blocked. (d) Excitation versus derived inhibition for all points for the cell shown in a (area under the curve) (Slope = 0.97, r^2 square = 0.93, x-intercept = 3.75e-5 mV.ms). Proportionality was seen for all responses at resting membrane potential. Top, ‘Derived inhibition’ was calculated by subtracting control PSP from the excitatory (GABAazine) PSP for each stimulus combination. (e,f) R^2 (median = 0.8) and slope values (median = 0.7) for all cells ($n = 8$ cells), showing tight IPSP/EPSP proportionality, and slightly more excitation than inhibition at resting membrane potentials.

DOI: <https://doi.org/10.7554/eLife.43415.012>

of the delay change with excitation, and m determines the maximum synaptic delay. In **Figure 6c**, we show that SDN emerged when we incorporated delays changing as a function of the total excitatory input to the model neuron.

We then tested this model prediction. From the EPSC and IPSC curves, we extracted excitatory and inhibitory onsets (Materials and methods), and subtracted the average inhibitory onsets from average excitatory onsets to get inhibitory delay (δ_{inh}) for each stimulus combination. We saw that δ_{inh} indeed varied inversely with total excitation (g_{exc}) (Figure 6f,g). Notably, the relationship of delay with conductance, with data from all cells pooled, seems to be a single inverse function, and might be a network property (Figure 6g, Figure 6—figure supplement 1d). The input-dependent change in inhibitory delay could be attributed to delayed spiking of interneurons with small excitatory inputs, and quicker firing with larger excitatory inputs. We further illustrate that this delay function emerges naturally by simply applying a threshold to the rising curve of an EPSP at an interneuron (Figure 6—figure supplement 1f). Thus, inhibition clamps down the rising EPSP at progressively earlier times, resulting in saturation of PSP amplitude when excitation is increased (Figure 6c,d, Figure 8). In Figure 8a and b, we show using a schematic, how SDN emerges when inhibitory onset changes as an inverse function of input strength.

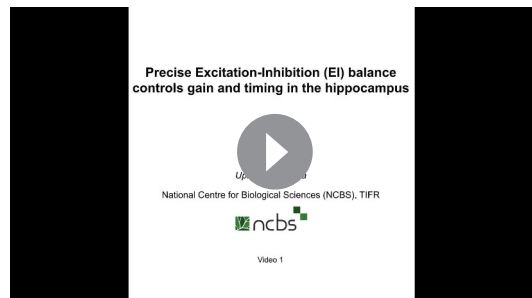
We observed that we were also able to capture the initial linear regime observed in Figure 4b by using the inverse relationship of delay with excitation in this conductance model. This can be understood as follows: at small excitatory input amplitudes, the EI delay is so large that inhibition arrives too late to affect the peak EPSP. At higher stimulus amplitudes the output response is now subjected to earlier, and hence increasingly effective inhibition, thus flattening the output curve (Appendix 1, Video 1, Figure 3—figure supplement 1a, Figure 6c).

We then tested if SDN required both EI balance and dynamic EI delay. We obtained values for balanced g_{inh} for each I/E ratio, and then shuffled the order of the balanced inhibitory vector with the excitation. This implied that the average I/E ratio was maintained over all stimuli, but not for individual stimuli. This shuffled set of inhibitory conductance with respect to excitation was used to calculate V_{max} (Figure 6—figure supplement 1b). Similarly, we obtained inhibitory delay (δ_{inh}) corresponding to each value of excitation from the dynamic delay curve in Equation (4) (Figure 6e). We then shuffled the order of delays, keeping excitation in the same order (Figure 6—figure supplement 1c). In both cases, SDN was strongly attenuated, implying that both EI balance and inverse scaling of inhibitory delay were necessary for SDN (Figure 6—figure supplement 1b,c, Supplementary Equation (6) to (8)). Further, we transformed the membrane current equation (Equation (5)) into the form which resembles divisive normalization equation (Appendix 1), and saw that in this form, γ depends on the intrinsic properties of the neuron, and is modulated by delays and EI ratios.

Thus, our analysis of a conductance model suggests that SDN could be a general property of balanced feedforward networks, due to two characteristic features: EI balance and inhibitory kinetics. Each of these variables may be subject to plasticity and modulation to attain different amounts of normalization (Figure 8c,d, Figure 8—figure supplement 1).

Stimulus information is encoded both in amplitude and time

We next asked if the temporally advancing inhibition (Figure 6e-h) affected PSP peak time with increase in stimulus strength. We calculated the



Video 1. Subthreshold divisive normalization emerges when onset delay of balanced inhibition dynamically decreases with excitation. (a) Schematic of the model of a single compartment neuron, which receives excitatory stimulus (in blue) at 20 ms, followed by an inhibitory stimulus (in orange) with variable onset delays. (b) Excitatory conductance (gluGbar) changes as shown in top most slider. Inhibitory conductance (I/E ratio*gluGbar) arrives after a dynamic or static delay. The orange and the blue dotted lines track the inhibition onset and the excitation peak, respectively. Their interaction point, marked by the orange dot, traces the relationship of excitatory conductance with dynamic or static delay. (c) EI summation plot (Figures 3d and 4b) of PSP peak against excitation. Model shows SDN with dynamic EI delays, characterized by the initial linear zone followed by a sublinear zone for higher excitation values. SDN was lost when the EI delay was static. (d) Membrane voltage change as a result of only excitatory (dotted line), and integration of excitatory and inhibitory conductances (solid line) from panel b. Note how the peak time changes as a function of delays.

DOI: <https://doi.org/10.7554/eLife.43415.020>

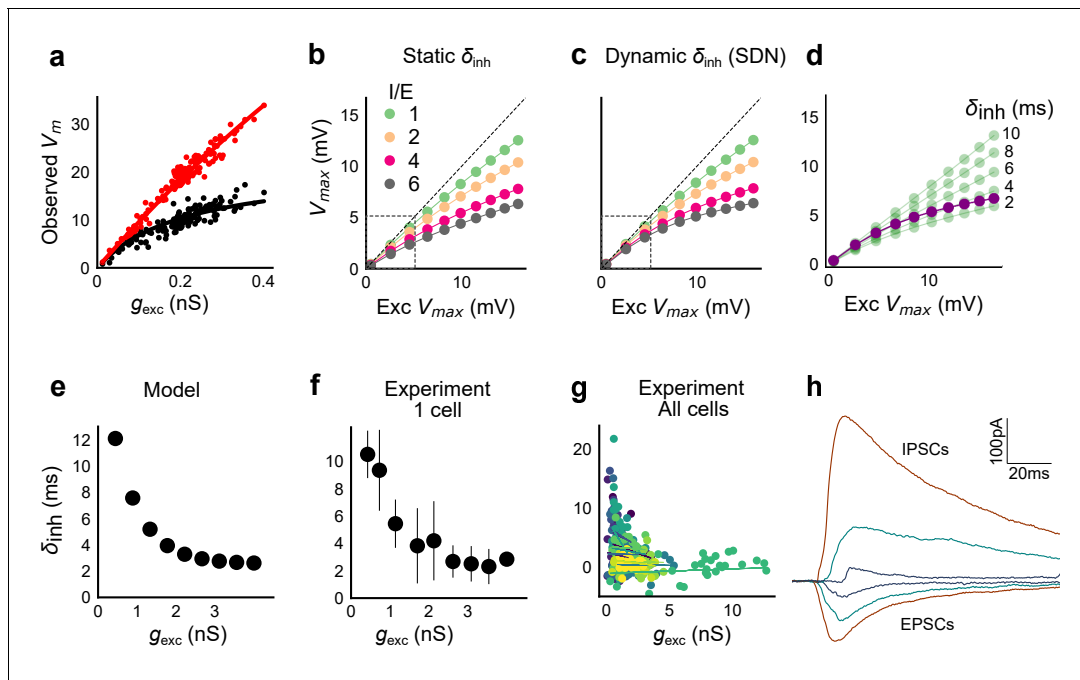


Figure 6. Conductance model predicts Excitatory-Inhibitory delay as an important parameter for divisive normalization. (a) Subthreshold responses from HH model, simulated with traces recorded from one voltage clamped cell (**Figure 2**). Non-linearly saturating curve, similar to SDN, obtained by simulating with both excitation and inhibition synaptic conductances (black), while the response profile is much more linear with only excitation (red). Each black point is the median response of an excitation trace paired with six different repeats of inhibition for that combination. (b) PSP peak amplitude with both excitatory and balanced inhibitory inputs is plotted against the EPSP peak amplitude with only excitatory input. Model showed sublinear behaviour approximating divisive inhibition for I/E proportionality ranging from 1 to 6 when the inhibitory delay was static. Different colours show I/E ratios. (c) Same as in b, except the inhibitory delay was varied inversely with excitatory conductance (as shown in e). Initial linear zone and diminishing changes in PSP amplitude, indicative of SDN were observed, and the normalization gain was sensitive to the I/E ratio. $\delta_{\min} = 2$ ms, $k = 0.5$ nS $^{-1}$, and $m = 8.15$ ms. Note, the increased overlap in the initial zone (grey box) and the saturation of the PSP peaks in c, as compared to b. (d) Effect of changing EI delay, keeping I/E ratio constant (I/E ratio = 5). Divisive inhibition (green) seen while changing EI delay values from 2 to 10 ms. Divisive normalization (purple) emerges if delays are changed as shown in e. $\delta_{\min} = 2$ ms, $k = 0.5$ nS $^{-1}$, and $m = 8.15$ ms. (e) Inverse relationship of EI delays with excitation. Inhibitory delay was varied with excitatory conductance in **Equation (4)** with $\delta_{\min} = 2$ ms, $k = 2$ nS $^{-1}$, and $m = 13$ ms. (f) Data from an example cell showing the relationship of EI delays with excitation. The relationship is similar to the prediction in e. Points are binned averages. Error bars are s.d. (g) Data from all cells showing delay as a function of excitation. Different colors indicate different cells ($n = 13$ cells). Grey lines are linear regression lines through individual cells. (h) Traces (from a voltage clamped neuron) showing the decreasing EI delay with increasing amplitude of PSCs. Each trace is an average of 6 repeats.

DOI: <https://doi.org/10.7554/eLife.43415.013>

The following figure supplements are available for figure 6:

Figure supplement 1. Sensitivity of SDN to EI balance and EI delay, and synaptic time courses used for model.

DOI: <https://doi.org/10.7554/eLife.43415.014>

Figure supplement 2. HH model simulations with voltage clamped data show SDN.

DOI: <https://doi.org/10.7554/eLife.43415.015>

slope of the PSP peak times against the expected axis in the presence (Control) and absence of inhibition (GABAazine) for a given cell. If inhibition cut into excitation and resulted in advancing of peak times with increasing stimulus strength, the slope of peak times would be negative, as shown in **Figure 7a**. Conversely, when inhibition is blocked, slope of peak times is not expected to change much. We saw that for all cells, slope of the peak time with inhibition intact was lower than the slope in the case with inhibition blocked (**Figure 7b**) (Wilcoxon Rank sum test ($p=0.006$), $n = 8$ cells).

What does SDN mean for information transmission in balanced networks? While SDN allowed the cell to integrate a large range of inputs before reaching spiking threshold, it also resulted in diminishing changes in PSP peaks at larger inputs (**Figure 4b**). This implied that information about the input was partially ‘lost’ from the PSP amplitude. However, PSP times to peak became shorter (**Figure 7a,b**), hence potentially encoding some information about the input in this time variable

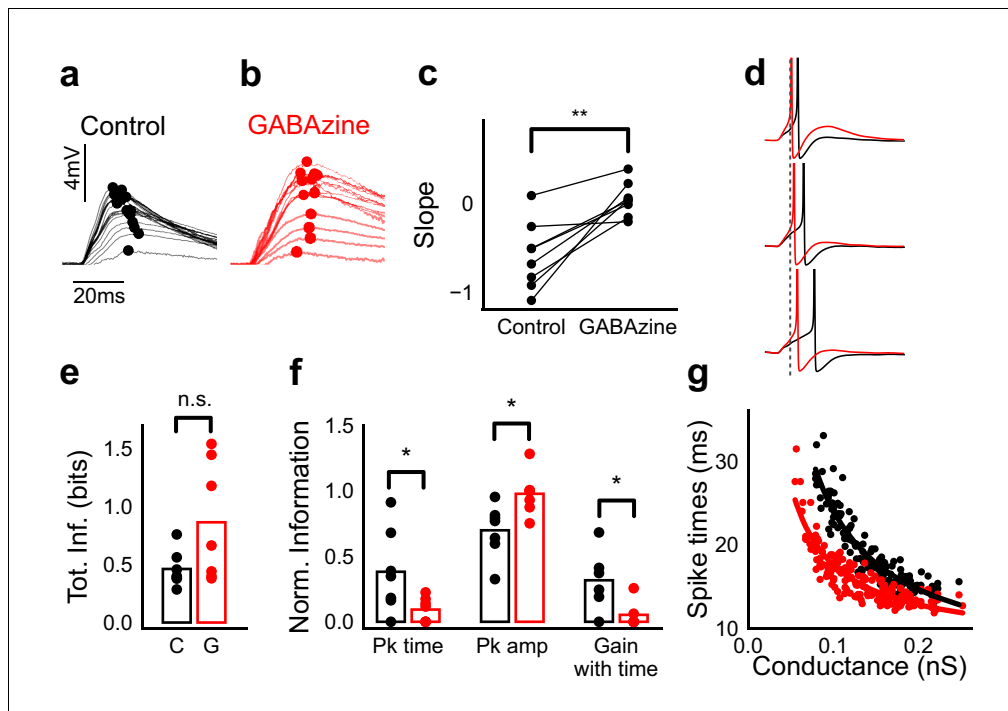


Figure 7. Advancing inhibitory onset changes PSP peak time and spike time with increase in stimulus strength. (a,b) The PSP peak arrived earlier following larger input in the control case (black), but not with GABAazine in bath (red). Traces for an example cell, binned (20 bins for Expected sum axis) and averaged, for control (black) and with GABAazine in bath (red). (c) Slope of the peak time was more negative in presence of inhibition (control) than when inhibition was blocked (GABAazine) ($n = 8$ cells). (d) Three example traces from the cell in g showing the relationship of spikes in presence (black) and absence of inhibition (red). Spikes were produced by HH model, using synaptic conductances from voltage clamp data. The separation between spike times of the two conditions increased with decrease in input conductance (top to bottom). (e) Total mutual information of peak amplitude and peak timing with expected sum was not significantly different between Control and GABAazine case (Wilcoxon Rank sum test (<0.05), $p=0.11$, $n = 7$ CA1 cells). (f) Normalized mutual information between Expected V_m and peak time, Expected V_m and peak amplitude, and conditional mutual information between Expected V_m and peak time, given the knowledge of peak amplitude. Normalized information was calculated by dividing mutual information by total information for each cell (as shown in d). Peak times carried more information in the presence of inhibition, and peak amplitudes carried more information in the absence of inhibition. There was higher gain in information about the input with timing if the inhibition was kept intact (Wilcoxon Rank sum test ($p<0.05$), $n = 7$ (Pk time, Pk amp) and ($p=0.05$) $n = 6$ (Gain with time) CA1 cells). (g) Relationship of spike time with excitatory conductance, in the presence (black) and absence of inhibition (red), for HH model simulations. All black points are medians of spikes of each excitation trace paired with six different repeats of inhibition for that combination.

DOI: <https://doi.org/10.7554/eLife.43415.016>

The following figure supplement is available for figure 7:

Figure supplement 1. Spike time changes with increasing input are steeper in presence of inhibition.

DOI: <https://doi.org/10.7554/eLife.43415.017>

(**Figure 7f, Figure 8b**). In contrast, while the peak amplitudes seen with GABAazine predicted the input more reliably, peak times of EPSPs did not change much with input (**Figure 7b,f**). Thus, PSP peak time may carry additional information about stimulus strength, when EI balance is maintained.

We quantified this using an information theoretical framework (**Shannon, 1948**). We took linear sum of 1-square PSP peak amplitudes (Expected sum), as a proxy for input strength. We then calculated the mutual information between Expected sum and PSP peak amplitudes of the corresponding N-squares, and between Expected sum and PSP peak timing (Materials and methods). Using this, we asked, how is the information about the input divided between PSP peak amplitude and timing? The total mutual information of both peak amplitude and peak timing with expected sum was slightly lesser in the presence of inhibition, but this difference was statistically not significant (**Figure 7e**) (Wilcoxon Rank sum test (<0.05), $p=0.11$, $n = 7$ cells). We found that peak timing had more information in presence of inhibition (control), and peak amplitude had more information in absence of inhibition (GABAazine) (Wilcoxon Rank sum test (<0.05), $n = 7$ cells) (**Figure 7f**). Further, we asked, how better can we predict the input, with the knowledge of peak timing, when

the peak amplitude is already known? We found that in the presence of inhibition, peak amplitude carried only a part of the total information about the input, and further knowledge of peak time substantially increased the total information. In contrast, in the absence of inhibition, peak amplitude carried most of the information about input, and there was very little gain in information with the knowledge of peak times (**Figure 7f**) (Wilcoxon Rank sum test (=0.05), n = 6 cells).

We then asked if the PSP peak time changes are also reflected in spike times. Since most of our stimuli elicited subthreshold responses, studying spiking required an artificial depolarization stimulus. From simulations we found that several parameters of the model (including resting membrane potential, membrane capacitance, synaptic conductances, EI ratio and delay, and spike threshold) could affect the mapping of subthreshold responses to spike timing, suggesting that this is a rich substrate for modulation. Keeping this caveat in mind, we tested the temporal profile of spikes with our model. We let the model cell spike in response to EI (similar to the Control condition) and only E (Gabazine condition). We observed that SDN translated to the spiking domain by encoding stronger stimulus amplitudes as shorter spike latencies, similar to the subthreshold responses. The presence of inhibition decreased the steepness of spike time with conductance (**Figure 7d,g**, **Figure 7—figure supplement 1**). The separation between the two conditions was sensitive to the exact value of threshold. At threshold close to resting potential, the separation was low, because the cell spiked before the effect of inhibition set in. For a given threshold, a subset of the cells showed enough separation between conditions (**Figure 7d,g**, **Figure 7—figure supplement 1**) and this value could be tuned to obtain maximum separation for each cell.

Overall, these results suggest that with inhibition intact, input information is shared between amplitude and time, and knowledge of peak time and amplitude together contains more information about input than either of them alone.

Modulation of gating with SDN

We next asked how the two basic parameters - I/E ratio and EI delay - modulated the degree of normalization and kinetics of the SDN curve (**Figure 8c,d**). Using our conductance model, we measured the normalization parameter γ ($\alpha = 0$, $\beta = 1$, **Equation (1)**) for a range of values of I/E ratio and delays, and found that normalization increased systematically with increase in I/E ratio as well as with increase in the steepness of the EI delay relationship (**Figure 8c**). This implies that the degree of normalization of not only an entire neuron, but subsets of inputs to a neuron, could be dynamically altered by changing these parameters. In terms of gating, for a neuron with all inputs tightly balanced, any subset of inputs with reduction in I/E ratio will be gated 'on', corresponding to a condition of higher γ . Neurons can thus differentially gate and respond to specific inputs, while still retaining the capacity to respond to other input combinations.

Discussion

This study describes two fundamental properties of the CA3-CA1 feedforward circuit: balanced excitation and inhibition from arbitrary presynaptic CA3 subsets, and an inverse relationship of excitatory-inhibitory delays with CA3 input amplitude. We used optogenetic photostimulation of CA3 with hundreds of unique stimulus combinations and observed precise EI balance at individual CA1 neurons for every input combination. Stronger stimuli from CA3 led to proportional increase in excitatory and inhibitory amplitudes at CA1, and a decrease in the delay with which inhibition arrived. Consequently, larger CA3 inputs had shorter inhibitory delays, which led to progressively smaller changes in CA1 membrane potential. We term this gain control mechanism Subthreshold Divisive Normalization (SDN). This reduction in inhibitory delay with stronger inputs contributes to a division of input strength coding between PSP amplitude and PSP timing.

Precise balance in the hippocampus

Our findings demonstrate that precise EI balance is maintained by arbitrary combinations of neurons in the presynaptic network, despite the reduced nature of the slice preparation, with no intrinsic network dynamics. This reveals exceptional structure in the connectivity of the network. Theoretical analyses suggest that networks can achieve detailed balance with inhibitory Spike Timing Dependent Plasticity (iSTDP) rules (**Hennequin et al., 2017; Luz and Shamir, 2012; Vogels et al., 2011**). Such an iSTDP rule has been observed in the auditory cortex (**D'amour and Froemke, 2015**). Given that

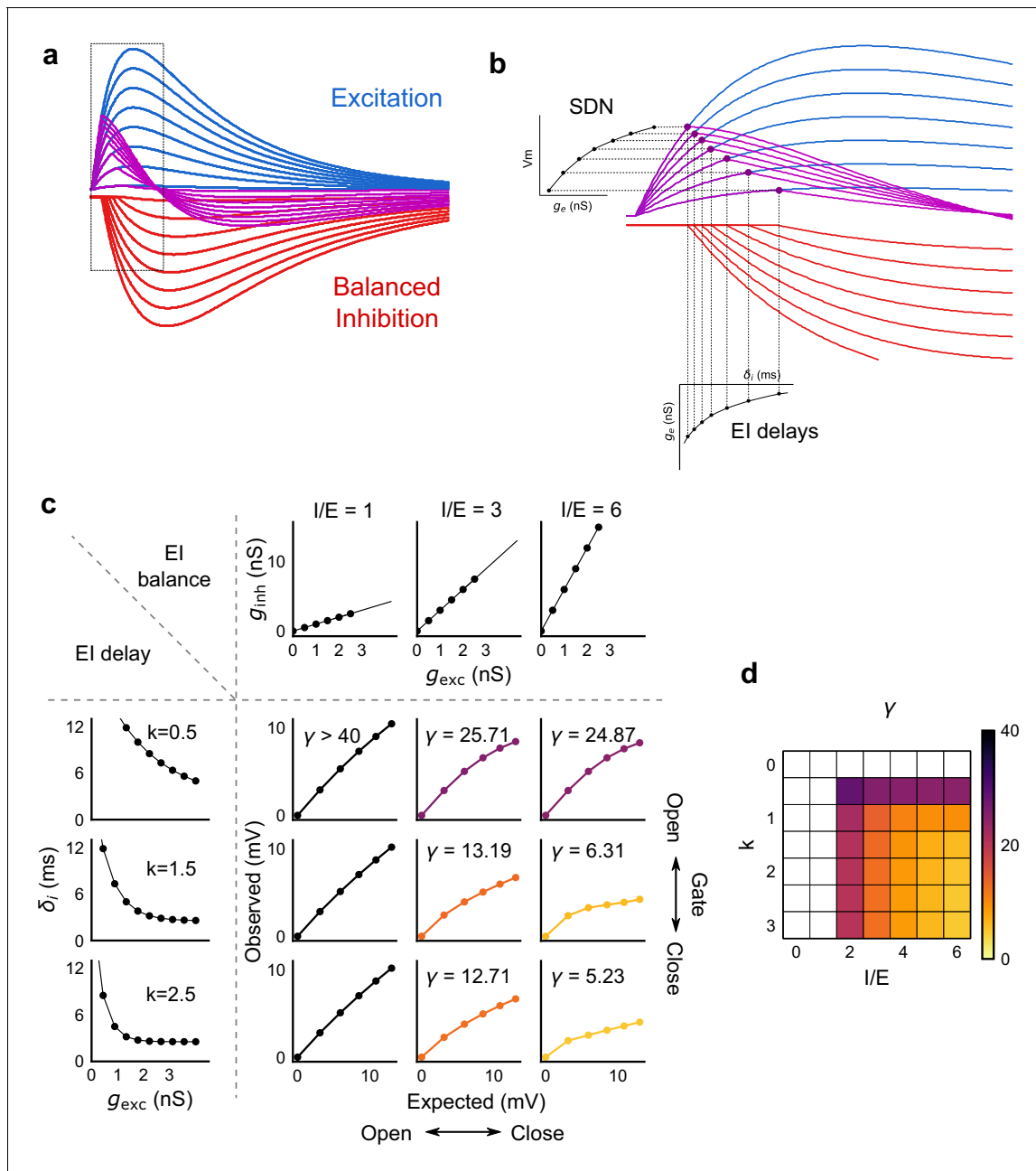


Figure 8. Emergence of SDN from balanced excitation and inhibition, coupled with dynamic EI delays. (a) Schematic showing precisely balanced EPSPs (blue) and corresponding IPSPs (red) summing to produce PSPs (purple). The EPSPs and IPSPs increase in equal input steps. (b) Zooming into the portion in the rectangle in a. Excitation onset is constant, but inhibition onset changes as an inverse function of input or conductance (g_{exc}), as shown in Figure 6. With increasing input, inhibition arrives earlier and cuts into excitation earlier for each input step. This results in smaller differences in excitatory peaks with each input step, resulting in SDN. The timing of PSP peaks (purple) becomes progressively advanced, whereas the timing of EPSP peaks (blue) does not, consistent with our results in Figure 7. (c,d) Normalization as a function of the two building blocks – El balance (I/E ratio) and El delays (interneuron recruitment kinetics, k , as predicted by the model. Larger values of both imply greater normalization and increased gating. Colors of the SDN curves depict the value of gamma (γ), as shown in the phase plot in d. White squares are values of γ larger than 40, where almost no normalization occurs.

DOI: <https://doi.org/10.7554/eLife.43415.018>

The following figure supplement is available for figure 8:

Figure supplement 1. PSP traces showing the effect of I/E ratio and inhibitory recruitment kinetics (k) on SDN.

DOI: <https://doi.org/10.7554/eLife.43415.019>

balance needs to be actively maintained (Xue et al., 2014), we suspect that similar plasticity rules (Hennequin et al., 2017) may also exist in the hippocampus.

Precisely balanced networks, with all input subsets balanced, are well suited for input gating (Barron et al., 2017; Hennequin et al., 2017). The finding that most silent CA1 cells can be converted to place cells for arbitrary locations predicts the existence of an input gating mechanism (Lee et al., 2012), but the nature of this mechanism remains unknown. One prediction of precise balance is that inputs for multiple potential place fields may be balanced, and hence place field activity is gated ‘off’. Evoked depolarizations (Lee et al., 2012) or dendritic plateau potentials (Bittner et al., 2015; Bittner et al., 2017), which potentiate the subset of active synapses, that is, change the I/E ratio (Grienberger et al., 2017), can flip the gate ‘on’, thereby converting a silent cell to a place cell for that specific place field. This reasoning corroborates the observation of homogenous inhibition suppressing out-of-field heterogeneously tuned excitation (Grienberger et al., 2017), while providing a finer, synaptic scale view of the gating mechanism.

El delays and temporal coding

In several El networks in the brain, inhibition is known to suppress excitation after a short time delay, leaving a ‘window of opportunity’ for spiking to occur (Higley and Contreras, 2006; Pouille and Scanziani, 2001; Wehr and Zador, 2003). We have shown that balanced inhibitory input arrives with a delay modulated by the excitatory input in a feedforward circuit. This inverse relationship of El delay with excitation has not been explicitly shown, although Heiss et al. (2008) report a decrease in El delays with increase in whisker stimulation speed in layer 4 cells. We show that modulation of El delay by excitation helps encode the input information in both amplitude and timing of the PSP (Figure 7). Thus, large inputs could be represented with fewer spikes, while conserving input strength information in spike timing. In CA1, a classic example of such dual coding is theta phase precession (Jensen and Lisman, 2000). In addition, spike times during sharp wave ripples, gamma oscillations and time cell representations are also precise up to ~10 ms, which is the range of the dynamic ‘window of opportunity’ we observe. This dynamic window also implies that the neuron can transition from temporal integration mode at small input amplitudes to coincidence detection at large input amplitudes (Gabernet et al., 2005; Higley and Contreras, 2006; Wehr and Zador, 2003). Consistent with this range of spike-coding transformations, our simulations suggest that the precise mapping of subthreshold summation to spike timing can be effectively modulated by several cellular parameters as well as by details of input activity (Figure 7d,g).

Subthreshold Divisive Normalization (SDN): a novel gain control mechanism

We have introduced Subthreshold Divisive normalization (SDN) as a novel gain control mechanism arising from El balance and dynamic El delays. Our study was uniquely able to observe SDN because of the large range of inputs possible (Poirazi et al., 2003) using patterned optical stimulation. While we observed no unidirectional correlation of the distance between input spots and their responses for most inputs (Figure 4—figure supplement 1), a limitation of this stimulation design is that some of the inputs may not be fully independent due physical proximity of stimulus spots. SDN expands the dynamic range of inputs that a neuron can accommodate before reaching spike threshold (Figure 8—figure supplement 1b). This is particularly useful for temporally coding, sparsely spiking neurons like CA1 (Ahmed and Mehta, 2009). So far, analogous gain control by divisive normalization has only been observed for firing rates of neurons (Carandini and Heeger, 2011). This implies that the timescales of gain change in DN are averaged over periods of tens of milliseconds, over which rates change. As opposed to this, in SDN, gain of every input is normalized at synaptic (millisecond) timescales. Our results add a layer of subthreshold gain control in single neurons, to the known suprathreshold gain control at the population level in CA1 (Pouille et al., 2009). This two-step gain control implies that the dynamic range of the population may be wider than previously estimated. While most experimental observations of firing rate gain change have been explained by the phenomenological divisive normalization equation, the mechanistic basis for normalization has been unclear. SDN provides a biophysical explanation for phenomenological divisive normalization by connecting El ratios and delays with gain control.

I/E ratio can be changed by neuromodulation (Froemke, 2015; Froemke et al., 2007), by short term plasticity mechanisms (Bartley and Dobrunz, 2015; Klyachko and Stevens, 2006; Tsodyks and Markram, 1997) and by disinhibition (Basu et al., 2016). Although we show that EI delays are input amplitude dependent, they may also be modulated by external signals, or behavioural states such as attention (Kim et al., 2016) (Figure 8c,d). Such interneuron recruitment based changes have been shown to exist in thalamocortical neurons (Gabernet et al., 2005). Dynamic regulation of EI delay has been theoretically explored in balanced networks (Bruno, 2011; Kremkow et al., 2010) for temporal gating of transient inputs independently by amplitude and time. Thus, temporal gating by EI delays (Kremkow et al., 2010), combined with the amplitude gating by detailed balance (Vogels and Abbott, 2009) could be a powerful mechanism for gating signals (Kremkow et al., 2010) in the hippocampal feedforward microcircuit.

Several studies point toward the existence of precise EI balance in the cortex (Atallah and Scanziani, 2009; Okun and Lampl, 2008; Wehr and Zador, 2003; Wilent and Contreras, 2005; Zhang et al., 2003; Zhou et al., 2014), and here we have shown it in the hippocampus. We propose that input strength dependent inhibitory delay change may be a general property of feedforward network motifs. Together, these suggest that precisely balanced feedforward networks are elegantly suited for controlling gain, timing and gating at individual neurons in neural circuits.

Materials and methods

Key resources table

Reagent type (species) or resource	Designation	Source or reference	Identifiers	Additional information
Genetic reagent (<i>M. musculus</i>)	C57BL/6-Tg (Grik4-cre) G32-4St/J	Jackson Laboratory	Stock #: 006474	Dr. Susumu Tonegawa's laboratory, MIT
Strain, strain background (Adeno- associated virus)	AAV5.CAGGS.Flex. ChR2-tdTomato. WPRE.SV40	Penn Vector Core		
Software, algorithm	MOOSE simulator	Ray and Bhalla, 2008	RRID:SCR_008031	Dr. Upinder Bhalla's laboratory, NCBS

Animals

All experimental procedures were approved by the National Centre for Biological Sciences Institutional Animal Ethics Committee (Protocol number USB-19-1/2011), in accordance with the guidelines of the Government of India (animal facility CPCSEA registration number 109/1999/CPCSEA) and equivalent guidelines of the Society for Neuroscience. CA3-cre (C57BL/6-Tg (Grik4-cre) G32-4St/J mice, Stock number 006474) were obtained from Jackson Laboratories. The animals were housed in a temperature controlled environment with a 14 hr light: 10 hr dark cycle, with *ad libitum* food and water.

Virus injections

21–30 days old male transgenic mice were injected with Lox-ChR2 (AAV5.CAGGS.Flex.ChR2-tdTomato.WPRE.SV40) virus obtained from University of Pennsylvania Vector Core. Injection coordinates used were –2.0 mm RC, ±1.9 mm ML, –1.5 mm DV. ~300–400 nl solution was injected into the CA3 region of left or right hemisphere with brief pressure pulses using Picospritzer-III (Parker-Hannifin, Cleveland, OH). Animals were allowed to recover for at least 4 weeks following surgery.

Slice preparation

8–12 week (4–8 weeks post virus injection) old mice were anesthetized with halothane and decapitated post cervical dislocation. Hippocampus was dissected out and 350 um thick transverse slices were prepared. Slices (350 microns) were cut in ice-cold high sucrose ASCF containing (in mM): 87 NaCl, 2.5 KCl, 1.25 NaH₂PO₄, 25 NaHCO₃, 75 sucrose, 10 glucose, 0.5 CaCl₂, 7 MgCl₂. Slices were

stored in a holding chamber, in artificial cerebro-spinal fluid (aCSF) containing (in mM) - 124 NaCl, 2.7 KCl, 2 CaCl₂, 1.3 MgCl₂, 0.4 NaH₂PO₄, 26 NaHCO₃, and 10 glucose, saturated with 95% O₂/5% CO₂. After at least an hour of incubation, the slices were transferred to a recording chamber and perfused with aCSF at room temperature.

Electrophysiology

Whole cell recording pipettes of 2-5MO were pulled from thick-walled borosilicate glass on a P-97 Flaming/Brown micropipette puller (Sutter Instrument, Novato, CA). Pipettes were filled with internal solution containing (in mM): 130 K-gluconate, 5 NaCl, 10 HEPES, 1 EGTA, 2 MgCl₂, 2 Mg-ATP, 0.5 Na-GTP and 10 Phosphocreatinine, pH adjusted to 7.3, osmolarity ~285 mOsm. The membrane potential of CA1 cells was maintained near -65 mV, with current injection, if necessary. GABA-A currents were blocked with GABAazine (SR-95531, Sigma) at 2 uM concentration for some experiments. Cells were excluded from analysis if the input resistance changed by more than 25% (measured for 15/39 cells) or if membrane voltage changed more than 2.5 mV (measured for 39/39 cells, maximum current injected to hold the cell at the same voltage was ±15 pA) of the initial value. For voltage clamp recordings, the K-gluconate was replaced by equal concentration Cs-gluconate. Cells were voltage clamped at 0 mV (close to calculated excitation reversal) and -70 mV (calculated inhibition reversal) for IPSC and EPSC recordings respectively. At 0 mV a small component of APV sensitive inward current was observed, and was not blocked during recordings. Cells were excluded if series resistance went above 25MO or if it changed more than 30% of the initial value, with mean series resistance being 15.7MO ± 4.5 MO s.d. (n = 13). For CA3 current clamp recordings, the cells were excluded if the V_m changed by 5 mV of the initial value. For whole-cell recordings, neurons were visualized using infrared microscopy and differential interference contrast (DIC) optics on an upright Olympus BX61WI microscope (Olympus, Japan) fitted with a 40X (Olympus LUMPLFLN, 40XW), 0.8NA water immersion objective. Recordings were acquired on a HEKA EPC10 double plus amplifier (HEKA Electronik, Germany) and filtered 2.9 kHz and digitized at 20 kHz.

Optical stimulation setup

Optical stimulation was done using DMD (Digital Micromirror Device) based Optoma W316 projector (60 Hz refresh rate) with its color wheel removed. Image from the projector was miniaturized using a Nikon 50 mm f/1.4D lens and formed at the focal plane of the tube lens, confocal to the sample plane. The white light from the projector was filtered using a blue filter (Edmund Optics, 52532), reflected off of a dichroic mirror (Q495LP, Chroma), integrated into the light path of the Olympus microscope, and focused on sample through a 40X objective. This arrangement covered a circular field of around 200 micron diameter on sample. 2.5 pixels measured one micron at sample through the 40X objective. Light intensity, measured using a power meter, was about 15 mW/mm² at sample surface. Background light from black screen usually elicited no or very little synaptic response at recorded CA1 cells. A shutter (NS15B, Uniblitz) was present in the optical path to prevent the slice from being stimulated by background light during the inter-trial interval. The shutter was used to deliver stimulus of 10–15 ms per trial. A photodiode was placed in the optical path after the shutter to record timestamps of the delivered stimuli.

Patterned optical stimulation

Processing 2 was used for generating optical patterns. All stimuli were 16 micron squares sub-sampled from a grid. 16 micron was chosen since it is close to the size of a CA3 soma. The light intensity and square size were standardized to elicit typically one spike per cell per stimulus. The number of spikes varied to some extent based on the expression of ChR2, which varied from cell to cell. The switching of spots from one trial to next, at 3 s inter trial interval, prevented desensitization of ChR2 over successive trials (**Figure 1g**).

For a patched CA1 cell, the number of connected CA3 neurons stimulated per spot was estimated to be in the range of 0 to a maximum of 50 for responses ranging from 0 to 2 mV. These calculations assume a contribution of 0.2 mV per synapse (**Magee and Cook, 2000**) and release probability of ~0.2 (**Murthy et al., 1997**). This number includes responses from passing axons, which could also get stimulated in our preparation.

We did not observe any significant cross stimulation of CA1 cells. CA1 cells were patched and the objective was shifted to the CA3 region of the slice, where the optical patterns were then projected. CA1 cells showed no response to optical stimulation because (i) Use of CA3-cre line restricted ChR2 to CA3 cells, (ii) physical shifting of the objective away from CA1 also made sure that any leaky expression, if present, did not elicit responses. Using a cre-based targeted optogenetic stimulation combined with patterned optical stimulation, we designed an experiment which was both more specific and more effective at exploring a large stimulus space. Unlike electrical stimulation, optical stimulation specifically excited CA3 pyramidal neurons, and hence the recorded inhibition was largely feedforward. We believe this specificity was crucial to the finding that I/E ratios for all stimuli to a cell are conserved. Electrical stimulation does not distinguish between neuronal subclasses, and in particular fails to separate out the inhibitory interneurons. Since a key part of our findings emerged from being able to establish a temporal sequence of activation of interneurons, it was crucial to exclude monosynaptic stimulation of interneurons in the experimental design. Second, patterned optical stimulation allowed us to explore a grid of 225 stimulus points in CA3, thereby obtaining a wide array of stimulus combination with large dynamic range, without compromising on the specificity of stimulation (*Figure 1, Figure 1—figure supplement 1*).

We used four different stimulus grids (*Figure 1—figure supplement 1*). All squares from a grid were presented individually (in random order) and in a stimulus set - randomly chosen combinations of 2, 3, 5, 7, or 9, with 2, 3 or 6 repeats of each combination. The order of presentation of a given N square combination was randomized from cell to cell.

Data analysis and code availability

All analyses were done using custom written software in Python 2.7.12 (numpy, scipy, matplotlib and other free libraries) and MatlabR2012b. All error bars are standard deviations. All analysis codes are available as a free library at (<https://github.com/sahilm89/linearity>; copy archived at <https://github.com/elifeiences-publications/linearity>).

Pre-processing

PSPs and PSCs were filtered using a low-pass Bessel filter at 2 kHz, and baseline normalized using 100 ms before the optical stimulation time as the baseline period. Period of interest was marked as 100 ms from the beginning of optical stimulation, as it was the typical timescales of PSPs. Timing of optical stimulation was determined using timestamp from a photodiode responding to the light from the projector. Trials were flagged if the PSP in the interest period were indistinguishable from baseline period due to high noise, using a two sample KS test ($p\text{-value} < 0.05$). Similarly, action potentials in the interest period were flagged and not analyzed, unless specifically mentioned.

Feature extraction

A total of four measures were used for analyzing PSPs and PSCs (*Figure 3c*). These were mean, area under the curve, average and area to peak. This was done to be able to catch differences in integration at different timescales, as suggested by *Poirazi et al. (2003)*. Trials from CA1 were mapped back to the grid locations of CA3 stimulation for comparison of Expected and Observed responses. Grid coordinate-wise features were calculated by averaging all trials for a given grid coordinate.

Subthreshold divisive normalization model

Different models of synaptic integration: Subtractive Inhibition, Divisive Inhibition, and Divisive Normalization models were obtained by constraining parameters in *Equation (1)*. The models were then fit to the current clamp dataset using lmfit. Reduced chi-squares (*Figure 4—figure supplement 2o*) and Bayesian Information Criterion (*Figure 4c*) were used to evaluate the goodness of fits of these models to experimental data.

Single-compartment model

A single-compartment conductance-based model was created in Python using sympy and numpy. The model consisted of leak, excitatory and inhibitory synaptic conductances (*Equation (5), Figure 6—figure supplement 1a*) to model the subthreshold responses by the CA1 neurons.

$$C_m \frac{dV_m}{dt} = g_{\text{leak}}(V_m - E_{\text{leak}}) + g_{\text{exc}}(V_m - E_{\text{exc}}) + g_{\text{inh}}(V_m - E_{\text{inh}}) \quad (5)$$

The parameters used for the model were taken directly from data, or literature (**Supplementary file 2**). The synaptic conductances $g_{\text{exc}}(t)$, and $g_{\text{inh}}(t)$ were modeled as difference of exponentials (**Equations (6) and (7)**):

$$g_{\text{exc}}(t) = \bar{g}_{\text{exc}} \left(\frac{e^{\left(\frac{-t}{\tau_{\text{decay}}}\right)} - e^{\left(\frac{-t}{\tau_{\text{rise}}}\right)}}{-\left(\frac{\tau_{\text{rise}}}{\tau_{\text{decay}}}\right)^{\frac{\tau_{\text{decay}} - \tau_{\text{rise}}}{\tau_{\text{decay}} - \tau_{\text{rise}}}} + \left(\frac{\tau_{\text{rise}}}{\tau_{\text{decay}}}\right)^{\frac{\tau_{\text{decay}} - \tau_{\text{rise}}}{\tau_{\text{decay}} - \tau_{\text{rise}}}}} \right) \quad (6)$$

$$g_{\text{inh}}(t) = \bar{g}_{\text{inh}} \left(\frac{e^{\left(\frac{\delta_{\text{inh}} - t}{\tau_{\text{decay}}}\right)} - e^{\left(\frac{\delta_{\text{inh}} - t}{\tau_{\text{rise}}}\right)}}{-\left(\frac{\tau_{\text{rise}}}{\tau_{\text{decay}}}\right)^{\frac{\tau_{\text{decay}} - \tau_{\text{rise}}}{\tau_{\text{decay}} - \tau_{\text{rise}}}} + \left(\frac{\tau_{\text{rise}}}{\tau_{\text{decay}}}\right)^{\frac{\tau_{\text{decay}} - \tau_{\text{rise}}}{\tau_{\text{decay}} - \tau_{\text{rise}}}}} \right) \quad (7)$$

For the divisive normalization case, the inhibitory delays (δ_{inh}) were modeled to be an inverse function of $g_{\text{exc}}(t)$ (**Equation (4)**). In other cases, they were assumed to be constant and values were taken from **Supplementary file 2**.

HH-based single-compartment model

A single-compartment Hodgkin Huxley model with parameters mentioned in **Supplementary file 3** was simulated in MOOSE (*Ray and Bhalla, 2008*) to analyze how measured synaptic conductances sum to cause CA1 somatic depolarization. To enable spiking, we included sodium and potassium delayed rectifier (KDR) channels in these neurons. Then, we drove this neuron with synaptic input as measured from voltage clamp data.

Measurement of synaptic conductances

We calculated excitatory and inhibitory conductances using **Equation (5)**, while holding the neuron at inhibitory and excitatory reversal potentials respectively (*Zhou et al., 2014, Atallah and Scanziani, 2009*). To measure excitatory conductance (g_{exc}), we clamped the membrane to the inhibitory reversal potential (E_{inh}). In the absence of a stimulus, the holding current gave us the value of leak current (I_{leak}). Excitatory synaptic current (I_{exc}) was measured as the change in membrane current evoked by the input stimulus ($I_m - I_{\text{leak}}$), from the baseline of holding current. We calculated the g_{exc} by dividing this stimulus evoked excitatory current by the excitatory driving force ($V_m - E_{\text{exc}}$). The same procedure was repeated at excitatory reversal to measure inhibitory conductance (g_{inh}) for each stimulus.

With this method, measurement of g_{exc} and g_{inh} at corresponding clamped membrane voltages was independent of the absolute value of I_{leak} . However, we needed to obtain an estimate of leak conductance (g_{leak}) for the purposes of the model (**Equation (5)**). We could not use the absolute value of I_{leak} as measured in our voltage clamped neurons because of blockage of potassium channels with Cs internals. Hence, for use in our conductance model, g_{leak} measurements were not taken from our voltage clamp data, and instead the value was taken from literature.

Fitting data

Voltage clamp data was fit to a difference of exponential functions (**Equation (8), Figure 6—figure supplement 1e**) by a non-linear least squares minimization algorithm using lmfit, a freely available curve fitting library for Python. Using this, we obtained amplitudes (\bar{g}), time course ($\tau_{\text{rise}}, \tau_{\text{decay}}$) and onset delay from stimulus (δ_{onset}) for both excitatory and inhibitory currents. We then calculated inhibitory onset delay (δ_{inh}) by subtracting onset delay of excitatory from inhibitory traces.

$$g(t) = \bar{g} \left(\frac{e^{\left(\frac{\delta_{\text{onset}} - t}{\tau_{\text{decay}}}\right)} - e^{\left(\frac{\delta_{\text{onset}} - t}{\tau_{\text{rise}}}\right)}}{-\left(\frac{\tau_{\text{rise}}}{\tau_{\text{decay}}}\right)^{\frac{\tau_{\text{decay}} - \tau_{\text{rise}}}{\tau_{\text{decay}}}}} + \left(\frac{\tau_{\text{rise}}}{\tau_{\text{decay}}}\right)^{\frac{\tau_{\text{decay}} - \tau_{\text{rise}}}{\tau_{\text{decay}}}}} \right) \quad (8)$$

Onset detection

Onsets were also detected using three methods. Since we propose onset delays to be a function of the excitation peak, we avoided onset finding methods such as time to 10% of peak, which rely on peaks of the PSCs. We used threshold based (time at which the PSC crossed a threshold), slope based (time at which the slope of the PSC onset was the steepest) and a running window based method. In the running window method, we ran a short window of 0.5 ms, and found the time point at which distributions of two consecutive windows became dissimilar, using a two sample KS test. Ideally, with no input, the noise distribution across two consecutive windows should remain identical. All three methods gave qualitatively similar results.

Modeling detailed balanced synapses

Synaptic inputs were modeled as sums of probabilistically activated basal synapses with synaptic strengths taken from a lognormal distribution with shape and scale parameters as given by our one square current clamp data (shape = -0.39, scale = 0.80). The width of the weight distribution was altered by changing the scale parameter. Probabilistic synaptic activation was modeled as a binomial process, with synaptic 'release probability' for excitatory and inhibitory inputs set at 0.2 and 0.8, respectively.

Inhibitory inputs were generated with various degrees of correlation to the excitation, by shuffling the excitatory weights in differently sized bins, from one to the length of the excitatory weight vector, controlled by a parameter ρ . In this manner, as ρ changed from 1 to 0, excitatory and inhibitory weight vectors changed from paired (detailed balance) to completely unpaired but with identical mean and variance of the weight distributions (global balance).

These synapses could be engaged by delivering stimuli, with the number of synapses per stimulus sampled from a Poisson distribution with mean of 5 synapses per stimulus. The total number of excitatory and inhibitory synaptic inputs engaged by a stimulus were always identical. Each stimulus was repeated six times. The resultant means and standard deviations for excitatory and inhibitory inputs were plotted against each other to compare different degrees of correlation. The whole process was repeated 100 times, and correlations and r-squared values were averaged to generate the heatmaps.

Mutual information calculation

Mutual information was calculated by non-parametric entropy estimation and histogram methods. NPEET (<https://github.com/gregversteeg/NPEET>) was used for non-parametric estimation of Mutual Information. The relationship between variables was shuffled 500 times to find the significance of the Mutual Information estimate. If the true value of MI was not larger than 90% of the distribution obtained by shuffling, mutual information was assumed to be 0. If the total information about the linear sum of one square responses using both peak amplitude and time could not be established with 90% confidence as described above, the cell was excluded from further analysis. We also used the histogram method to find the mutual information (data not shown), and saw a similar trend. Cells with fewer than 80 trials and less than 2 mV inter-quartile range in the linear sum from one square PSP were excluded from the analysis. The calculated linear sum from one square PSP peak amplitude responses, measured N-square peak amplitudes and time were binned with an equal number of bins. The number of bins were calculated using Sturges' Rule, which selects the number of bins as $1 + 3.3 \log n$, where n is the total number of observations for a given neuron. Bin frequencies were divided by the total number of responses to get the probability of occurrence $p(x)$ of each bin.

Mutual Information was then calculated for all pairs of combinations between linear sum, peak amplitude and time using **Equation (9)** and **(10)**.

$$MI(X, Y) = H(X) + H(Y) - H(X, Y) \quad (9)$$

where Shannon's entropy $H(X)$ for a variable X , is given as:

$$H(X) = \sum_{x \in X} -p(x)\log_2 p(x) \quad (10)$$

Further, conditional mutual information was calculated to measure gain in information about input (linear sum) by knowledge of peak timing when peak amplitude is already known. It was calculated using **Equation 11**.

$$I(X;Y|Z) = H(X,Z) + H(Y,Z) - H(X,Y,Z) - H(Z) \quad (11)$$

Normalized mutual information was calculated by dividing mutual information between pairs of variables by the total information between all three variables (**Equation 12**).

$$I(X;Y,Z) = H(Z) + H(X,Y) - H(X,Y,Z) \quad (12)$$

Cross-pulse adaptation

We individually presented five unique photostimulation spots in all possible pairwise combinations, with an inter-stimulus interval of 50 ms (*Dittman et al., 2000*), to test for the interaction using a Cross Pulse Adaptation protocol. We then compared the averages of ten repeats of the response for a given spot when it arrived second in the stimulus-pair, to when it came first. Hence, if there is facilitation caused due to the presence of the first spot, then we should observe that the response to the spot when it comes second is larger than when it comes first in the stimulus pair. To quantify this change, we calculated the ratio between the average response of the spot, when it arrives at the second place, to the response when it arrives at the first place. This gave us the Cross Pulse Ratio (*Figure 4—figure supplement 1b*). A necessary internal control was that the self-self spot pairs should get facilitated. However, we observed lack of facilitation for self-self pairs, for all the cells we tested (*Figure 4—figure supplement 1, n = 6* cells). To ensure that this effect was not due to a limitation of the preparation, we tested paired pulse facilitation with electrical stimulation on the same neuron which depressed with optical stimulation. We show that the neuron shows PPF with electrical, but not with optical stimulation (*Figure 4—figure supplement 1a*). Unlike electrical stimulation, which strongly and briefly stimulates many axonal fibres, optical stimulation targets neurons with varying degrees of strengths, and incomplete recovery of ChR2 from desensitization at such short timescales may be the reason for the second pulse not being as effective as the first one. This interfered with our ability to measure paired pulse facilitation and introduced uncertainty in interpreting cross-pulse effects. This precluded further investigation using this approach.

Distributedness and physical distance between square patterns

We calculated the effect of the interaction due to physical proximity of photostimulation squares on the responses. We defined a quantity distributedness, as the sum of the distance between all simultaneously stimulated spots from the combined centre of mass of these spots (*Figure 4—figure supplement 1d*). We compared this to degree of sublinearity, that is the ratio between the Observed response (O) and the Expected sum (E) of individual squares. Thus, if the interaction between neighbouring squares caused sublinearity, we would see a positive correlation between the distributedness and O/E ratio (for the stimuli within an N-square set). Conversely, a negative correlation would imply supralinearity.

We also checked for any interaction that may be taking place between two different optical stimulation patterns. To quantify this, we measured distances on the grid map between all spots in all pairs of patterns, and compared it against the V_m change they caused at CA1 (*Figure 4—figure supplement 1e*).

Acknowledgements

AB and SM were supported by NCBS/TIFR and Council of Scientific and Industrial Research (CSIR). We acknowledge support from the University Grants Commission/Israel Science Foundation grant (UGC/ISF No. F 6-18/2014(IC)). We acknowledge the National Mouse Resource facility funded by Department of Biotechnology for housing and maintaining all animals used in this study. We would like to thank Nikhila Krishnan and Shriya Palchaudhuri for help with genotyping; Ashesh Dhawale for help in building the optical stimulation setup; and, Sathyaa Subramaniyam, Deepanjali Dwivedi,

Oliver Muthmann, Mehrab Modi, Dinesh Natesan, Aditya Gilra, Arvind Kumar and Rishikesh Narayanan for discussions and suggestions on the manuscript.

Additional information

Competing interests

Upinder Singh Bhalla: Reviewing editor, eLife. The other authors declare that no competing interests exist.

Funding

Funder	Grant reference number	Author
University Grants Commission	UGC/ISF No. F 6-18/2014 (IC)	Upinder Singh Bhalla
Israel Science Foundation	UGC/ISF No. F 6-18/2014 (IC)	Upinder Singh Bhalla
Council of Scientific and Industrial Research	Senior Research Fellowship	Sahil Moza
National Centre for Biological Sciences	Graduate Student Fellowship	Aanchal Bhatia Sahil Moza

The funders had no role in study design, data collection and interpretation, or the decision to submit the work for publication.

Author contributions

Aanchal Bhatia, Conceptualization, Data curation, Formal analysis, Investigation, Visualization, Methodology, Writing—original draft, Writing—review and editing; Sahil Moza, Conceptualization, Data curation, Software, Formal analysis, Validation, Investigation, Visualization, Methodology, Writing—original draft, Writing—review and editing; Upinder Singh Bhalla, Conceptualization, Resources, Software, Supervision, Funding acquisition, Writing—original draft, Project administration, Writing—review and editing

Author ORCIDs

Aanchal Bhatia  <http://orcid.org/0000-0003-4709-115X>

Sahil Moza  <http://orcid.org/0000-0002-2225-8841>

Upinder Singh Bhalla  <https://orcid.org/0000-0003-1722-5188>

Ethics

Animal experimentation: All experimental procedures were approved by the National Centre for Biological Sciences Institutional Animal Ethics Committee (Protocol number USB-19-1/2011), in accordance with the guidelines of the Government of India (animal facility CPCSEA registration number 109/1999/CPCSEA) and equivalent guidelines of the Society for Neuroscience. CA3-cre (C57BL/6-Tg (Grik4-cre) G32-4StJ/J mice, Stock number 006474) were obtained from Jackson Laboratories. The animals were housed in a temperature controlled environment with a 14-h light: 10h dark cycle, with ad libitum food and water.

Decision letter and Author response

Decision letter <https://doi.org/10.7554/eLife.43415.029>

Author response <https://doi.org/10.7554/eLife.43415.030>

Additional files

Supplementary files

- Supplementary file 1. Table S1 Synaptic time courses chosen for the model. The median, 25% and 75% values for each of the four distributions in **Figure 6—figure supplement 1e** are shown.

DOI: <https://doi.org/10.7554/eLife.43415.021>

- Supplementary file 2. Table S2 Parameters for the conductance model. Parameters for this model were either calculated using electrophysiological experimental conditions, taken from literature (Table S2a) or fit from data (Table S2b).

DOI: <https://doi.org/10.7554/eLife.43415.022>

- Supplementary file 3. Table S3 Parameters for the HH based conductance model. Parameters for this model were either calculated using electrophysiological experimental conditions, or taken from literature. The simulations were conducted using synaptic conductances, measured from voltage clamp data (**Figure 2**).

DOI: <https://doi.org/10.7554/eLife.43415.023>

- Transparent reporting form

DOI: <https://doi.org/10.7554/eLife.43415.024>

Data availability

All simulation data and code are open source and online, available at <https://github.com/sahilm89/linearity> (copy archived at <https://github.com/elife sciences-publications/linearity>). Data is available at Dryad (<http://doi.org/10.5061/dryad.f456k4f>).

The following dataset was generated:

Author(s)	Year	Dataset title	Dataset URL	Database and Identifier
Aanchal Bhatia, Sahil Moza, Upinder Singh Bhalla	2019	Precise excitation inhibition balance controls gain and timing in the hippocampus	http://doi.org/10.5061/dryad.f456k4f	Dryad, 10.5061/dryad.f456k4f

References

- Ahmed OJ, Mehta MR. 2009. The hippocampal rate code: anatomy, physiology and theory. *Trends in Neurosciences* **32**:329–338. DOI: <https://doi.org/10.1016/j.tins.2009.01.009>, PMID: 19406485
- Anderson JS, Carandini M, Ferster D. 2000. Orientation tuning of input conductance, excitation, and inhibition in cat primary visual cortex. *Journal of Neurophysiology* **84**:909–926. DOI: <https://doi.org/10.1152/jn.2000.84.2.909>, PMID: 10938316
- Atallah BV, Scanziani M. 2009. Instantaneous modulation of gamma oscillation frequency by balancing excitation with inhibition. *Neuron* **62**:566–577. DOI: <https://doi.org/10.1016/j.neuron.2009.04.027>, PMID: 19477157
- Barron HC, Vogels TP, Behrens TE, Ramaswami M. 2017. Inhibitory engrams in perception and memory. *PNAS* **13**:201701812. DOI: <https://doi.org/10.1073/pnas.1701812114>
- Bartley AF, Dobrunz LE. 2015. Short-term plasticity regulates the excitation/inhibition ratio and the temporal window for spike integration in CA1 pyramidal cells. *European Journal of Neuroscience* **41**:1402–1415. DOI: <https://doi.org/10.1111/ejn.12898>, PMID: 25903384
- Basu J, Zaremba JD, Cheung SK, Hitti FL, Zemelman BV, Losonczy A, Siegelbaum SA. 2016. Gating of hippocampal activity, plasticity, and memory by entorhinal cortex long-range inhibition. *Science* **351**:aaa5694. DOI: <https://doi.org/10.1126/science.aaa5694>, PMID: 26744409
- Bezaire MJ, Soltesz I. 2013. Quantitative assessment of CA1 local circuits: knowledge base for interneuron-pyramidal cell connectivity. *Hippocampus* **23**:751–785. DOI: <https://doi.org/10.1002/hipo.22141>, PMID: 23674373
- Bittner KC, Grienberger C, Vaidya SP, Milstein AD, Macklin JJ, Suh J, Tonegawa S, Magee JC. 2015. Conjunctive input processing drives feature selectivity in hippocampal CA1 neurons. *Nature Neuroscience* **18**:1133–1142. DOI: <https://doi.org/10.1038/nn.4062>, PMID: 26167906
- Bittner KC, Milstein AD, Grienberger C, Romani S, Magee JC. 2017. Behavioral time scale synaptic plasticity underlies CA1 place fields. *Science* **357**:1033–1036. DOI: <https://doi.org/10.1126/science.aan3846>, PMID: 28883072
- Bruno RM. 2011. Synchrony in sensation. *Current Opinion in Neurobiology* **21**:701–708. DOI: <https://doi.org/10.1016/j.conb.2011.06.003>, PMID: 21723114
- Carandini M, Heeger DJ. 2011. Normalization as a canonical neural computation. *Nature Reviews Neuroscience* **13**:51–62. DOI: <https://doi.org/10.1038/nrn3136>, PMID: 22108672

- Cash S, Yuste R. 1999. Linear summation of excitatory inputs by CA1 pyramidal neurons. *Neuron* **22**:383–394. DOI: [https://doi.org/10.1016/S0896-6273\(00\)81098-3](https://doi.org/10.1016/S0896-6273(00)81098-3), PMID: 10069343
- D'amour JA, Froemke RC. 2015. Inhibitory and excitatory spike-timing-dependent plasticity in the auditory cortex. *Neuron* **86**:514–528. DOI: <https://doi.org/10.1016/j.neuron.2015.03.014>, PMID: 25843405
- Denève S, Machens CK. 2016. Efficient codes and balanced networks. *Nature Neuroscience* **19**:375–382. DOI: <https://doi.org/10.1038/nn.4243>, PMID: 26906504
- Dittman JS, Kreitzer AC, Regehr WG. 2000. Interplay between facilitation, depression, and residual calcium at three presynaptic terminals. *The Journal of Neuroscience* **20**:1374–1385. DOI: <https://doi.org/10.1523/JNEUROSCI.20-04-01374.2000>, PMID: 10662828
- Enoki R, Inoue M, Hashimoto Y, Kudo Y, Miyakawa H. 2001. GABAergic control of synaptic summation in hippocampal CA1 pyramidal neurons. *Hippocampus* **11**:683–689. DOI: <https://doi.org/10.1002/hipo.1083>, PMID: 11811662
- Froemke RC, Merzenich MM, Schreiner CE. 2007. A synaptic memory trace for cortical receptive field plasticity. *Nature* **450**:425–429. DOI: <https://doi.org/10.1038/nature06289>, PMID: 18004384
- Froemke RC. 2015. Plasticity of cortical excitatory-inhibitory balance. *Annual Review of Neuroscience* **38**:195–219. DOI: <https://doi.org/10.1146/annurev-neuro-071714-034002>, PMID: 25897875
- Gabernet L, Jadhav SP, Feldman DE, Carandini M, Scanziani M. 2005. Somatosensory integration controlled by dynamic thalamocortical feed-forward inhibition. *Neuron* **48**:315–327. DOI: <https://doi.org/10.1016/j.neuron.2005.09.022>, PMID: 16242411
- Grienberger C, Milstein AD, Bittner KC, Romani S, Magee JC. 2017. Inhibitory suppression of heterogeneously tuned excitation enhances spatial coding in CA1 place cells. *Nature Neuroscience* **20**:417–426. DOI: <https://doi.org/10.1038/nn.4486>, PMID: 28114296
- Haider B, Duque A, Hasenstaub AR, McCormick DA. 2006. Neocortical network activity in vivo is generated through a dynamic balance of excitation and inhibition. *Journal of Neuroscience* **26**:4535–4545. DOI: <https://doi.org/10.1523/JNEUROSCI.5297-05.2006>, PMID: 16641233
- Heiss JE, Katz Y, Ganmor E, Lampl I. 2008. Shift in the balance between excitation and inhibition during sensory adaptation of S1 neurons. *Journal of Neuroscience* **28**:13320–13330. DOI: <https://doi.org/10.1523/JNEUROSCI.2646-08.2008>, PMID: 19052224
- Hennequin G, Agnes EJ, Vogels TP. 2017. Inhibitory plasticity: balance, control, and codependence. *Annual Review of Neuroscience* **40**:557–579. DOI: <https://doi.org/10.1146/annurev-neuro-072116-031005>, PMID: 28598717
- Higley MJ, Contreras D. 2006. Balanced excitation and inhibition determine spike timing during frequency adaptation. *Journal of Neuroscience* **26**:448–457. DOI: <https://doi.org/10.1523/JNEUROSCI.3506-05.2006>, PMID: 16407542
- Iascone DM, Li Y, Sumbul U, Doron M, Chen H, Andreu V, Polleux F. 2018. Whole-neuron synaptic mapping reveals local balance between excitatory and inhibitory synapse organization. *bioRxiv*. DOI: <https://doi.org/10.1101/395384>
- Ishizuka N, Weber J, Amaral DG. 1990. Organization of intrahippocampal projections originating from CA3 pyramidal cells in the rat. *The Journal of Comparative Neurology* **295**:580–623. DOI: <https://doi.org/10.1002/cne.902950407>, PMID: 2358523
- Ishizuka N, Cowan WM, Amaral DG. 1995. A quantitative analysis of the dendritic organization of pyramidal cells in the rat hippocampus. *The Journal of Comparative Neurology* **362**:17–45. DOI: <https://doi.org/10.1002/cne.903620103>, PMID: 8576427
- Jensen O, Lisman JE. 2000. Position reconstruction from an ensemble of hippocampal place cells: contribution of theta phase coding. *Journal of Neurophysiology* **83**:2602–2609. DOI: <https://doi.org/10.1152/jn.2000.83.5.2602>, PMID: 10805660
- Kim H, Ährlund-Richter S, Wang X, Deisseroth K, Carlén M. 2016. Prefrontal parvalbumin neurons in control of attention. *Cell* **164**:208–218. DOI: <https://doi.org/10.1016/j.cell.2015.11.038>, PMID: 26771492
- Klyachko VA, Stevens CF. 2006. Excitatory and feed-forward inhibitory hippocampal synapses work synergistically as an adaptive filter of natural spike trains. *PLOS Biology* **4**:e207. DOI: <https://doi.org/10.1371/journal.pbio.0040207>, PMID: 16774451
- Kremkow J, Aertsen A, Kumar A. 2010. Gating of signal propagation in spiking neural networks by balanced and correlated excitation and inhibition. *Journal of Neuroscience* **30**:15760–15768. DOI: <https://doi.org/10.1523/JNEUROSCI.3874-10.2010>, PMID: 21106815
- Lee D, Lin BJ, Lee AK. 2012. Hippocampal place fields emerge upon single-cell manipulation of excitability during behavior. *Science* **337**:849–853. DOI: <https://doi.org/10.1126/science.1221489>, PMID: 22904011
- Lovett-Barron M, Turi GF, Kaifosh P, Lee PH, Bolze F, Sun XH, Nicoud JF, Zemelman BV, Sternson SM, Losonczy A. 2012. Regulation of neuronal input transformations by tunable dendritic inhibition. *Nature Neuroscience* **15**:423–430. DOI: <https://doi.org/10.1038/nn.3024>, PMID: 22246433
- Luz Y, Shamir M. 2012. Balancing feed-forward excitation and inhibition via hebbian inhibitory synaptic plasticity. *PLOS Computational Biology* **8**:e1002334. DOI: <https://doi.org/10.1371/journal.pcbi.1002334>, PMID: 22291583
- Magee JC, Cook EP. 2000. Somatic EPSP amplitude is independent of synapse location in hippocampal pyramidal neurons. *Nature Neuroscience* **3**:895–903. DOI: <https://doi.org/10.1038/78800>, PMID: 10966620
- Murthy VN, Sejnowski TJ, Stevens CF. 1997. Heterogeneous release properties of visualized individual hippocampal synapses. *Neuron* **18**:599–612. DOI: [https://doi.org/10.1016/S0896-6273\(00\)80301-3](https://doi.org/10.1016/S0896-6273(00)80301-3), PMID: 9136769

- Okun M**, Lampl I. 2008. Instantaneous correlation of excitation and inhibition during ongoing and sensory-evoked activities. *Nature Neuroscience* **11**:535–537. DOI: <https://doi.org/10.1038/nn.2105>, PMID: 18376400
- Okun M**, Lampl I. 2009. Balance of excitation and inhibition. *Scholarpedia* **4**:7467. DOI: <https://doi.org/10.4249/scholarpedia.7467>
- Poirazi P**, Brannon T, Mel BW. 2003. Arithmetic of subthreshold synaptic summation in a model CA1 pyramidal cell. *Neuron* **37**:977–987. DOI: [https://doi.org/10.1016/S0896-6273\(03\)00148-X](https://doi.org/10.1016/S0896-6273(03)00148-X), PMID: 12670426
- Pouille F**, Marin-Burgin A, Adesnik H, Atallah BV, Scanziani M. 2009. Input normalization by global feedforward inhibition expands cortical dynamic range. *Nature Neuroscience* **12**:1577–1585. DOI: <https://doi.org/10.1038/nn.2441>, PMID: 19881502
- Pouille F**, Scanziani M. 2001. Enforcement of temporal fidelity in pyramidal cells by somatic feed-forward inhibition. *Science* **293**:1159–1163. DOI: <https://doi.org/10.1126/science.1060342>, PMID: 11498596
- Ray S**, Bhalla US. 2008. PyMOOSE: interoperable scripting in Python for MOOSE. *Frontiers in Neuroinformatics* **2**. DOI: <https://doi.org/10.3389/neuro.11.006.2008>, PMID: 19129924
- Shannon CE**. 1948. A mathematical theory of communication. *Bell System Technical Journal* **27**:379–423. DOI: <https://doi.org/10.1002/j.1538-7305.1948.tb01338.x>
- Shu Y**, Hasenstaub A, Badoval M, Bal T, McCormick DA. 2003. Barrages of synaptic activity control the gain and sensitivity of cortical neurons. *The Journal of Neuroscience* **23**:10388–10401. DOI: <https://doi.org/10.1523/JNEUROSCI.23-32-10388.2003>, PMID: 14614098
- Tsodyks MV**, Markram H. 1997. The neural code between neocortical pyramidal neurons depends on neurotransmitter release probability. *PNAS* **94**:719–723. DOI: <https://doi.org/10.1073/pnas.94.2.719>, PMID: 9012851
- Vogels TP**, Sprekeler H, Zenke F, Clopath C, Gerstner W. 2011. Inhibitory plasticity balances excitation and inhibition in sensory pathways and memory networks. *Science* **334**:1569–1573. DOI: <https://doi.org/10.1126/science.1211095>, PMID: 22075724
- Vogels TP**, Abbott LF. 2009. Gating multiple signals through detailed balance of excitation and inhibition in spiking networks. *Nature Neuroscience* **12**:483–491. DOI: <https://doi.org/10.1038/nn.2276>, PMID: 19305402
- Wehr M**, Zador AM. 2003. Balanced inhibition underlies tuning and sharpens spike timing in auditory cortex. *Nature* **426**:442–446. DOI: <https://doi.org/10.1038/nature02116>, PMID: 14647382
- Wilent WB**, Contreras D. 2005. Dynamics of excitation and inhibition underlying stimulus selectivity in rat somatosensory cortex. *Nature Neuroscience* **8**:1364–1370. DOI: <https://doi.org/10.1038/nn1545>, PMID: 16158064
- Woodson W**, Nitecka L, Ben-Ari Y. 1989. Organization of the GABAergic system in the rat hippocampal formation: a quantitative immunocytochemical study. *The Journal of Comparative Neurology* **280**:254–271. DOI: <https://doi.org/10.1002/cne.902800207>, PMID: 2925894
- Xue M**, Atallah BV, Scanziani M. 2014. Equalizing excitation-inhibition ratios across visual cortical neurons. *Nature* **511**:596–600. DOI: <https://doi.org/10.1038/nature13321>, PMID: 25043046
- Yizhar O**, Fenno LE, Prigge M, Schneider F, Davidson TJ, O’Shea DJ, Sohal VS, Goshen I, Finkelstein J, Paz JT, Stehfest K, Fudim R, Ramakrishnan C, Huguenard JR, Hegemann P, Deisseroth K. 2011. Neocortical excitation/inhibition balance in information processing and social dysfunction. *Nature* **477**:171–178. DOI: <https://doi.org/10.1038/nature10360>, PMID: 21796121
- Zhang LI**, Tan AY, Schreiner CE, Merzenich MM. 2003. Topography and synaptic shaping of direction selectivity in primary auditory cortex. *Nature* **424**:201–205. DOI: <https://doi.org/10.1038/nature01796>, PMID: 12853959
- Zhou M**, Liang F, Xiong XR, Li L, Li H, Xiao Z, Tao HW, Zhang LI. 2014. Scaling down of balanced excitation and inhibition by active behavioral states in auditory cortex. *Nature Neuroscience* **17**:841–850. DOI: <https://doi.org/10.1038/nn.3701>, PMID: 24747575

Appendix 1

DOI: <https://doi.org/10.7554/eLife.43415.025>

Here we compare the analytic form of the PSP peak with and without inhibition. This set of equations furthers our understanding of how the subthreshold divisive normalization takes effect, with changes in EI ratios and inhibitory delays. Here, ω represents the EI ratio at the time of postsynaptic depolarization peak, and η represents the ratio of the excitatory conductances at peak depolarization time in the presence and absence of delayed inhibition.

Finding roots for **Equation 5**,

$$C_m \frac{dV_m}{dt} = g_{\text{leak}} \cdot (E_{\text{leak}} - V_m) + g_{\text{exc}}(t) \cdot (E_{\text{exc}} - V_m) + g_{\text{inh}}(t) \cdot (E_{\text{inh}} - V_m) = 0$$

$$g_{\text{leak}} E_{\text{leak}} + g_{\text{exc}}(t^*) E_{\text{exc}} + g_{\text{inh}}(t^*) E_{\text{inh}} - V_m (g_{\text{leak}} + g_{\text{exc}}(t^*) + g_{\text{inh}}(t^*)) = 0 \quad (\text{A1})$$

Here t^* is the time of PSP peak.

$$V_m(t^*) = \frac{g_{\text{leak}} E_{\text{leak}} + g_{\text{exc}}(t^*) E_{\text{exc}} + g_{\text{inh}}(t^*) E_{\text{inh}}}{g_{\text{leak}} + g_{\text{exc}}(t^*) + g_{\text{inh}}(t^*)} \quad (\text{A2})$$

Subtracting E_{leak} from both sides,

$$\theta = V_m(t^*) - E_{\text{leak}} = \frac{g_{\text{leak}} E_{\text{leak}} + g_{\text{exc}}(t^*) E_{\text{exc}} + g_{\text{inh}}(t^*) E_{\text{inh}}}{g_{\text{leak}} + g_{\text{exc}}(t^*) + g_{\text{inh}}(t^*)} - E_{\text{leak}} \quad (\text{A3})$$

$$\theta = \frac{g_{\text{exc}}(t^*)(E_{\text{exc}} - E_{\text{leak}}) + g_{\text{inh}}(t^*)(E_{\text{inh}} - E_{\text{leak}})}{g_{\text{leak}} + g_{\text{exc}}(t^*) + g_{\text{inh}}(t^*)} \quad (\text{A4})$$

Similarly, with $\bar{g}_{\text{inh}} = 0$ (no inhibition case), let t^{**} be the time of peak.

$$\varepsilon = \frac{g_{\text{exc}}(t^{**})(E_{\text{exc}} - E_{\text{leak}})}{g_{\text{leak}} + g_{\text{exc}}(t^{**})} \quad (\text{A5})$$

Let $\eta = \frac{g_{\text{exc}}(t^*)}{g_{\text{exc}}(t^{**})}$, $\omega = \frac{g_{\text{inh}}(t^*)}{g_{\text{exc}}(t^*)}$, $\Delta E_{\text{exc}} = (E_{\text{exc}} - E_{\text{leak}})$, and $\Delta E_{\text{inh}} = (E_{\text{inh}} - E_{\text{leak}})$

Dividing 4 by 5, and replacing using terms above:

$$\frac{\theta}{\varepsilon} = \frac{\frac{g_{\text{exc}}(t^*)\Delta E_{\text{exc}}}{g_{\text{exc}}(t^{**})\Delta E_{\text{exc}}} + \frac{g_{\text{inh}}(t^*)\Delta E_{\text{inh}}}{g_{\text{exc}}(t^{**})\Delta E_{\text{exc}}}}{\frac{g_{\text{leak}} + g_{\text{exc}}(t^*) + g_{\text{inh}}(t^*)}{g_{\text{leak}} + g_{\text{exc}}(t^{**})}}$$

$$\frac{\theta}{\varepsilon} = \frac{\eta + \omega\eta\frac{\Delta E_{\text{inh}}}{\Delta E_{\text{exc}}}}{\frac{g_{\text{leak}}}{g_{\text{leak}} + g_{\text{exc}}(t^{**})} + (1 + \omega)\frac{g_{\text{exc}}(t^*)}{g_{\text{leak}} + g_{\text{exc}}(t^{**})}, \frac{g_{\text{exc}}(t^{**})\Delta E_{\text{exc}}}{g_{\text{exc}}(t^{**})\Delta E_{\text{exc}}}}$$

$$\frac{\theta}{\varepsilon} = \frac{\eta\left(1 + \omega\frac{\Delta E_{\text{inh}}}{\Delta E_{\text{exc}}}\right)}{\frac{g_{\text{leak}}}{g_{\text{leak}} + g_{\text{exc}}(t^{**})} + \frac{(1 + \omega)}{\Delta E_{\text{exc}}}\eta\varepsilon}$$

Multiplying the numerator and denominator by $\frac{\Delta E_{\text{exc}}}{\eta(1 + \omega)}$

$$\frac{\theta}{\varepsilon} = \frac{\frac{\Delta E_{\text{exc}}(1 + \omega\frac{\Delta E_{\text{inh}}}{\Delta E_{\text{exc}}})}{(1 + \omega)}}{\frac{g_{\text{leak}}\Delta E_{\text{exc}}}{(g_{\text{leak}} + g_{\text{exc}}(t^{**}))(1 + \omega)\eta} + \varepsilon}$$

$$\frac{\theta}{\varepsilon} = \frac{\frac{\Delta E_{\text{exc}}}{(1 + \omega)} + \left(\frac{\omega}{1 + \omega}\right)\Delta E_{\text{inh}}}{\frac{\Delta E_{\text{exc}}}{\left(1 + \frac{g_{\text{exc}}(t^{**})}{g_{\text{leak}}}\right)(1 + \omega)\eta} + \varepsilon}$$

$$\theta = \frac{\lambda\varepsilon}{\gamma + \varepsilon} \quad (\text{A6})$$

$$\lambda = \frac{\Delta E_{\text{exc}}}{(1 + \omega)} \left(1 + \omega\frac{\Delta E_{\text{inh}}}{\Delta E_{\text{exc}}}\right) \quad (\text{A7})$$

$$\gamma = \frac{\Delta E_{\text{exc}}}{(1 + \omega)(1 + \Phi)\eta}, \text{ where } \Phi \frac{g_{\text{exc}}(t^{**})}{g_{\text{leak}}} \quad (\text{A8})$$

When the delay between excitation and inhibition is large, η approaches 1, and ω approaches 0, leading to θ approaching ε . This corresponds to the region where the input-output relationship is almost linear at low values of ε , and becomes increasingly sublinear as ε increases. As the values of η and ω increase, the value of γ decreases, leading to increasing normalization.

Supplementary figures



Figures and figure supplements

Precise excitation-inhibition balance controls gain and timing in the hippocampus

Aanchal Bhatia et al

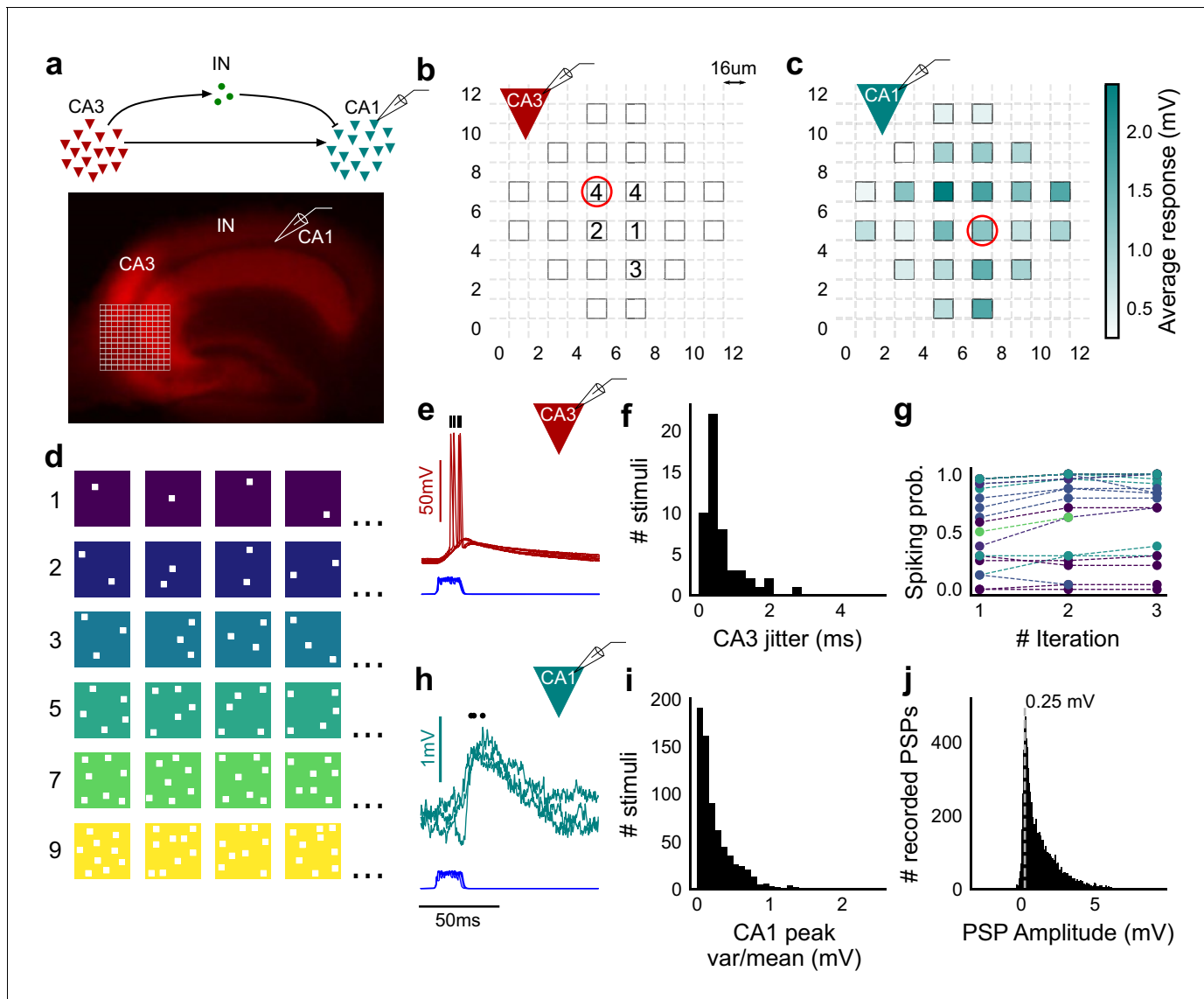


Figure 1. Stimulating CA3-CA1 network with hundreds of optical patterns. (a) Top, schematic of the CA3-CA1 circuit with direct excitation and feedforward inhibition. Bottom, image of a hippocampus slice expressing ChR2-tdTomato (red) in CA3 in a Cre-dependent manner. Optical stimulation grid (not drawn to scale) was centered at the CA3 cell body layer and CA1 neurons were patched. (b) Spike response map of CA3 neuron responses with one grid square active at a time. A CA3 neuron was patched and optically stimulated, in random spatio-temporal order, on the grid locations marked with grey border. This cell spiked (marked with number inside representing spike counts over four trials) in 5 out of 24 such one square stimuli delivered. (c) Heatmap of CA1 responses while CA3 neurons were stimulated with one square optical stimuli. Colormap represents peak V_m change averaged over three repeats. (d) Schematic of optical stimulus patterns. Examples of combinations of N-square stimuli where N could be 1, 2, 3, 5, 7 or 9 (in rows). (e) Spikes in response to four repeats for the circled square, in b. Spike times are marked with a black tick, showing variability in evoked peak times. Blue trace at the bottom represents photodiode measurement of the stimulus duration. Scale bar for time, same as h. (f) Distribution of jitter in spike timing (SD) for all stimuli for all CA3 cells ($n = 8$ cells). (g) CA3 spiking probability (fraction of times a neuron spiked across 24 stimuli, repeated thrice) is consistent over a single recording session. Randomization of the stimulus pattern prevented ChR2 desensitization. Circles, colored as in d depict spiking probability on each repeat of a stimulus set with connecting lines tracking three repeats of the set ($n = 7$ cells). (h) PSPs in response to three repeats of the circled square in c. Peak times are marked with an asterisk. Blue traces at the bottom represent corresponding photodiode traces for the stimulus duration. (i) Distribution of peak PSP amplitude variability (variance/mean) for all 1-square responses ($n = 28$ cells, stimuli = 695). (j) Histogram of peak amplitudes of all PSPs elicited by all 1-square stimuli, over all CA1 cells. Grey dotted line marks the mode ($n = 38$ cells, trials = 8845).

DOI: <https://doi.org/10.7554/eLife.43415.002>

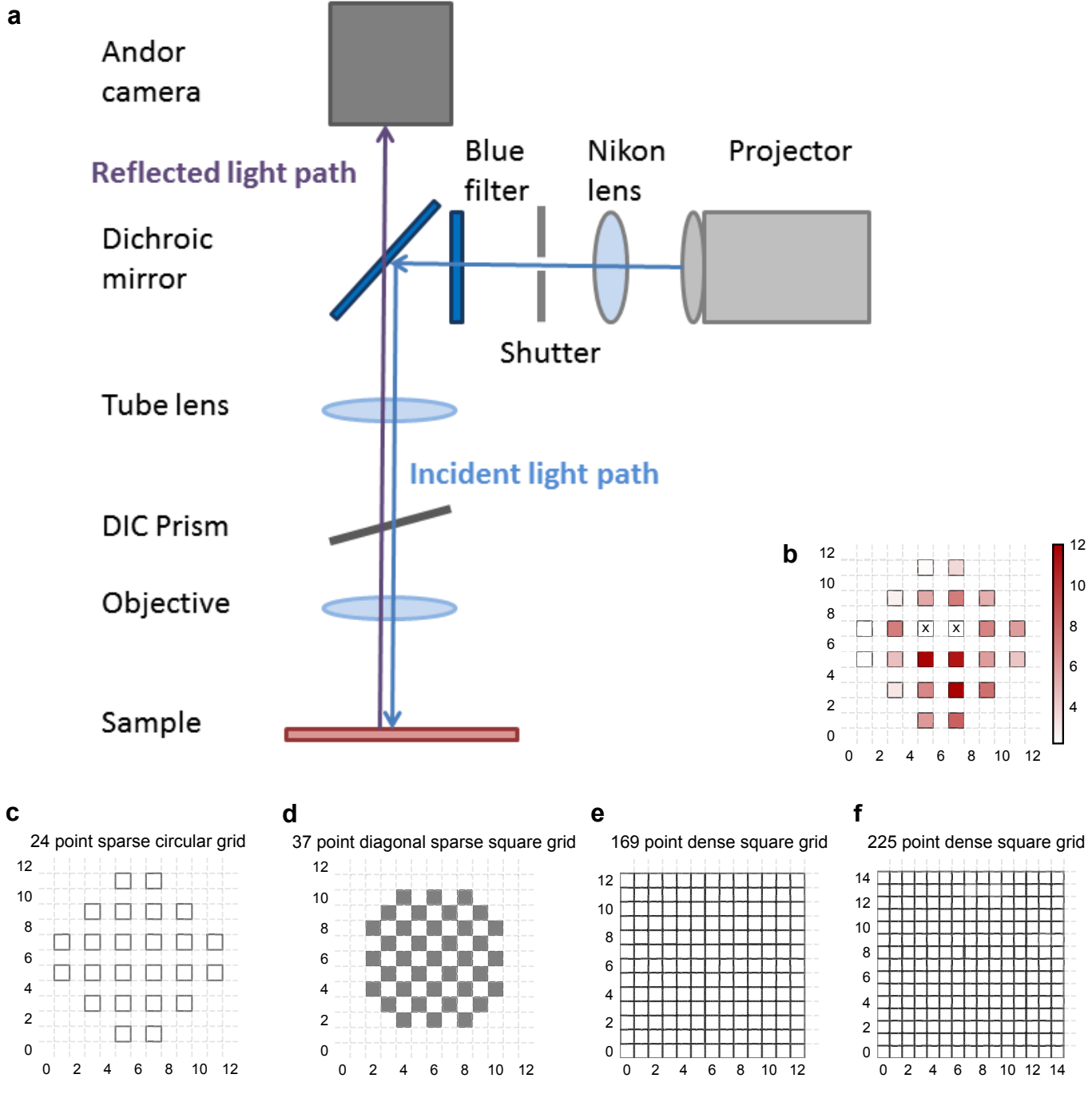


Figure 1—figure supplement 1. Experiment design. (a) Schematic of the light path of patterned optical stimulation. Projector's output was minified using a lens and introduced into the light path of the microscope by reflecting off of a dichroic. We could thus focus arbitrary minified patterns at the sample plane, and switch them at short intervals. (b) Heat map of CA3 neuron responses with one grid square active at a time, from the neuron in **Figure 1b**. Color in grid squares represents peak V_m change from baseline, averaged over trials when the neuron did not spike. Locations where the cell spiked all four times are marked with a cross. (c–f) Four different kinds of grids used for photostimulation. The grid was made sparser to avoid stimulation of the same region with light from nearby photostimulation squares. The four different grids were (from left to right): 24 square circular sparse grid (**Figure 1**) (13 cells), 37 point sparse circular grid (6 cells), 13 × 13 dense grid (9 cells), 15 × 15 dense grid (10 cells). For one cell we used a fifth kind of grid: 112 point dense circular grid (not shown in figure).

DOI: <https://doi.org/10.7554/eLife.43415.003>

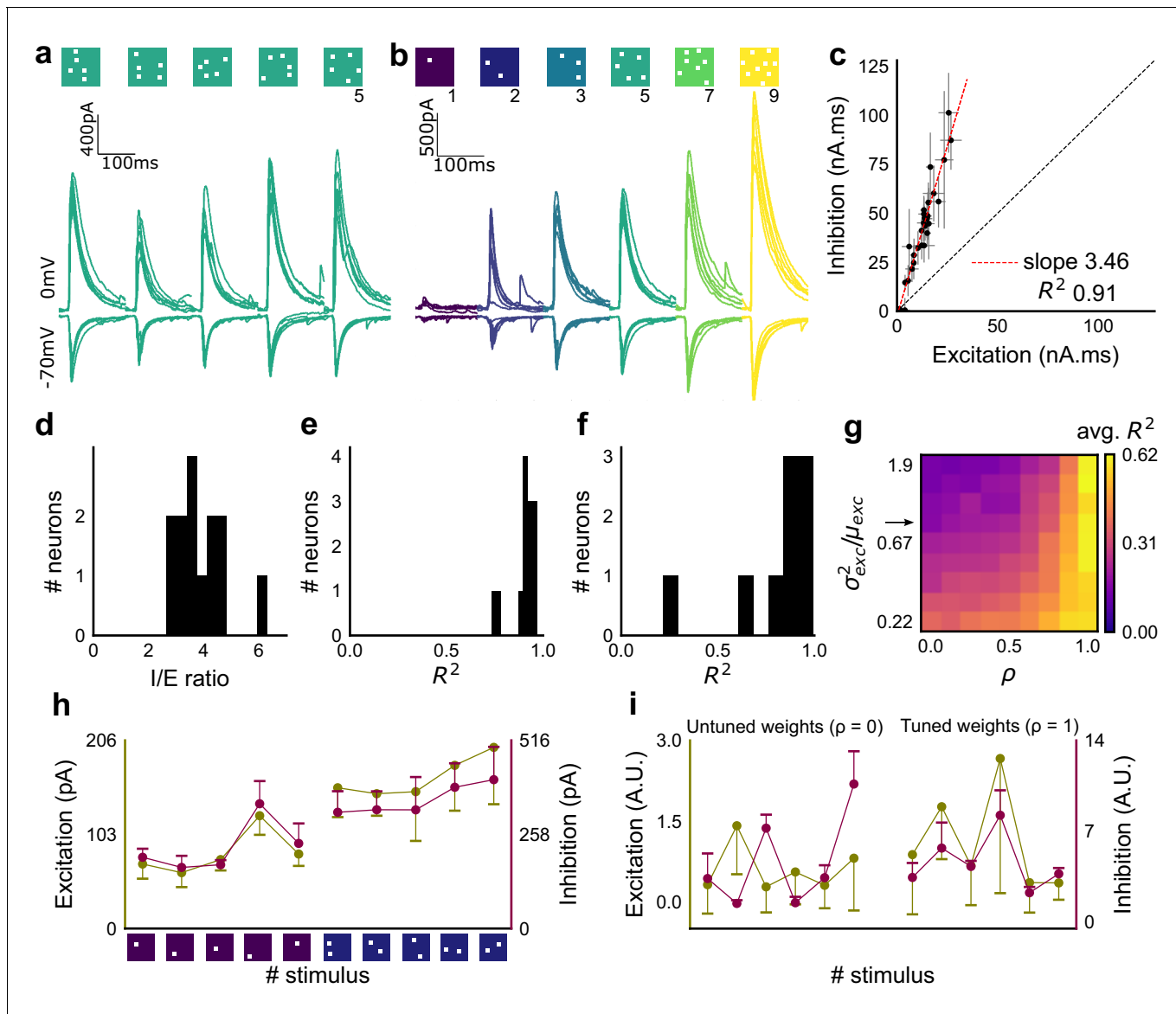


Figure 2. Excitation and inhibition are tightly balanced for all stimuli to a CA1 cell. (a) Monosynaptic excitatory postsynaptic currents (EPSCs, at -70 mV) and disynaptic inhibitory postsynaptic currents (IPSCs, at 0 mV) in response to five different stimulus combinations of 5 squares each. All combinations show proportional excitatory and inhibitory currents over six repeats. Top, schematic of 5-square stimuli. (b) EPSCs and IPSCs are elicited with the same I/E ratio in response to six repeats of a combination, and across six different stimuli from 1 square to nine squares, for the same cell as in a. Top, schematic of the stimuli. (c) Area under the curve for EPSC and IPSC responses, obtained by averaging over six repeats, plotted against each other for all stimuli to the cell in a, b. Error bars are s.d. (d) Summary of I/E ratios for all cells ($n = 13$ cells). (e) Summary for all cells of R^2 values of linear regression fits through all points. Note that 11 out of 13 cells had R^2 greater than 0.9, implying strong proportionality. (f) Same as e, but with linear regression fits for 1 and 2 square responses, showing that even small number of synapses are balanced for excitation and inhibition ($n = 9$ cells). (g) Phase plot from the model showing how tuning of synapses (ρ) affects observation of EI balance (R^2) for various values of variance/mean of the basal weight distribution. Changing the scale of the basal synaptic weight distributions against tuning parameter ρ affects goodness of EI balance fits. Arrow indicates where our observed synaptic weight distribution lay. (h) Example of EI correlations (from data) for 1 and 2 square inputs for an example cell. Bottom, schematic of the stimuli. Excitation and inhibition are colored olive and purple, respectively. Error bars are s.d. (i) Examples of EI correlation (from model) for small number of synapses, from the row marked with arrow in g. The left and right curves show low and high correlations in mean amplitude when EI synapses are untuned ($\rho = 0$) and tuned respectively ($\rho = 1$) (A.U. = Arbitrary Units). Colors, same as h. Error bars are s.d.

DOI: <https://doi.org/10.7554/eLife.43415.004>

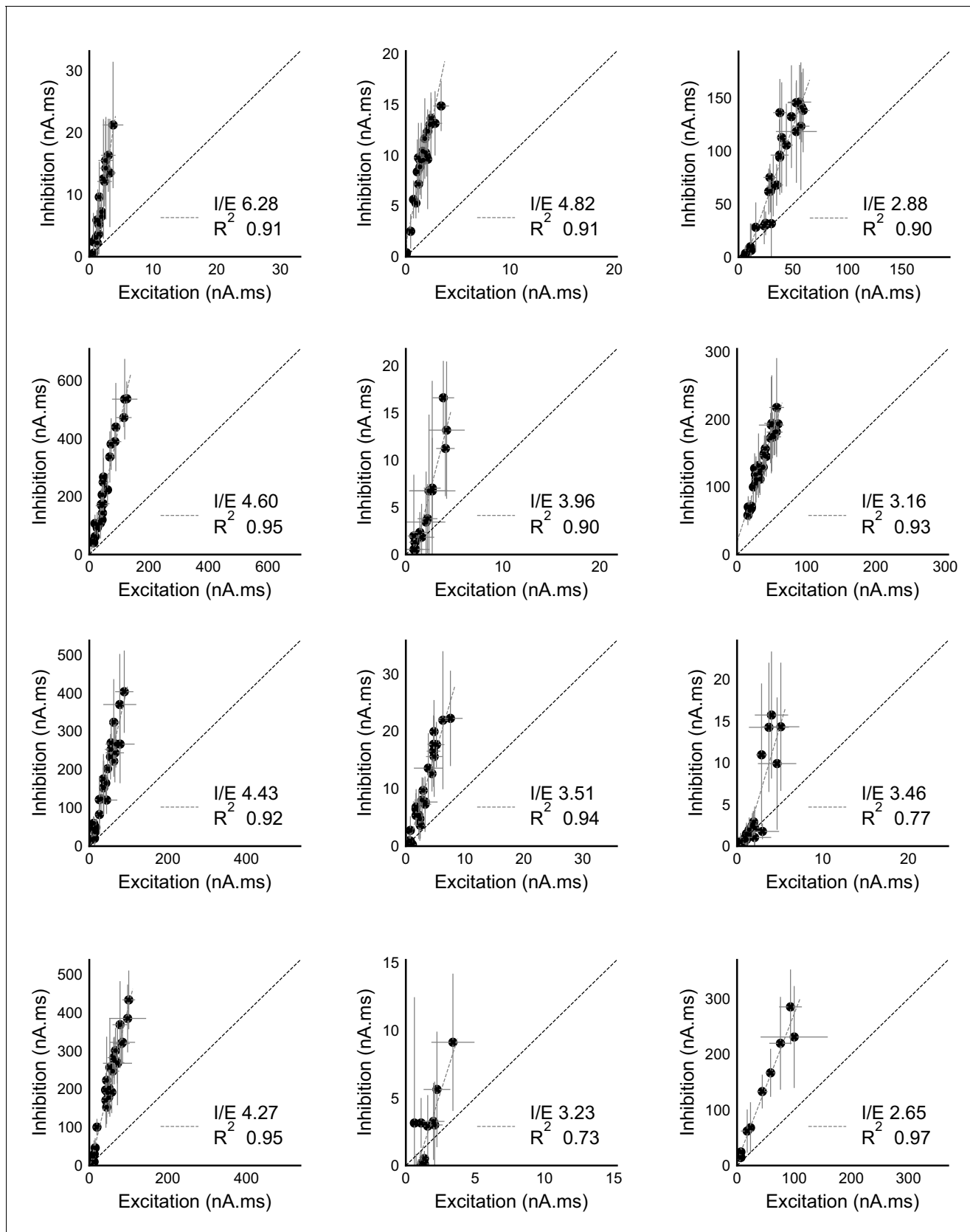


Figure 2—figure supplement 1. Detailed balance in CA3-CA1 feedforward network. (a) Plot of residuals for all inputs (colored by N-square as shown in Figure 1d) of all cells, normalized by their standard deviation. The residuals were calculated by subtracting the actual values of inhibition from the Figure 2—figure supplement 1 continued on next page

Figure 2—figure supplement 1 continued

values predicted by the regression line across the Excitation-Inhibition plot. These were then standardised by dividing individual residual values by the standard deviation across all stimuli of the same number of squares. We found that standardized residuals for different input squares were distributed symmetrically across 0, showing that the I/E ratios did not change substantially across the cell. Variability within stimulus repeats compared with that across all stimuli grouped by the number of squares, for excitation (left) and inhibition (right). For both, within stimulus variability is lower. (b) Variability over repeats of a stimulus (within) divided by variability across all stimuli of the same number of squares delivered to a cell (across), for excitation (left) and inhibition (right). Dotted line represents equal within and across variability. For both excitation and inhibition, within-stimulus variability is lower ($n = 13$ cells). (c) Standard deviation of I/E ratios across stimuli for a given cell was lower than that across all cells (dotted line) for 12 out of 13 cells. (d) Two example cells where EI balance can be observed for 1 and 2 square data from voltage clamped cells (Summary plot in **Figure 2f**). (e) Two example cells where EI balance can be observed for one square data from current clamped cells, as shown in **Figure 5d**. (f) Summary of R^2 for one square data from all current clamped cells ($n = 9$). (g) Histogram of correlation between standard deviations (s.d.) for excitation and inhibition for all stimuli over individual cells. Mean correlation = 0.61 ($n = 13$ cells). (h) A schematic for the detailed balance model. EI correlations increase with increase in ρ , as well as with decrease in variance of the distribution of basal excitatory synaptic weights. (i) Phase plot, similar to **Figure 2g**, but with correlations of standard deviations for excitation and inhibition. Arrow marks the row with our estimated synaptic weight distribution width. (j) Example cell with 0.72 correlation between s.d. of excitation and inhibition repeats over individual stimuli. Excitation and inhibition are colored olive and purple respectively. (k) Examples for s.d. correlation from the row marked with arrow, for untuned (left, $\rho = 0$, corr = 0.22) and tuned (right, $\rho = 1$, corr = 0.87) synapses (A.U. = Arbitrary Units). Colors, same as i. Error bars are s.d.

DOI: <https://doi.org/10.7554/eLife.43415.006>

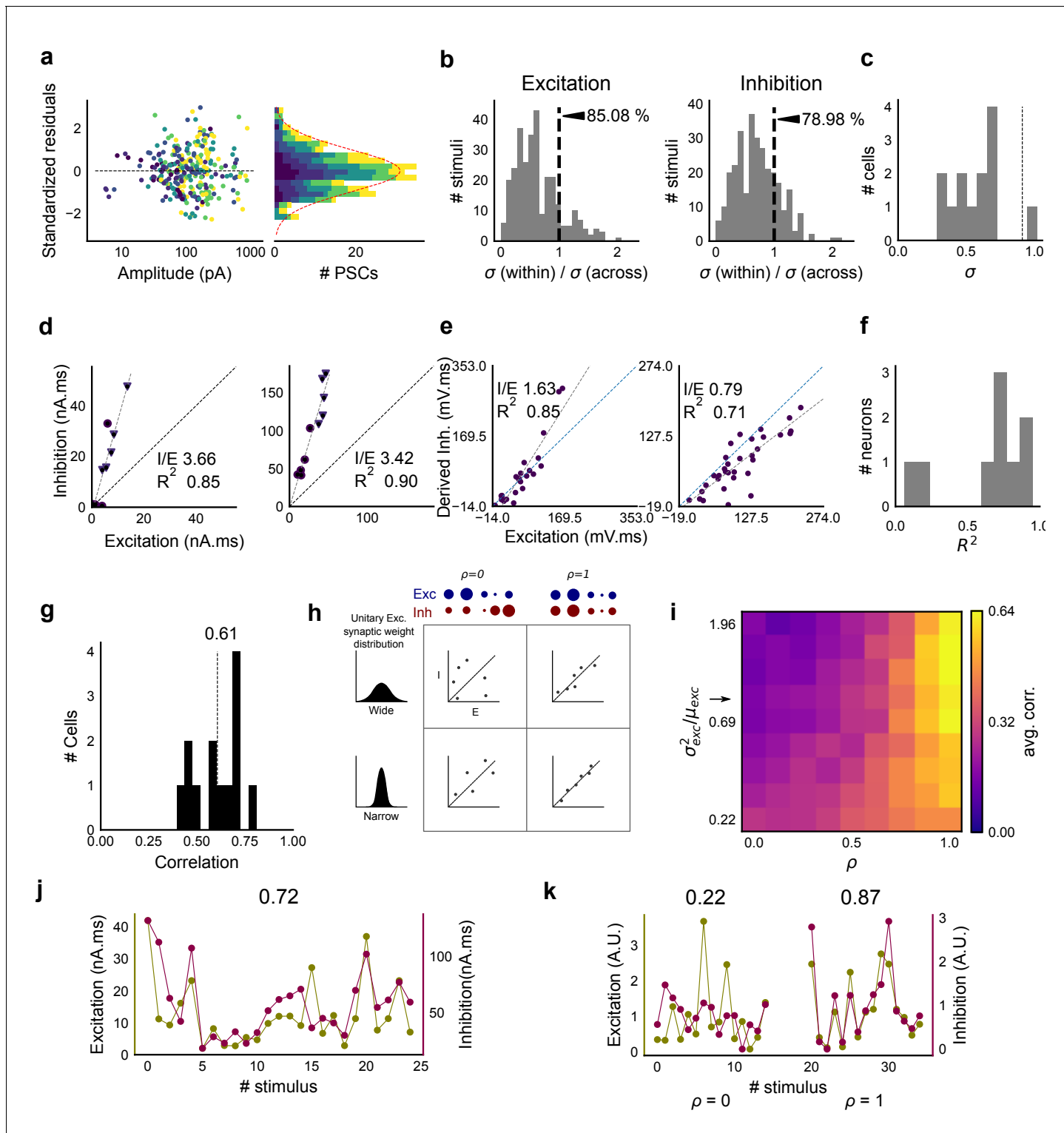


Figure 2—figure supplement 2. Raw data from all cells showing precise balance between excitation and inhibition. Individual plots for area under the curve for excitation and inhibition recorded from all cells (except the display cell in **Figure 2c**). These were measured by clamping the cells at inhibitory (-70 mV) and excitatory (0 mV) reversal potentials respectively. Cells exhibit close proportionality between excitation and inhibition. The I/E ratio (slope) and the R^2 (goodness of fit) for each cell are mentioned in their individual plots. Error bars are s.d.

DOI: <https://doi.org/10.7554/eLife.43415.005>

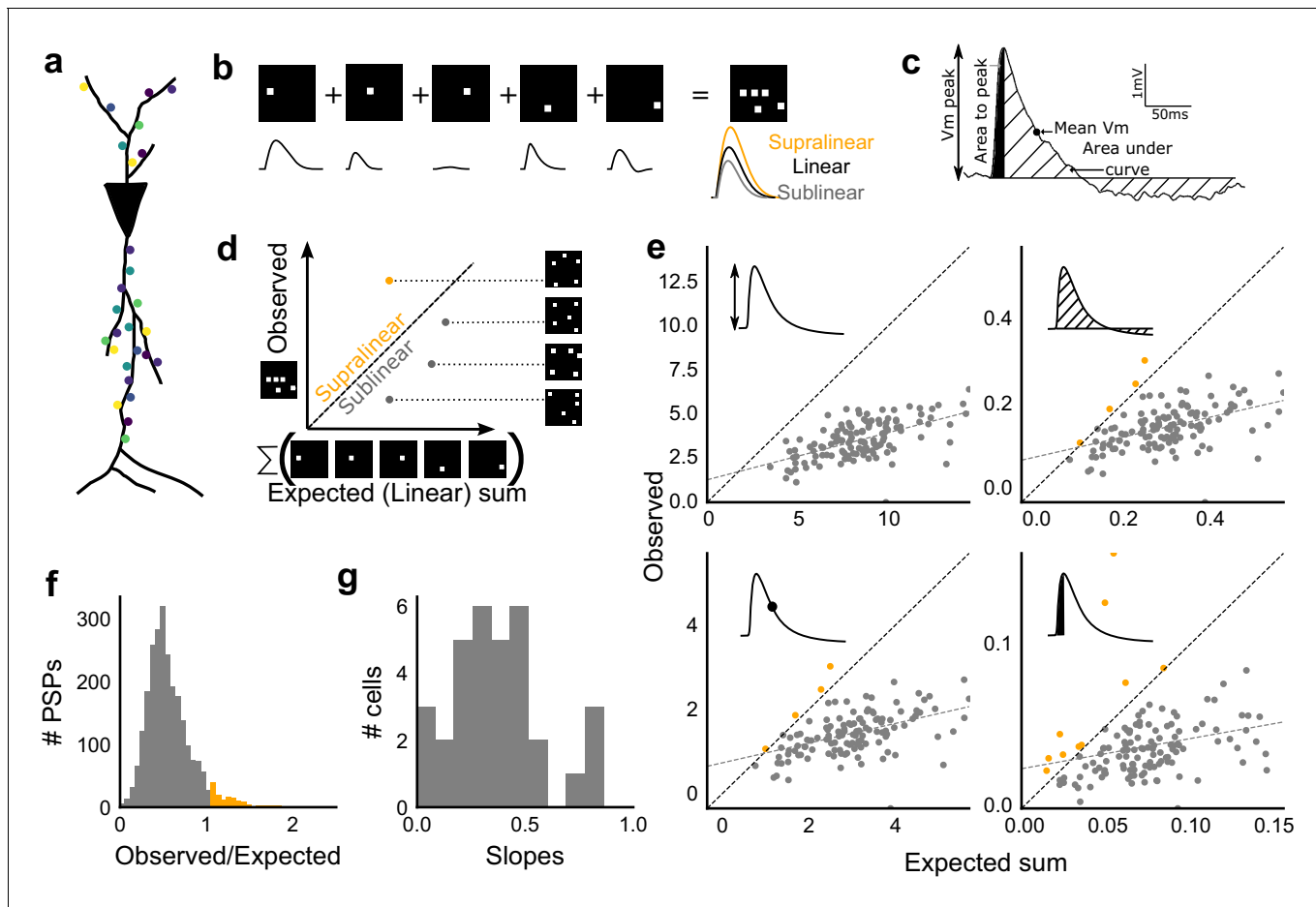


Figure 3. Excitatory and feed-forward inhibitory inputs from CA3 integrate sublinearly at CA1. (a) Schematic of a neuron receiving synaptic input distributed over its dendritic tree. (b) Schematic of input integration. Top, five 1-square stimuli presented individually, and a single 5-square stimulus comprising of the same squares. Bottom, PSPs elicited as a response to these stimuli. 5-square PSP can be larger (supralinear, orange), equal to (linear, black), or smaller (sublinear, grey) than the sum of the single square PSPs. (c) A PSP trace marked with the four measures used for further calculations. PSP peak, PSP area, area to peak and mean voltage are indicated. (d) Schematic of the input integration plot. Each circle represents response to one stimulus combination. ‘Observed’ (true response of 5 square stimulation) on Y-axis and ‘Expected’ (linear sum of 1 square responses) is on X-axis. (e) Most responses for a given cell show sublinear summation for a 5-square stimulus. The four panels show sublinear responses for four different measures (mentioned in c) for the same cell. The grey dotted line is the regression line and the slope of the line is the scaling factor for the responses for that cell. For peak (mV), area (mV.ms), average (mV), and area to peak (mV.ms); slope = 0.27, 0.23, 0.23, 0.18; R^2 0.57, 0.46, 0.46, 0.26, respectively. The responses to AUC and average are similar because of the similarity in the nature of the measure. (f) Distribution of Observed/Expected ratio of peaks of all responses for all 5-square stimuli (mean = 0.57, s.d. = 0.31), from all recorded cells pooled. 93.35% responses to 5-square stimuli were sublinear (2513 PSPs, n = 33 cells). (g) Distribution of slopes for peak amplitude of 5-square stimuli (mean = 0.38, s.d. = 0.22). Regression lines for all cells show that all cells display sublinear (<1 slope) summation (n = 33 cells).

DOI: <https://doi.org/10.7554/eLife.43415.007>

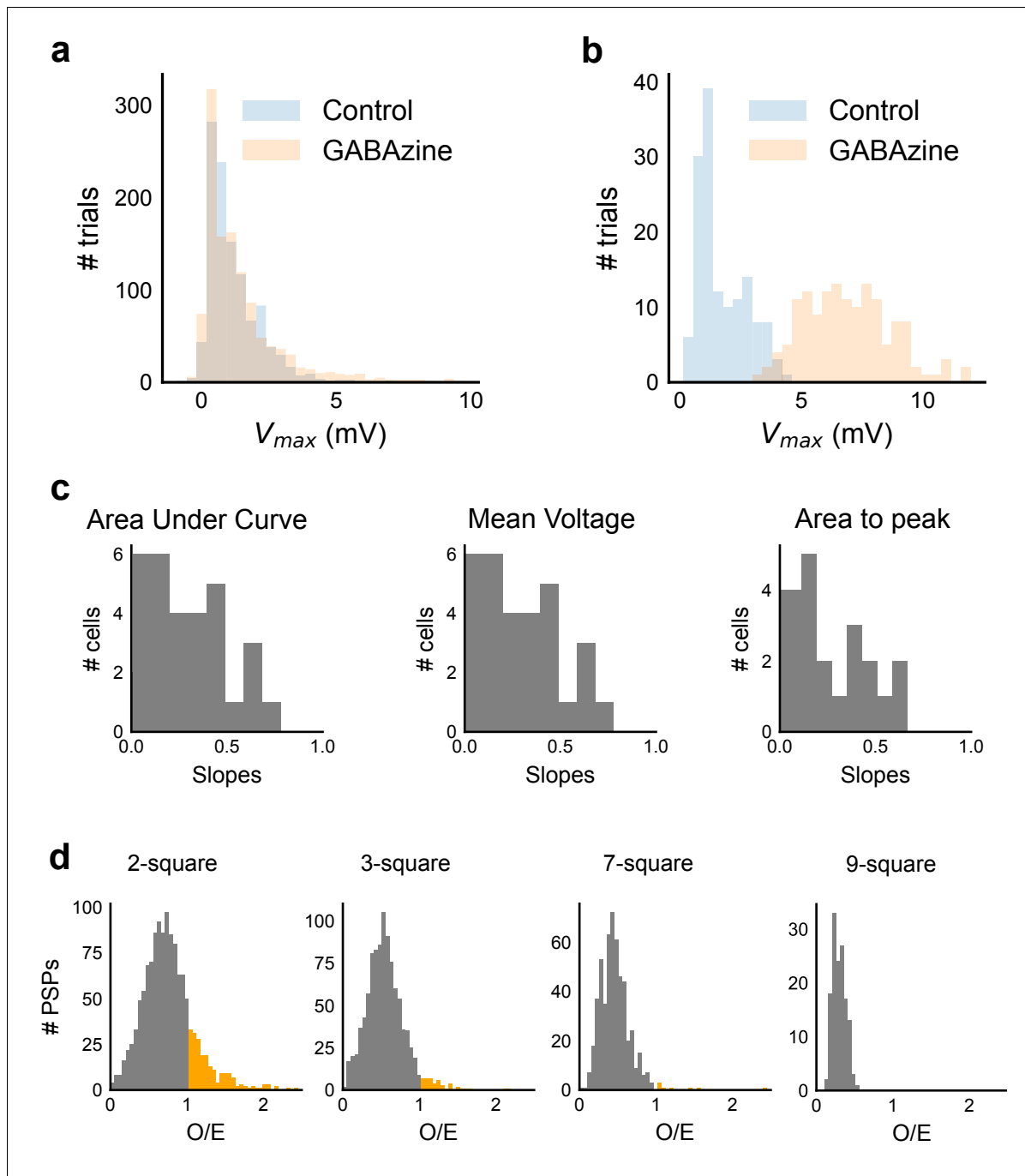


Figure 3—figure supplement 1. Summation at CA3-CA1 network is sublinear. (a) Responses to 1-square photostimulation at CA3 were similar in both Control and GABAazine conditions, except close to the tail of the distribution ($n = 11$, Control: 1092 trials, GABAazine: 1173 trials). This demonstrates that there is very little inhibitory effect on peak V_m with one square photostimulation. (b) Responses to 9-squares photostimulation lead to much larger responses in the presence of GABAazine than in its absence ($n = 3$, Control: 142 trials, GABAazine: 144 trials). Compare this with a. (c) Slope values for three other measures (area under curve, mean voltage and area to peak) of the observed PSP on five square stimulation in all cells. Sublinearity is seen in all four measures ($n = 33$ cells). The slope for first measure, peak V_m , is displayed in **Figure 3g**. Area under curve and Mean voltage panels look alike due to the similarity in the nature of the measure. (d) Summation plots analogous to those in **Figure 3f** for the remaining 2, 3, 7 and 9 stimuli. Observed/Expected (O/E) ratio for most stimuli was less than 1, showing sublinear summation (grey).

DOI: <https://doi.org/10.7554/eLife.43415.008>

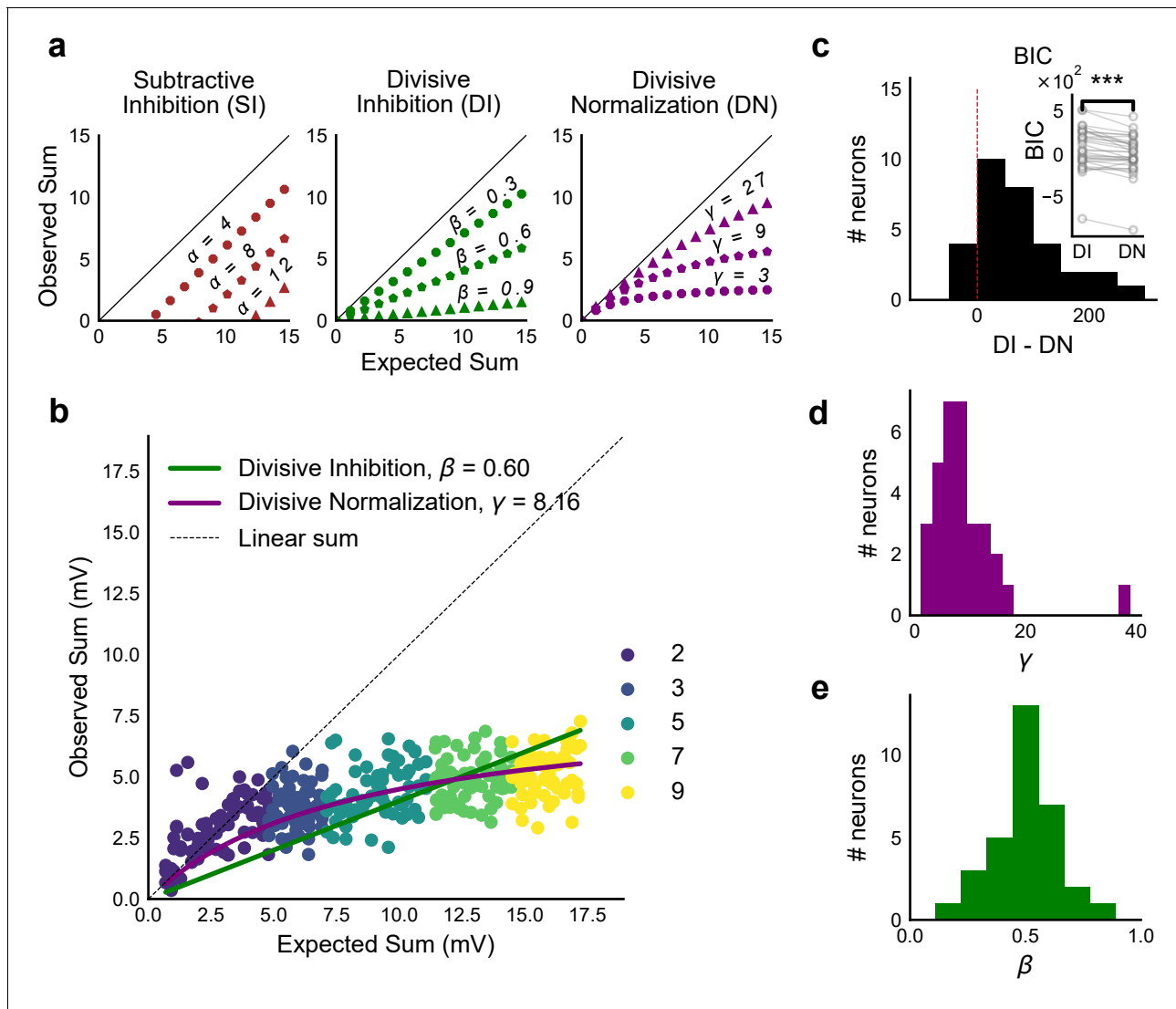


Figure 4. Over a wide input range, integration of CA3 excitatory and feed-forward inhibitory input leads to SDN at CA1. (a) Three phenomenological models of how inhibition interacts with excitation and modulates membrane potential: (left to right) Subtractive Inhibition (SI), Divisive Inhibition (DI) and Divisive Normalization (DN). Note how parameters α , β and γ from **Equation (1)** affect response output. (b) Divisive normalization seen in a cell stimulated with 2, 3, 5, 7 and 9 square combinations. DN and DI model fits are shown in purple and green, respectively. (c) Difference in Bayesian Information Criterion (BIC) values for the two models - DI and DN. Most differences between BIC for DI and DN were less than 0, which implied that DN model fit better, accounting for the number of variables used. Insets show raw BIC values. Raw BIC values were consistently lower for DN model, indicating better fit (Two-tailed paired t-test, $p < 0.00005$, $n = 32$ cells). (d) Distribution of the parameter γ of the DN fit for all cells (median = 7.9, $n = 32$ cells). Compare with a, b to observe the extent of normalization. (e) Distribution of the parameter beta of the DI fit for all cells (mean = 0.5, $n = 32$ cells). Values are less than 1, indicating sublinear behaviour.

DOI: <https://doi.org/10.7554/eLife.43415.009>

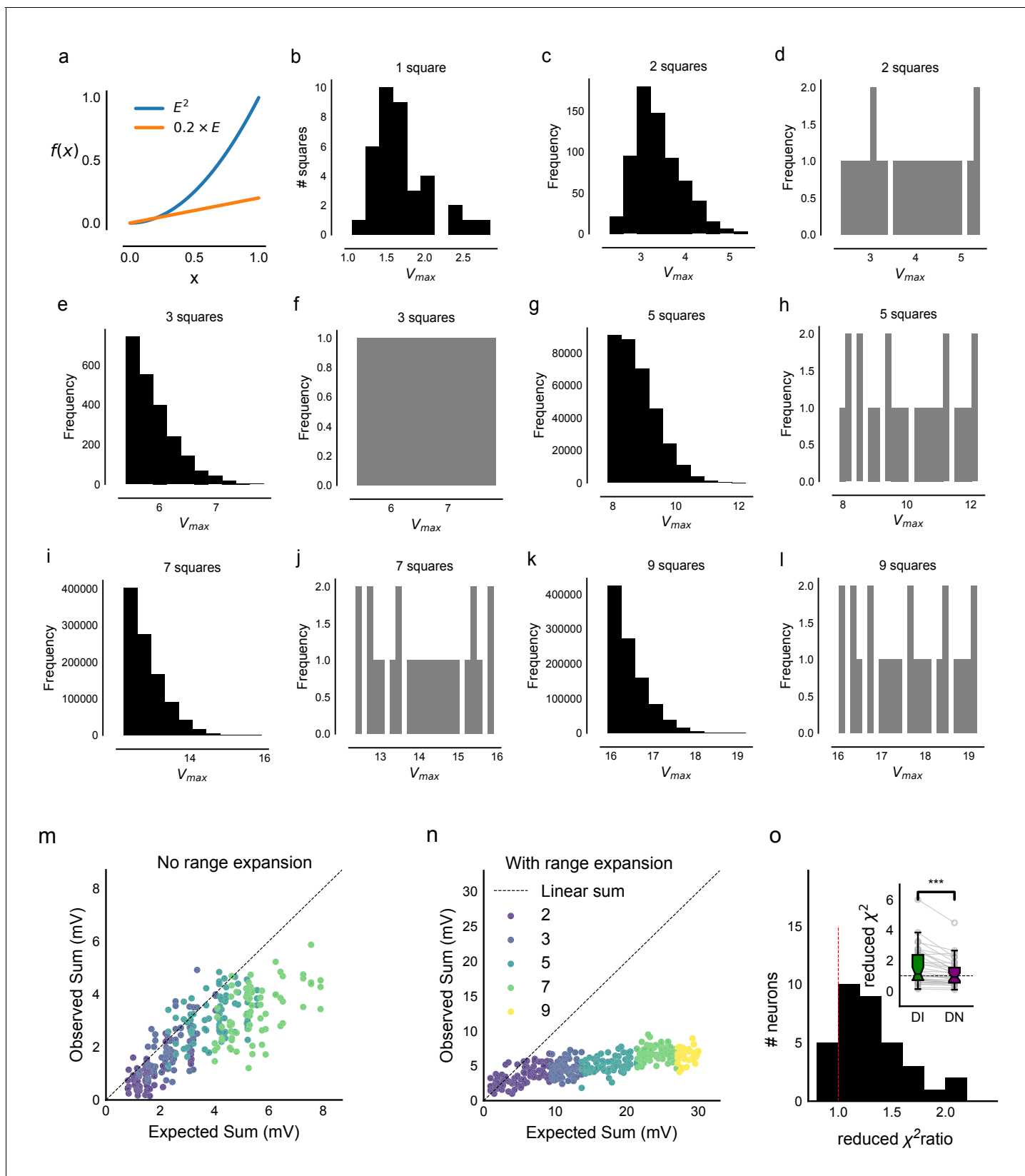


Figure 4—figure supplement 1. Interaction of squares does not affect summation unidirectionally. (a) Example cell showing PPF with electrical, but not with optical stimulation. Individual traces are in grey and black is the average trace. (b) Cross Pulse Ratio (Materials and methods) of 25 pairs of stimuli

Figure 4—figure supplement 1 continued

(from five photostimulation squares) presented to an example cell, different from that in a. Ratio less than one for self-self pairs, on the diagonal, implies lack of facilitation. (c) We restricted our analysis to non-bordering squares and fit the subthreshold divisive normalization model and checked for the value of the normalization parameter (γ). The degree of sublinearity and the input-output curve remained unchanged, as indicated by the similarity in the values of DN parameter γ , ruling out the hypothesis that interactions between neighboring squares account for the observed sublinearity in the SDN curve. (d) Median correlation (0.09) between distributedness of the photostimulation squares and the O/E ratio shows that distances between grid squares do not have a unidirectional relationship with the extent of sublinearity. (e) Median correlation (0.02) between how close the patterns were on the grid to the measured voltage response of CA1 again shows no unidirectional effect of physical proximity of patterns.

DOI: <https://doi.org/10.7554/eLife.43415.011>

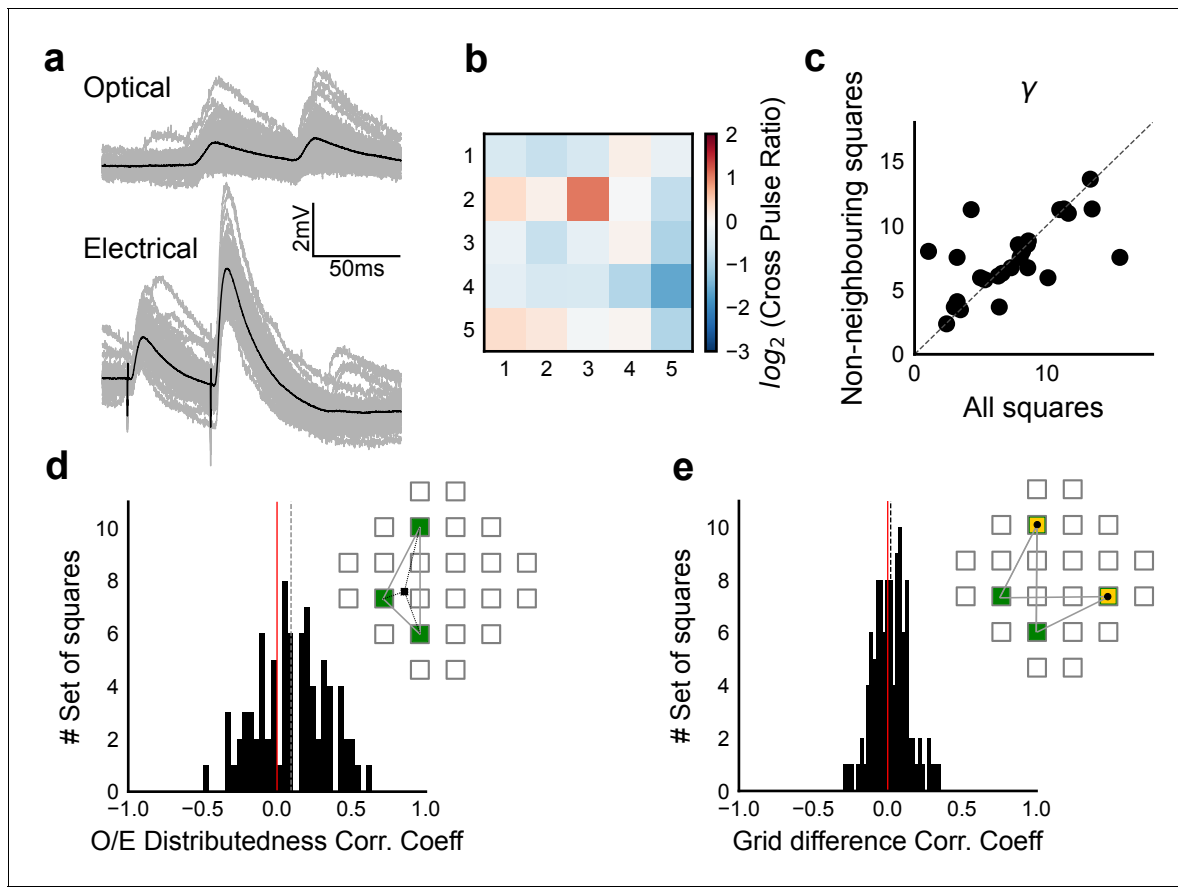


Figure 4—figure supplement 2. Input range expansion for observing nonlinear summation and divisive normalization. (a) A large range of stimulus strengths is required to detect nonlinearity in summation and to characterize divisive normalization. Comparing a nonlinear function of x , $f(x) = x^2$ (blue) with a linear function $f(x) = 0.2x$ (orange). It is difficult to distinguish between the two possibilities (from $x = 0$ to $x = 0.2$). However, across a larger range of x , differences can be seen. (b–l) In order to sample uniformly and over a wider input range of a cell (x axis, labelled Expected sum), we did ‘range expansion’ for some cells ($n = 6$ cells) as follows. A 37-point grid (Figure 1—figure supplement 1c) was used for these experiments. For a given cell, we first measured the 1-square responses to all 37 grid squares. Then, the 1-square responses were binned into 24 bins, and one member was picked from each bin randomly. In case there were fewer than than one member per bin, other bins were resampled without replacement until the total number was 24. Using this, we generated the distributions of expected sum of N-squares ($N = 2, 3, 5, 7, 9$). The distributions of the next N-square was truncated such that its minimum began at the maximum of the last N-square distribution (distributions in black, first column of all rows). For example, if the set of squares were 2, 3, 5, 7, 9, we picked the squares such that the distribution of 5 squares started from the end of 3 squares. We then sampled uniformly from this reduced distribution (distributions in grey, second column of all rows). This allowed us to uniformly sample from the entire theoretically possible range, and hence ensure that we observed summation over a wide range of inputs (as explained in a). (m, n) Responses from one cell without (m) and one with (n) range expansion are shown. Note that responses from different N-squares (shown in different colors, marked as in Figure 1d), are overlapping in the Expected-axis for m, while the process of range expansion enforces exploration of a large input range in a non-overlapping manner in n. (o) Reduced chi-square fits confirm DN model fits better than DI. In addition to BIC (Figure 4c), we used the reduced chi-square fit test to compare the two models of inhibitory computations (divisive inhibition (DI) and divisive normalization (DN)). Divisive normalization model (Equation 3) almost always fit better than divisive inhibition model (Equation 2) for reduced chi-square, as it did for BIC (Figure 4b and c). This figure shows the reduced chi-square ratio plotted for DI and DN models (DI/DN). Values close to one imply good fits, while lesser and greater than one imply over and under-fitting the data respectively. Again, DN is on average closer to one (inset), and the reduced chi-square ratio is almost always larger than one, implying that DN model fit is better than a DI model fit ($n = 32$ cells).

DOI: <https://doi.org/10.7554/eLife.43415.010>

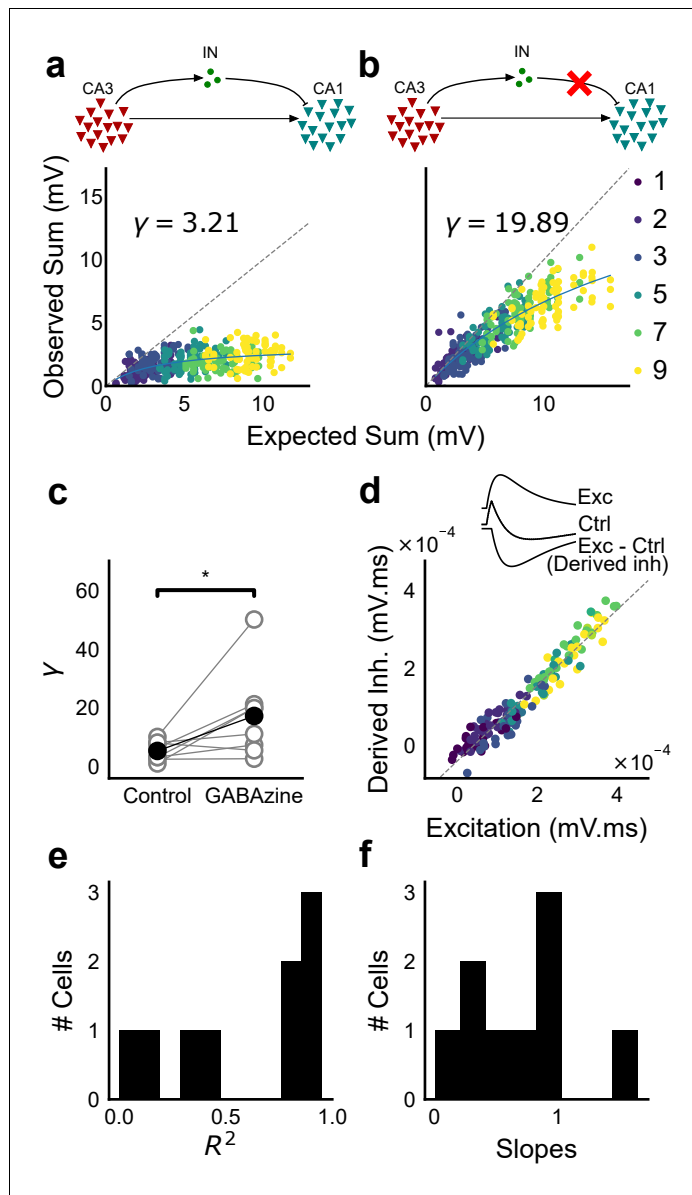


Figure 5. Blocking balanced inhibition at resting membrane potential attenuates SDN. (a) Top, schematic of experiment condition. Bottom, a cell showing divisive normalization in control condition. (b) Top, schematic of experiment condition with feedforward inhibition blocked (2 μM GABAazine). Bottom, responses of the same cell with inhibition blocked. The responses are much closer to the linear summation line (dashed). The blue lines in a, b are the fits of the DN model. The value of γ of the fit increases when inhibition is blocked. (c) Parameter γ was larger with GABAazine in bath (Wilcoxon rank sum test, $p < 0.05$, $n = 8$ cells), implying reduction in normalization with inhibition blocked. (d) Excitation versus derived inhibition for all points for the cell shown in a (area under the curve) (Slope = 0.97, r-square = 0.93, x-intercept = 3.75e-5 $\text{mV} \cdot \text{ms}$). Proportionality was seen for all responses at resting membrane potential. Top, ‘Derived inhibition’ was calculated by subtracting control PSP from the excitatory (GABAazine) PSP for each stimulus combination. (e,f) R^2 (median = 0.8) and slope values (median = 0.7) for all cells ($n = 8$ cells), showing tight IPSP/EPSP proportionality, and slightly more excitation than inhibition at resting membrane potentials.

DOI: <https://doi.org/10.7554/eLife.43415.012>

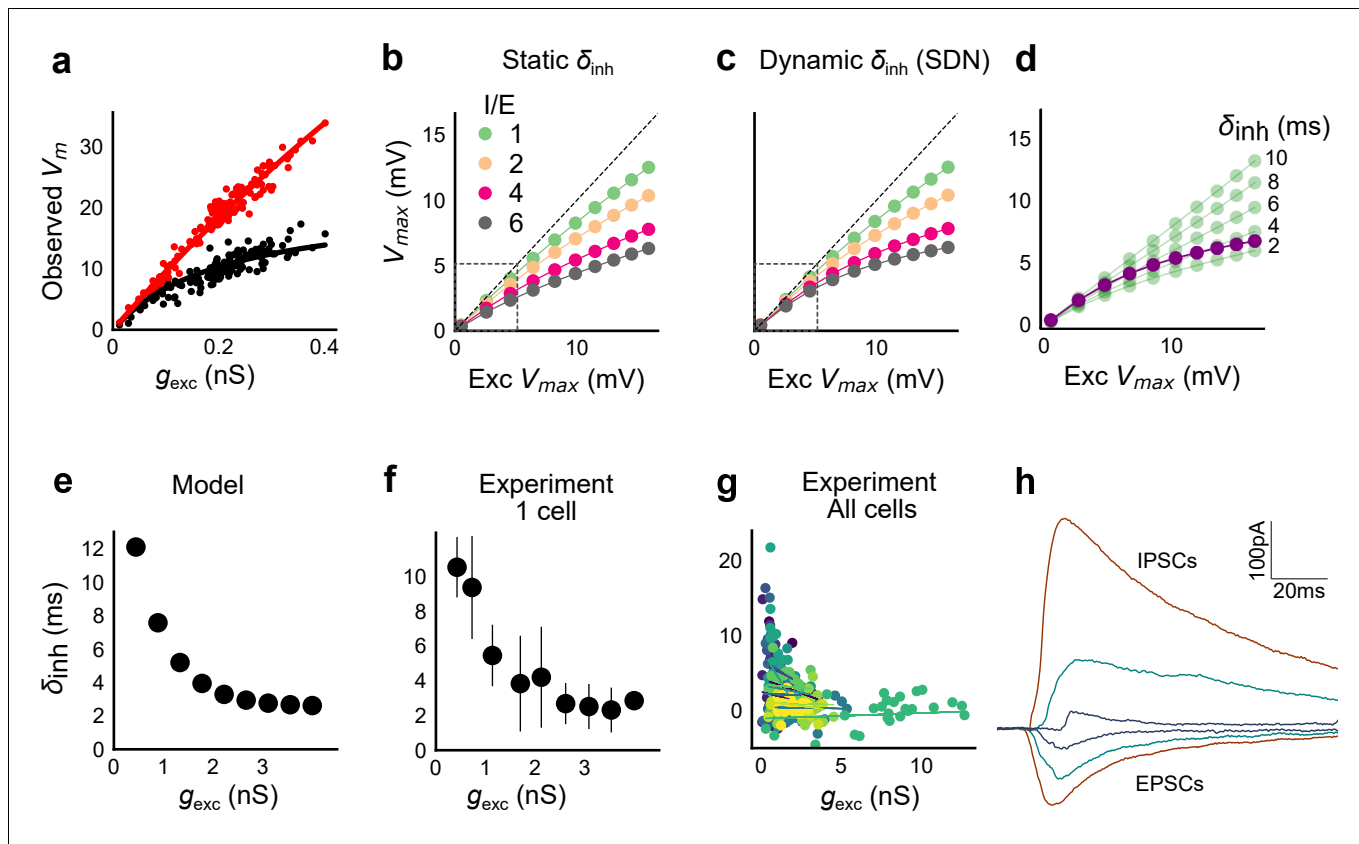


Figure 6. Conductance model predicts Excitatory-Inhibitory delay as an important parameter for divisive normalization. (a) Subthreshold responses from HH model, simulated with traces recorded from one voltage clamped cell (Figure 2). Non-linearly saturating curve, similar to SDN, obtained by simulating with both excitation and inhibition synaptic conductances (black), while the response profile is much more linear with only excitation (red). Each black point is the median response of an excitation trace paired with six different repeats of inhibition for that combination. (b) PSP peak amplitude with both excitatory and balanced inhibitory inputs is plotted against the EPSP peak amplitude with only excitatory input. Model showed sublinear behaviour approximating divisive inhibition for I/E proportionality ranging from 1 to 6 when the inhibitory delay was static. Different colours show I/E ratios. (c) Same as in b, except the inhibitory delay was varied inversely with excitatory conductance (as shown in e). Initial linear zone and diminishing changes in PSP amplitude, indicative of SDN were observed, and the normalization gain was sensitive to the I/E ratio. $\delta_{min} = 2$ ms, $k = 0.5$ nS^{-1} , and $m = 8.15$ ms. Note, the increased overlap in the initial zone (grey box) and the saturation of the PSP peaks in c, as compared to b. (d) Effect of changing EI delay, keeping I/E ratio constant (I/E ratio = 5). Divisive inhibition (green) seen while changing EI delay values from 2 to 10 ms. Divisive normalization (purple) emerges if delays are changed as shown in e. $\delta_{min} = 2$ ms, $k = 0.5$ nS^{-1} , and $m = 13$ ms. (e) Inverse relationship of EI delays with excitation. Inhibitory delay was varied with excitatory conductance in Equation (4) with $\delta_{min} = 2$ ms, $k = 2$ nS^{-1} , and $m = 13$ ms. (f) Data from an example cell showing the relationship of EI delays with excitation. The relationship is similar to the prediction in e. Points are binned averages. Error bars are s.d. (g) Data from all cells showing delay as a function of excitation. Different colors indicate different cells ($n = 13$ cells). Grey lines are linear regression lines through individual cells. (h) Traces (from a voltage clamped neuron) showing the decreasing EI delay with increasing amplitude of PSCs. Each trace is an average of 6 repeats.

DOI: <https://doi.org/10.7554/eLife.43415.013>

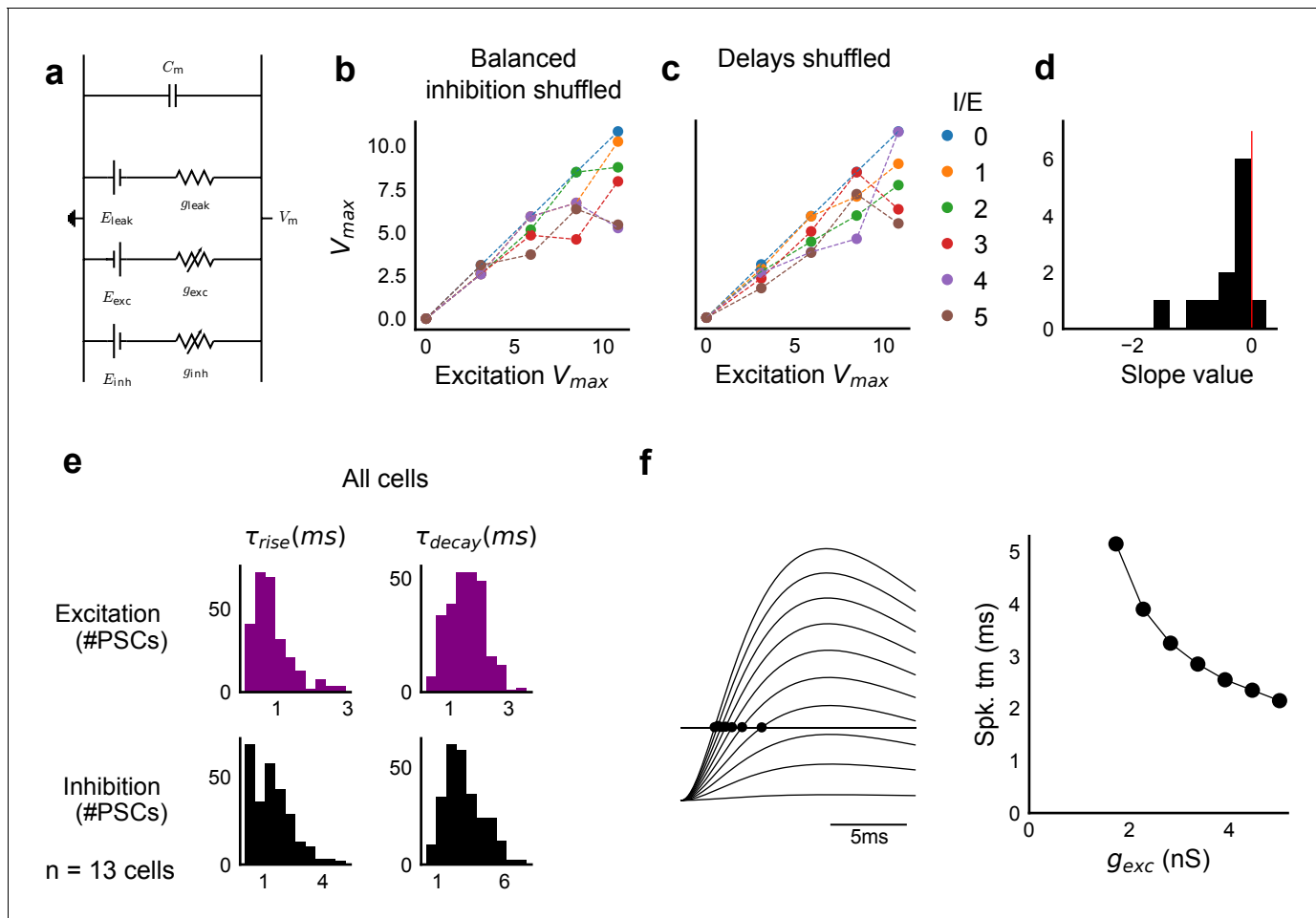


Figure 6—figure supplement 1. Sensitivity of SDN to EI balance and EI delay, and synaptic time courses used for model. (a) Equivalent circuit for the conductance model showing capacitive, excitatory, inhibitory, and leak components. (b,c) Subthreshold divisive normalization was sensitive to I/E ratio (b), and EI delay (c). SDN was lost when the relationship between I/E ratios for a given cell was permuted b. SDN was also lost when the relationship of delay to excitation (Figure 6e) was permuted (c). (d) Histogram of slopes of linear regression lines through EI delays (δ_{inh}) vs excitatory conductance (g_{exc}) for cells in Figure 6g. (e) Rise times (τ_{rise}) and decay times (τ_{decay}) were extracted from optically evoked postsynaptic currents (EPSCs and IPSCs, Figure 2, Figure 2—figure supplement 1) by fitting a difference of exponentials (Figure 6, Equation (8)) ($n = 13$ cells). (f) Schematic showing that our observed delay function (right) can be obtained by thresholding of EPSPs (left) in the simple conductance model.

DOI: <https://doi.org/10.7554/eLife.43415.014>

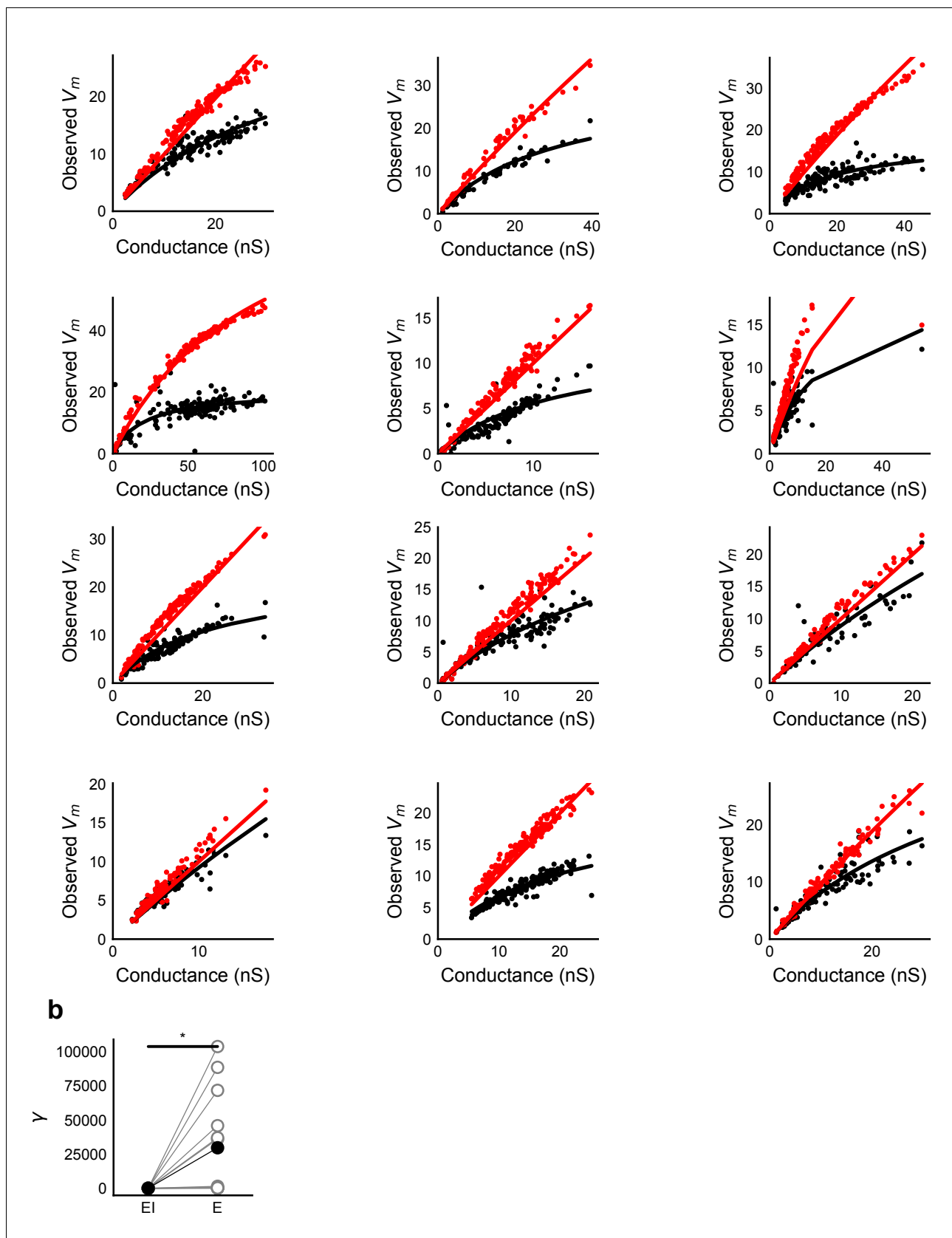


Figure 6—figure supplement 2. HH model simulations with voltage clamped data show SDN. (a) Fits of parameter γ (Equation (3)) to peak V_m vs excitatory conductance for simulations of the HH model with synaptic conductances taken from voltage clamped cells. Black dots are medians for peak *Figure 6—figure supplement 2 continued on next page*

Figure 6—figure supplement 2 continued

depolarization caused by excitatory conductance paired with inhibitory conductance for 6 repeats of the same stimulus. X-axis conductance values were scaled with a factor of 100 for fitting. (b) Difference in fit parameter γ for the case with and without inhibition, black dots are means. The two distributions were significantly different (Wilcoxon rank sum test, $p < 1e-4$, $n = 13$). The fit was susceptible to outliers in some cases.

DOI: <https://doi.org/10.7554/eLife.43415.015>

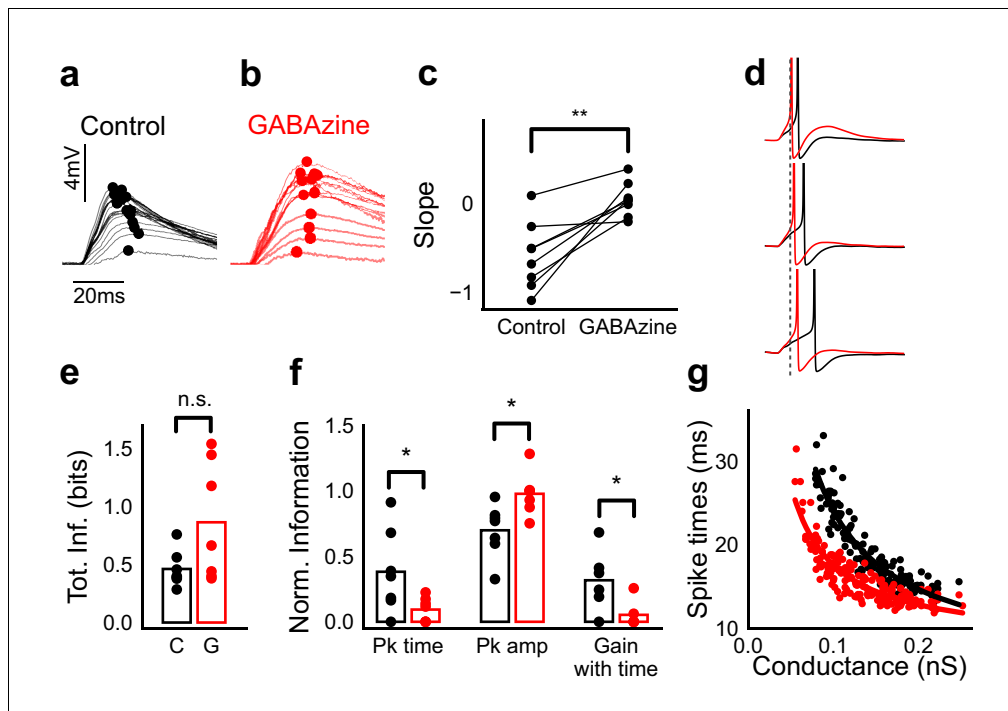


Figure 7. Advancing inhibitory onset changes PSP peak time and spike time with increase in stimulus strength. (a,b) The PSP peak arrived earlier following larger input in the control case (black), but not with GABAazine in bath (red). Traces for an example cell, binned (20 bins for Expected sum axis) and averaged, for control (black) and with GABAazine in bath (red). (c) Slope of the peak time was more negative in presence of inhibition (control) than when inhibition was blocked (GABAazine) ($n = 8$ cells). (d) Three example traces from the cell in g showing the relationship of spikes in presence (black) and absence of inhibition (red). Spikes were produced by HH model, using synaptic conductances from voltage clamp data. The separation between spike times of the two conditions increased with decrease in input conductance (top to bottom). (e) Total mutual information of peak amplitude and peak timing with expected sum was not significantly different between Control and GABAazine case (Wilcoxon Rank sum test (<0.05), $p=0.11$, $n = 7$ CA1 cells). (f) Normalized mutual information between Expected V_m and peak time, Expected V_m and peak amplitude, and conditional mutual information between Expected V_m and peak time, given the knowledge of peak amplitude. Normalized information was calculated by dividing mutual information by total information for each cell (as shown in d). Peak times carried more information in the presence of inhibition, and peak amplitudes carried more information in the absence of inhibition. There was higher gain in information about the input with timing if the inhibition was kept intact (Wilcoxon Rank sum test ($p<0.05$), $n = 7$ (Pk time, Pk amp) and ($p=0.05$) $n = 6$ (Gain with time) CA1 cells). (g) Relationship of spike time with excitatory conductance, in the presence (black) and absence of inhibition (red), for HH model simulations. All black points are medians of spikes of each excitation trace paired with six different repeats of inhibition for that combination.

DOI: <https://doi.org/10.7554/eLife.43415.016>

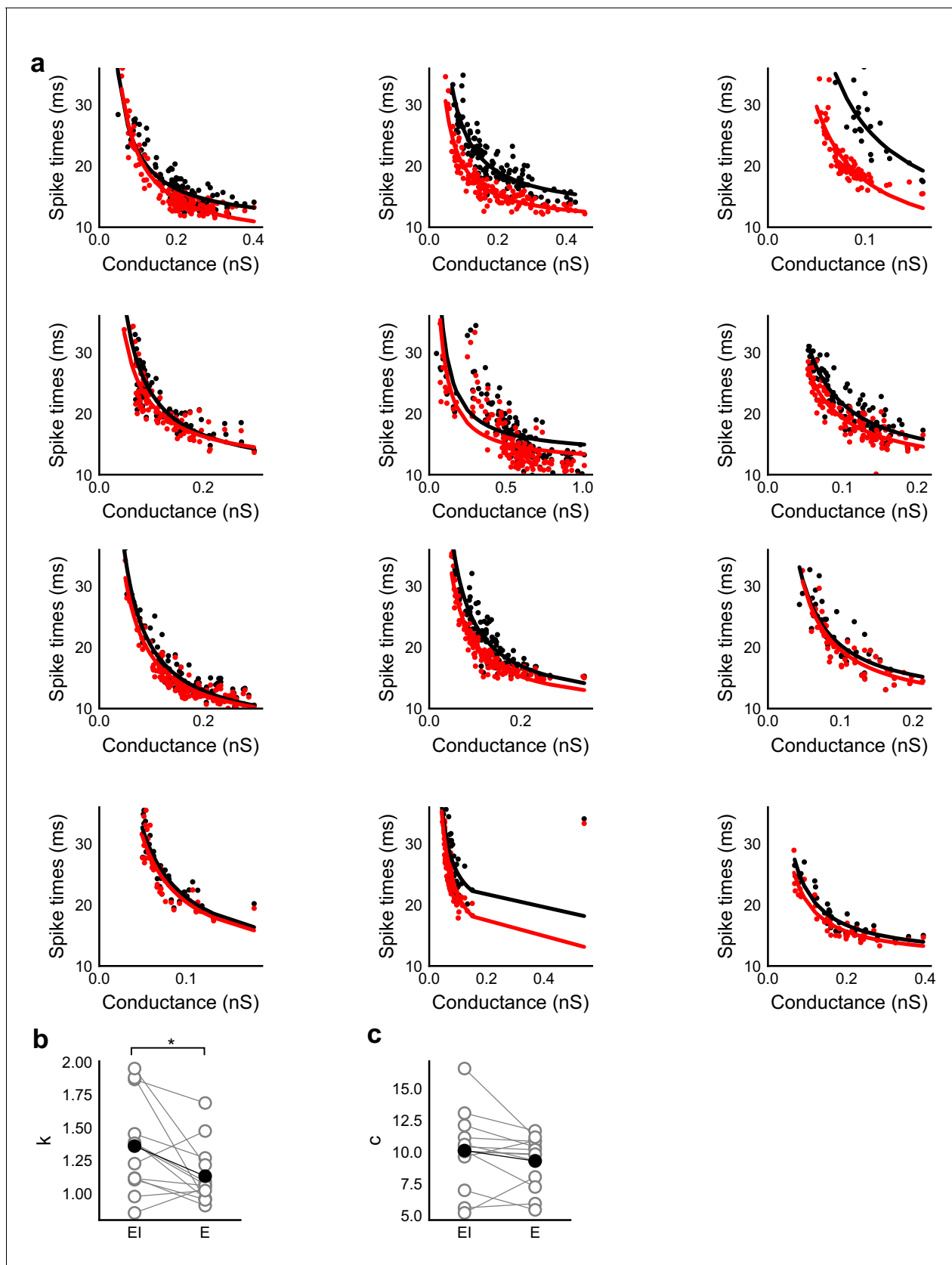


Figure 7—figure supplement 1. Spike time changes with increasing input are steeper in presence of inhibition. (a) Plots from HH model, simulated using data from voltage clamp cells, show the relationship of spike time with conductance, with (black) and without inhibition (red). Each plot is Figure 7—figure supplement 1 continued on next page

Figure 7—figure supplement 1 continued

produced using data from an individual cell. Each black point is the median of spike times evoked by excitation paired with six different repeats of inhibition for that stimulus combination. Red points are spike times produced for the same values of excitation, but without any inhibition. Separation of the curves was strongly dependent on the exact value of threshold. Using the natural threshold which emerged from the HH model (-56.3 mV), separation could be seen for about half the cells. (b,c) Value of fit parameters k, c when the relationship between spike times and excitatory were fit by $c + k/x$ curve. There was significant difference (Wilcoxon rank sum test, $p < 0.05$, $n = 13$) between the steepness of the curves for the cases with and without inhibition, where the absence of inhibition makes this curve steeper. There was no significant difference between the intercepts for these fits (Wilcoxon rank sum test, $p > 0.05$, $n = 13$).

DOI: <https://doi.org/10.7554/eLife.43415.017>

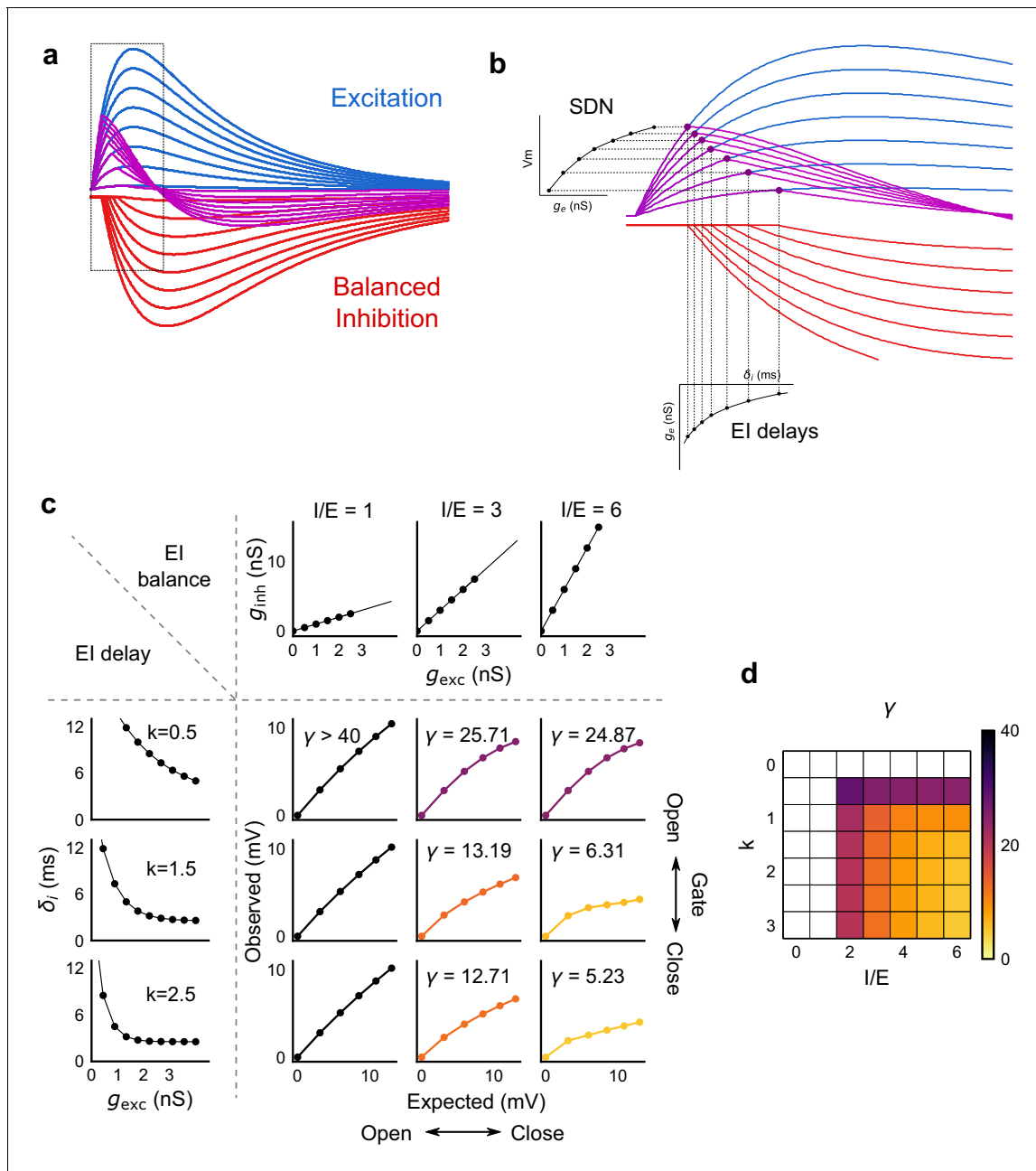


Figure 8. Emergence of SDN from balanced excitation and inhibition, coupled with dynamic EI delays. (a) Schematic showing precisely balanced EPSPs (blue) and corresponding IPSPs (red) summing to produce PSPs (purple). The EPSPs and IPSPs increase in equal input steps. (b) Zooming into the portion in the rectangle in a. Excitation onset is constant, but inhibition onset changes as an inverse function of input or conductance (g_{exc}), as shown in Figure 6. With increasing input, inhibition arrives earlier and cuts into excitation earlier for each input step. This results in smaller differences in excitatory peaks with each input step, resulting in SDN. The timing of PSP peaks (purple) becomes progressively advanced, whereas the timing of EPSP peaks (blue) does not, consistent with our results in Figure 7. (c,d) Normalization as a function of the two building blocks – El balance (I/E ratio) and El delays (interneuron recruitment kinetics, k , as predicted by the model. Larger values of both imply greater normalization and increased gating. Colors of the SDN curves depict the value of gamma (γ), as shown in the phase plot in d. White squares are values of γ larger than 40, where almost no normalization occurs.

DOI: <https://doi.org/10.7554/eLife.43415.018>

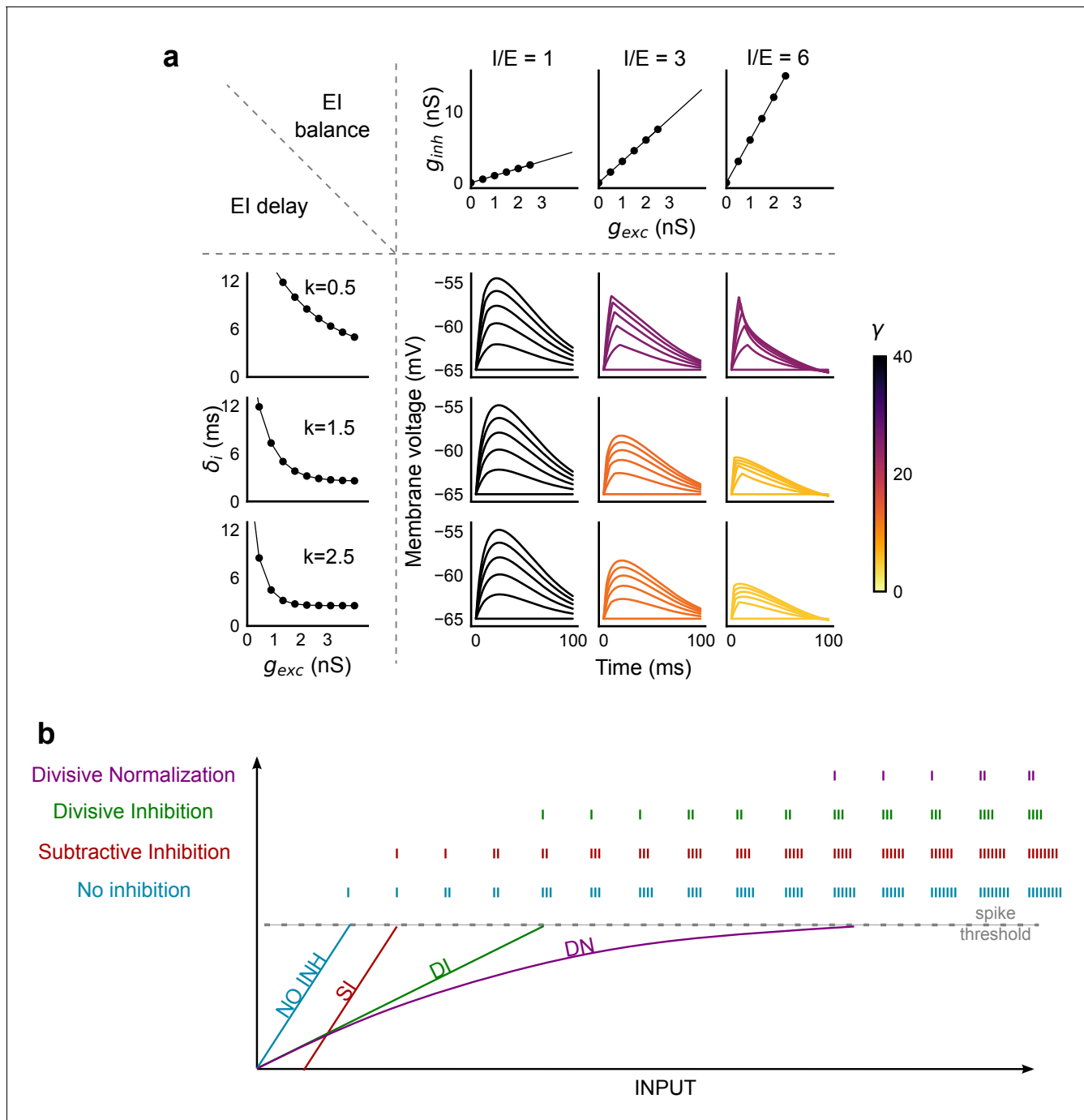


Figure 8—figure supplement 1. PSP traces showing the effect of I/E ratio and inhibitory recruitment kinetics (k) on SDN. (a) Similar to **Figure 8c**, but with the simulated membrane potential traces replacing the Input-Output curves. Colorbar represents values of γ . (b) Input range expansion by SDN. Schematic shows comparison of various models of EI interaction for the range of inputs accommodated by a neuron, before reaching spike threshold.

DOI: <https://doi.org/10.7554/eLife.43415.019>

Supplementary tables

Name (Units)	Median	25%	75%
Excitatory τ_{rise} (ms)	0.007	0.005	0.011
Excitatory τ_{decay} (ms)	0.016	0.011	0.020
Inhibitory τ_{rise} (ms)	0.013	0.005	0.020
Inhibitory τ_{decay} (ms)	0.027	0.020	0.038

S2a. Values taken from literature

Variable	Meaning	Source	Value
g_{leak}	Leak conductance	Fernandos and White, J. Neuro. (2010)	10 nS
E_{exc}	Excitatory reversal	Calculated (Methods)	0 mV
E_{inh}	Inhibitory reversal	Calculated (Methods)	-70 mV
E_{leak}	Leak reversal	Fernandos and White, J. Neuro. (2010)	-65 mV
C_m	Membrane capacitance	neuroelectro.org	100 pF

S2b. Values extracted by fitting data

Variable	Meaning	Range (units)
t	Time	0-100 ms
g_{exc}	Excitatory max conductance	0 - 5 nS
$\tau_{\text{exc}}^{\text{rise}}$	Excitatory Rise	7 ms
$\tau_{\text{exc}}^{\text{decay}}$	Excitatory Fall	16 ms
$\delta_{\text{exc}}^{\text{onset}}$	Excitatory onset time	0 ms
P	I/E ratio	0 - 5
g_{inh}	Inhibitory max conductance	$P \times g_{\text{exc}}$
$\tau_{\text{inh}}^{\text{rise}}$	Inhibitory Rise	13 ms
$\tau_{\text{inh}}^{\text{decay}}$	Inhibitory Fall	27 ms
$\delta_{\text{inh}}^{\text{onset}}$	Inhibitory onset time	2-15 ms

Variable	Meaning	Value
l	Soma length (cylindrical compartment)	10 μ
d	Soma diameter	10 μ
τ_m	Membrane time constant	0.01 s
E_{exc}	Excitatory reversal	0 mV
E_{inh}	Inhibitory reversal	-70 mV
E_{leak}	Leak reversal	-65 mV
E_{Ns}	Sodium channel reversal potential	55 mV
E_{KDR}	Delayed rectifier potassium channel reversal potential	-75 mV
g_{Ns}	Sodium channel maximum conductance	20 mS/cm ²
g_{KDR}	Delayed rectifier potassium channel maximum conductance	25 mS/cm ²

Chapter 4

Conclusion

In the preceding chapters, we showed two fundamental computational functions performed by specific network motifs. Stereotypical circuit motifs that perform specific computations are found across several biological networks (Milo, 2002), such as gene regulation, protein-protein interaction and neuronal networks. First, we investigated feedback motifs in the context of the robustness of bistable chemical reaction systems, known to be important for memory storage and decision making operations. Bistable chemical reaction systems have been observed across several biological systems: from decision making in mitosis to proposed chemical reaction systems responsible for memory storage at the synapses. Second, we looked at the feedforward inhibitory neuronal network in the hippocampus in the context of precise excitatory-inhibitory balance and input gain control. This circuit has been observed to be important for spatial, temporal and episodic memory formation.

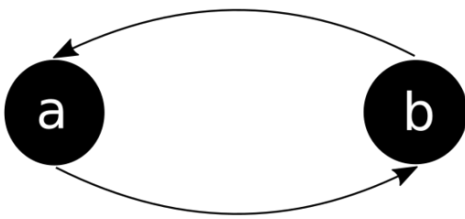
Network structures that are robust to various perturbations have been suggested as organizational units for larger biological networks (Prill et al., 2005; Angulo et al., 2015), (Chapter 1,2). We wanted to investigate the properties of network structures responsible for robustness to different kinds of perturbations, and if there are correlations between robustness to different perturbations across different chemical reaction networks (CRNs). We investigated the robustness of all bistable chemical reaction networks below the size of 3 reactants and 6 reactions, or 4 reactants and 3 re-

actions to perturbations to the network structure, reaction rates and intrinsic noise. We found no average relation between robustness to different perturbations. However, when we grouped the CRNs according to their smallest bistable subnetwork(s), or *root groups*, we found that the presence of a certain subset of these minimum bistable networks indicated a higher propensity of both network growth and tolerance to parametric fluctuations. Specifically, we found that we could add many reactions to group VI root CRN (Figure 4.1a, right) and it still retained bistability, and if a given CRN contained root group VI, it was more likely to have high parameter robustness. Further, combinations of different root groups suggested a principled way in which reaction systems could organize their robustness to different kinds of perturbations.

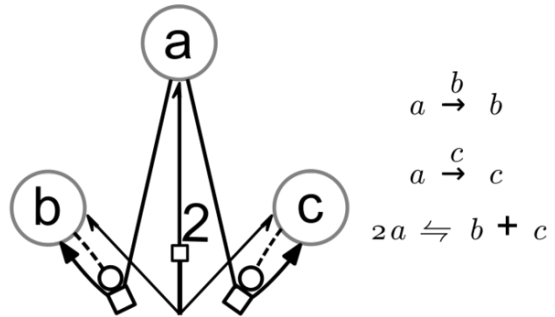
Feedforward inhibition is a commonly found circuit motif in the brain. In the second study, we investigated the hippocampal CA3-CA1 feedforward inhibitory circuit. This circuit is known to be important for spatial navigation and episodic memory formation. Neuronal circuits have certain characteristic attributes, for example, Excitation-Inhibition (EI) balance, which is thought to keep the total activity of the circuit in control. However, different theoretical proposals and experimental observations differed in their agreement on the precision of EI balance in the brain. There were different schools of thought that believed that excitation and inhibition were balanced only on average (global EI balance) and over slow (>10 ms) timescales (loose EI balance), or all presynaptic inputs (detailed EI balance) and over fast (<10 ms) timescales (tight EI balance) (Chapter 1). The combination of detailed and tight, called precise EI balance implies that random groups of presynaptic inputs are proportional for excitation and inhibition at fast timescales. The theoretical ramifications of this are discussed in (Barron et al., 2017). For our second goal, using a combination of theory, optogenetics and patch-clamp experiments, we designed a study to test the existence of *precise* EI balance in the brain. At this resolution of precise EI balance, arbitrary combinations of excitatory and inhibitory presynaptic network inputs are received at the postsynaptic neuron with close to identical ratios and at fast (<10 ms) timescales. We stimulated the hippocampal input network (CA3) with randomized, combinatorially chosen patterns of light and recorded from its

output (CA1) using patch-clamp. We found that the ratio between excitatory and inhibitory synaptic input in the hippocampal CA1 neurons was within a tightly bounded ratio, and there indeed was *precise* EI balance. Moreover, we discovered that the delay between excitation and inhibition was not constant, as previously thought. It reduced as we increased the number of excitatory inputs from CA3. This led us to discover a novel sub-threshold computation, where the response of the output (CA1) neurons increases linearly for small input, but as input is increased, the degree of change in the output keeps shrinking (Chapter 3, (Bhatia, Moza, and Bhalla, 2019)). This general phenomenon, called divisive normalization, has been widely observed at the suprathreshold level and has been shown to lead to gain control in the visual and olfactory systems (Carandini and Heeger, 1995, 2011; Olsen et al., 2010). We proposed (Bhatia, Moza, and Bhalla, 2019) that this mechanism may play an important role in the formation of place cells in the hippocampus. In this chapter, we conclude this thesis by presenting future directions and several questions that our studies have opened.

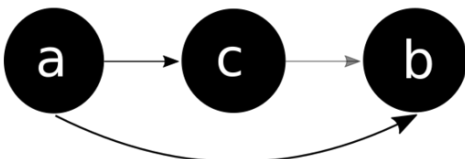
a. Feedback loop



Root group VI: |DabX|DacX|Fabc|



b. Feedforward loop



Hippocampal CA3-CA1 network

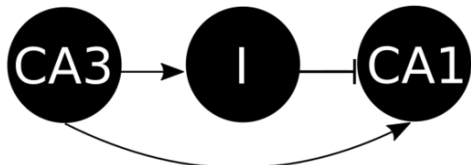


Figure 4.1: Feedforward and feedback loop motifs. **a.** (Left) Feedback loop motif showing recurrent activation (or inhibition). (Right) Group VI root CRN showing mirror-symmetric positive feedback loops with chemical reactions corresponding to the CRN. **b.** (Left) Feedforward loop motif showing a positive connection from a to c and a to b, and ambivalent (positive or negative) connection from c to b. (Right) Schematic of hippocampal CA3-CA1 circuit showing a feedforward inhibitory network with excitatory input from CA3 to I and CA3 to CA1 and inhibitory input from I to CA1.

Families of feedback loop networks inherit robustness attributes from their root networks

Biological systems consist of colossal networks of interacting molecules, computing and transforming information over time. Theoretical models that study these complex systems select a level of description and all interactions that are above or below a certain degree of resolution to the chosen scale (Goldenfeld, 1999) are either coarse-grained or ignored. For example, while modelling neuronal networks, the details of the chemistry of dendritic spines are ignored, and conversely, while modelling the chemistry of dendritic spines, neuronal activity in multiple neurons in the net-

work is ignored. This is only possible because of the natural separation of length, time and energy scales in these systems.

However, the coarse-grained network structures that represent specific computations at a given level of description may be relevant to multiple levels of description: for the example above, both in the network of chemicals in the synapse and the structure of connectivity of neurons. These recurrent graphical structures called *motifs* have been found in several networks in a variety of biological systems across several scales (Chapter 1). Why are some network structures more frequent than others? One suggestion has been that evolution favours robust network motifs. Thus, while the same computational function can be performed by several architectures, some network structures are more resilient to addition or subtraction of connections, or changes in parameters which govern the dynamics on these networks.

We asked the question: are structural perturbations and parametric perturbations to a network correlated? On average, we saw that there was a weak correlation between them. We then grouped the CRNs by the presence of the smallest networks that showed bistability (*root groups*) in these subnetworks. From this new perspective, we found CRNs which had certain root groups showed a higher trend for both structural and parametric robustness. Specifically, the beautiful mirror-symmetric motif of group VI (Fig. 4.1a), which consists of two competitive autocatalytic feedback loops was highly resistant to parameter fluctuations, and it could retain its ability to be bistable with the addition of reactions to form larger networks.

We found surprising and interesting links between our findings and the origin of life literature that suggests the abiogenic origin of enantiomeric purity found in biological systems. We found that two highly cited autocatalytic mechanisms (Frank, 1953; Viedma, 2005) proposed for causing this asymmetry had the highest parametric robustness in all CRNs that we tested. One of these was again the group VI root CRN, which is robustly bistable to both parametric fluctuations, and to the addition of new reactions in the network. The other was structurally similar to group VI, in that it

also had competitive autocatalytic feedback loops with a shared substrate. Our study reveals two attributes of this autocatalytic network structure which are interesting from the perspective of a hypothetical early biological network. First, mirror-symmetric competitive autocatalytic loops are the best strategy for parametric robustness in small reaction networks. Second, the addition of new links to this CRN tends to retain bistable dynamics. As mutations alter the structure of the biological CRNs or allow exploration of their parameter space, the two attributes mentioned above allow the network to grow in complexity while retaining bistable dynamics. Similar architectures have also been used experimentally to synthesize pure chiral products from achiral substrates (Shibata et al., 1996). Parametrically robust bistable reaction systems proposed by us could similarly be considered to synthesise such homochiral products. Similarly, such networks could also be used for making biochemical sensors using synthetic biology constructs. Robust bistability is desirable in networks in these cases to avoid fine-tuning of chemical reaction rates, promoter region affinity, etc.

Future directions

An immediate question that emerges from this is: are these networks truly over-represented in biological systems? To investigate this, first, the bimolecular reactions in the (dat) have to be converted to interaction graphs, because most biochemical reaction databases are in this form. Then using an appropriate motif search algorithm, these subnetworks can be queried against the biochemical reaction databases. However, there is the caveat that reducing these bimolecular reaction systems to interaction graphs is lossy and generally has many possible solutions.

What structural properties do these 24 groups have in common? Are there general properties that are common to all of these bistable mechanisms? We did not explore the structure of these root groups further, to look for further similarities between their structure. This line of inquiry may suggest general rules to design minimal structures for systems of other sizes.

Our metric for Noise robustness relies on explicit stochastic simulation of chemical reaction systems, and we were not able to simulate many systems to measure their residence times accurately across several sets of reaction rates. This was due to two reasons: first, a lot of bistable systems had *stuck-states*, i.e., stable states from which no escape is possible with noise. This happened because irreversible reactions are allowed in our framework, which can lead to steady-states with zero concentrations of reactants without any flux that can produce the reactant. In order to avoid such stuck-states, each reaction will need to be (at least weakly) reversible. Second, for some CRNs, the network had high robustness to noise, which led to large simulation times. It would be useful to implement tau-leaping (Gillespie, 2001) to accelerate these simulations to measure both residence and relaxation times accurately.

Feedforward inh circuit with precise EI balance leads to gain control

Neural syntax or the language neurons use to communicate with each other remains one of the biggest unsolved problems in neuroscience. It is possible that unlike the genetic code, no universal code exists for the brain. However, several remarkably general attributes of the neural code have been discovered, for example, synaptic plasticity, stochastic synaptic release, network oscillations, and excitation-inhibition (EI) balance. Given the observed ubiquity of these principles, at least across mammalian brains, a general theory of neuronal computation is likely to include these variables with appropriate plasticity rules that provide structured ways for learning parameter values for these variables. Our study has been able to directly compare contending theoretical ideas regarding the precision of excitatory-inhibitory balance in the brain. This led to our discovery that EI balance is combinatorially precise in the hippocampal CA3-CA1 network, and perhaps generally in feedforward networks (Fig 4.1b). This implies that for a given output neuron, the basal ratio between excitatory and inhibitory presynaptic inputs is maintained within a tight bound for all combinations of inputs it receives.

Recent advances in optogenetics and imaging techniques have hugely facilitated perturbation and measurement of neurons selectively and in large numbers. Thus, it has become increasingly possible to design experiments to attack fundamental problems in a theoretically guided manner. Consequently, the gap between theoretical and experimental neuroscience has gradually started narrowing down. For example, in the field of EI balance, it took many years for (Wehr and Zador, 2003) to experimentally test and provide evidence against theoretical ideas of an average, slow time-scale excitation-inhibition balance (Gerstein and Mandelbrot, 1964; v. Vreeswijk and Sompolinsky, 1996; Shadlen and Newsome, 1994). However recent predictions from Tim Vogels' and others (Vogels et al., 2011) were immediately tested by Rob Froemke (D'amour and Froemke, 2015), suggesting an excitation-dependent inhibitory plasticity rule for the existence of a detailed balance between excitation and inhibition. Our study was similarly designed using a theoretical grounding at three levels. First, at the level of the design of the central question. Our experimental design directly distinguished between the theoretically proposed precise, detailed, tight, global, and loose balance categories. Second, at the level of computational analysis. We used a mixture of relevant analysis methods on our data, having several parallel measurables to optimize the extraction of information. We also kept our analysis in a tight feedback loop with the experiments. As a result, we were able to tweak the experimental design in an informed way for optimizing data collection, and also direct the experiments after key observations had been made. Lastly, we designed theoretical models which used experimentally acquired data to mechanistically explain the observation of subthreshold divisive normalization.

On a related note, a large focus of experimental neuroscience in the context of neural code has been on suprathreshold computation. Perhaps this is because firing rates are easily measured. However, there are several theoretical problems with this notion as mentioned in Chapter 1, most importantly that of accurate measurement of the high variance Poisson firing rate within the neuronal integration time. Our study has been able to provide a concrete observation of a subthreshold computation, and its connections with precise EI balance in the brain. For the hippocampal CA1,

where spiking is known to be sparse, Subthreshold Divisive Normalization (SDN) could play an important role as a subthreshold gain control mechanism determining CA1 spike times in response to bursty input from CA3. Another role we've proposed for SDN *in-vivo* is inhibitory gating. Using inhibitory gating, the normally gated *off* inputs for a subgroup of neurons can be gated *on* by "gate-modulating mechanisms" to allow for stimuli to selectively activate this subgroup. Example of such mechanisms could be disinhibition by interneurons that inhibit other interneurons such as VIP interneurons, or by short-term synaptic facilitation or depression. One signature of such inhibitory gating mechanisms would be that the postsynaptic neuron subgroups would receive a lot more "gated *off*" excitatory inputs than are necessary to drive them. These inputs can then be selectively gated *on*, when necessary. This makes SDN a potential mechanism for the conversion of silent cells to place cells in the hippocampus. Silent cells in the hippocampus have been converted to place cells for arbitrary locations by artificial current injections (Lee et al., 2012; Bittner et al., 2015). One way to interpret this is that information about many locations continuously reaches hippocampal CA1 cells, however, some cells are selectively activated for specific locations (gated *on*), which become place cells. We have suggested (Bhatia, Moza, and Bhalla, 2019) that the SDN along with inhibitory gating mechanisms could act on hippocampal place/time cells *in-vivo*, selecting specific cells to be activated.

Future directions

Several interesting questions have emerged from our work. We were only able to establish the existence of precise EI balance at the hippocampal CA1 neurons by somatic measurement. However, inhibitory inputs are distributed all over the neuron's dendrites. It is tempting to wonder if there are sub-neuronal compartments such as dendrites, or even doubly-innervated dendritic spines (Chen et al., 2012), where precise EI balance exists. Next, several different categories of interneurons are known to exist both in the hippocampus and in the cortex. These interneuron populations are developmentally segregated and are known to have different morphologies, molecular

markers and intrinsic and network properties. For example, a set of interneurons called basket cells are parvalbumin-positive (PV), and are known to have low thresholds, high firing rates, and innervate CA1 pyramidal neurons close to the soma and axon initiation segment. This leads to many important questions: Are there different timescales of EI balance, based on the interneuron type? Do they lead to similar I/E ratios distributions, or are the somatically measured I/E ratios at the pyramidal neurons a sum of many interneuron-type dependent I/E ratios? Are the interneurons also EI balanced themselves? These also point to the broader question, what is the functional role of the diversity of I/E ratios for neural coding?

There are also several important yet unanswered questions about the emergence of precise EI balance at the hippocampus. First, mechanistically, how does this balance emerge and how is it maintained at the hippocampus? Given that there is synaptic plasticity in hippocampal neurons, and the circuit has 10-20% interneurons, it is non-trivial to construct a network which can passively maintain a balanced state. Thus, are the neurons continuously getting rebalanced by an excitation-dependent inhibitory plasticity rule, similar to the cortex (D'amour and Froemke, 2015)?

Our study was designed to deconstruct the synaptic inputs at CA1 to isolate and finely control the CA3 excitation and feedforward inhibition. However, *in-vivo*, CA1 neurons receive continuous, mixed, dynamically changing inputs. How do these currents change as a behaving animal navigates a maze, or does a trace-conditioning task? In the same vein, oscillations are known to be maintained and their phases tuned by interneuron populations. In the hippocampal CA3, EI balance is maintained during gamma oscillations (Atallah and Scanziani, 2009). What happens to EI balance during different kinds of oscillations during wakefulness and under different stages of sleep? Given their simultaneous and hierarchical organization of network oscillations across mammalian brains (Buzsáki et al., 2013), are there different delay relationships and EI ratios for different sets of interneurons to maintain these rhythms? Further, what kinds of plasticity rules can maintain I/E ratios in recurrent networks that generate oscillatory inputs?

Answers to these fundamental questions would lay the grounds for a more complete picture of the role of EI balance in the neural syntax and the organization of neuronal activity in the brain.

Bibliography

- SWITCHES database. Searchable Web Interface for Topologies of CHEmical Switches. URL <https://switches.ncbs.res.in>. Based on parent publication Ramakrishnan and Bhalla, Plos Comp. Bio. (2008).
- Marco Tulio Angulo, Yang-Yu Liu, and Jean-Jacques Slotine. Network motifs emerge from interconnections that favour stability. *Nature Physics*, 11(10):848–852, jul 2015. doi: 10.1038/nphys3402. URL <https://doi.org/10.1038/nphys3402>.
- Bassam V. Atallah and Massimo Scanziani. Instantaneous Modulation of Gamma Oscillation Frequency by Balancing Excitation with Inhibition. *Neuron*, 62(4):566–577, may 2009. doi: 10.1016/j.neuron.2009.04.027. URL <https://doi.org/10.1016/j.neuron.2009.04.027>.
- Helen C. Barron, Tim P. Vogels, Timothy E. Behrens, and Mani Ramaswami. Inhibitory engrams in perception and memory. *Proceedings of the National Academy of Sciences*, page 201701812, jun 2017. doi: 10.1073/pnas.1701812114. URL <https://doi.org/10.1073/pnas.1701812114>.
- Aanchal Bhatia, Sahil Moza, and Upinder Singh Bhalla. Precise excitation-inhibition balance controls gain and timing in the hippocampus. *eLife*, 8, apr 2019. doi: 10.7554/elife.43415. URL <https://doi.org/10.7554/elife.43415>.
- Katie C Bittner, Christine Grienberger, Sachin P Vaidya, Aaron D Milstein, John J Macklin, Junghyup Suh, Susumu Tonegawa, and Jeffrey C Magee. Conjunctive input processing drives

- feature selectivity in hippocampal CA1 neurons. *Nature Neuroscience*, 18(8):1133–1142, jul 2015. doi: 10.1038/nn.4062. URL <https://doi.org/10.1038%2Fnn.4062>.
- György Buzsáki, Nikos Logothetis, and Wolf Singer. Scaling Brain Size Keeping Timing: Evolutionary Preservation of Brain Rhythms. *Neuron*, 80(3):751–764, oct 2013. doi: 10.1016/j.neuron.2013.10.002. URL <https://doi.org/10.1016%2Fj.neuron.2013.10.002>.
- Matteo Carandini and David J. Heeger. Summation and Division in V1 Simple Cells. In *The Neurobiology of Computation*, pages 59–65. Springer US, 1995. doi: 10.1007/978-1-4615-2235-5_10. URL https://doi.org/10.1007%2F978-1-4615-2235-5_10.
- Matteo Carandini and David J. Heeger. Normalization as a canonical neural computation. *Nature Reviews Neuroscience*, 13(1):51–62, nov 2011. doi: 10.1038/nrn3136. URL <https://doi.org/10.1038%2Fnrn3136>.
- Jerry L. Chen, Katherine L. Villa, Jae Won Cha, Peter T.C. So, Yoshiyuki Kubota, and Elly Nedivi. Clustered Dynamics of Inhibitory Synapses and Dendritic Spines in the Adult Neocortex. *Neuron*, 74(2):361–373, apr 2012. doi: 10.1016/j.neuron.2012.02.030. URL <https://doi.org/10.1016%2Fj.neuron.2012.02.030>.
- James A. D’amour and Robert C. Froemke. Inhibitory and Excitatory Spike-Timing-Dependent Plasticity in the Auditory Cortex. *Neuron*, 86(2):514–528, apr 2015. doi: 10.1016/j.neuron.2015.03.014. URL <https://doi.org/10.1016%2Fj.neuron.2015.03.014>.
- F.C. Frank. On spontaneous asymmetric synthesis. *Biochimica et Biophysica Acta*, 11:459–463, jan 1953. doi: 10.1016/0006-3002(53)90082-1. URL <https://doi.org/10.1016%2F0006-3002%2853%2990082-1>.
- George L. Gerstein and Benoit Mandelbrot. Random Walk Models for the Spike Activity of a Single Neuron. *Biophysical Journal*, 1(2):139–151, feb 1958. doi: 10.1016/S0006-3002(58)86901-5. URL [https://doi.org/10.1016/S0006-3002\(58\)86901-5](https://doi.org/10.1016/S0006-3002(58)86901-5).

- gle Neuron. *Biophysical Journal*, 4(1):41–68, jan 1964. doi: 10.1016/s0006-3495(64)86768-0.
URL [https://doi.org/10.1016/s0006-3495\(64\)86768-0](https://doi.org/10.1016/s0006-3495(64)86768-0).
- Daniel T. Gillespie. Approximate accelerated stochastic simulation of chemically reacting systems. *The Journal of Chemical Physics*, 115(4):1716–1733, jul 2001. doi: 10.1063/1.1378322. URL <https://doi.org/10.1063/1.1378322>.
- N. Goldenfeld. Simple Lessons from Complexity. *Science*, 284(5411):87–89, apr 1999. doi: 10.1126/science.284.5411.87. URL <https://doi.org/10.1126/science.284.5411.87>.
- D. Lee, B.-J. Lin, and A. K. Lee. Hippocampal Place Fields Emerge upon Single-Cell Manipulation of Excitability During Behavior. *Science*, 337(6096):849–853, aug 2012. doi: 10.1126/science.1221489. URL <https://doi.org/10.1126/science.1221489>.
- R. Milo. Network Motifs: Simple Building Blocks of Complex Networks. *Science*, 298(5594):824–827, oct 2002. doi: 10.1126/science.298.5594.824. URL <https://doi.org/10.1126/science.298.5594.824>.
- SR Olsen, V Bhandawat, and RI Wilson. Divisive normalization in olfactory population codes. *Neuron*, 66:287–99, Apr 2010.
- RJ Prill, PA Iglesias, and A Levchenko. Dynamic properties of network motifs contribute to biological network organization. *PLoS Biol*, 3:e343, Nov 2005.
- Michael N. Shadlen and William T. Newsome. Noise neural codes and cortical organization. *Current Opinion in Neurobiology*, 4(4):569–579, aug 1994. doi: 10.1016/0959-4388(94)90059-0.
URL [https://doi.org/10.1016/0959-4388\(94\)90059-0](https://doi.org/10.1016/0959-4388(94)90059-0).
- Takanori Shibata, Hiroshi Morioka, Tadakatsu Hayase, Kaori Choji, and Kenso Soai. Highly Enantioselective Catalytic Asymmetric Automultiplication of Chiral Pyrimidyl Alcohol. *Journal of*

- the American Chemical Society*, 118(2):471–472, jan 1996. doi: 10.1021/ja953066g. URL <https://doi.org/10.1021/ja953066g>.
- C. v. Vreeswijk and H. Sompolinsky. Chaos in Neuronal Networks with Balanced Excitatory and Inhibitory Activity. *Science*, 274(5293):1724–1726, dec 1996. doi: 10.1126/science.274.5293.1724. URL <https://doi.org/10.1126/science.274.5293.1724>.
- Cristobal Viedma. Chiral Symmetry Breaking During Crystallization: Complete Chiral Purity Induced by Nonlinear Autocatalysis and Recycling. *Physical Review Letters*, 94(6), feb 2005. doi: 10.1103/physrevlett.94.065504. URL <https://doi.org/10.1103/physrevlett.94.065504>.
- T. P. Vogels, H. Sprekeler, F. Zenke, C. Clopath, and W. Gerstner. Inhibitory Plasticity Balances Excitation and Inhibition in Sensory Pathways and Memory Networks. *Science*, 334(6062):1569–1573, nov 2011. doi: 10.1126/science.1211095. URL <https://doi.org/10.1126/science.1211095>.
- Michael Wehr and Anthony M. Zador. Balanced inhibition underlies tuning and sharpens spike timing in auditory cortex. *Nature*, 426(6965):442–446, nov 2003. doi: 10.1038/nature02116. URL <https://doi.org/10.1038/nature02116>.